MODELING THE IMPACT OF BIOMASS COMBUSTION ON ATMOSPHERIC AEROSOL

Thesis by

Brigitte Lee Rooney

In Partial Fulfillment of the Requirements for

the degree of

Doctor of Philosophy

Caltech

CALIFORNIA INSTITUTE OF TECHNOLOGY

Pasadena, California

2020

(Defended May 29, 2020)

© 2020

Brigitte Lee Rooney
ORCID: 0000-0002-9725-9080

ACKNOWLEDGEMENTS

ABSTRACT

Biomass burning is a significant source of atmospheric particulate matter less than 2.5 micrometers in diameter ($PM_{2.5}$) and encompasses a variety of activities, fuels, and emissions profiles. A significant portion of the world population relies on solid biofuels for cooking and other household activities. Residential use of solid biofuels can have negative impacts on human health, particularly in southeast Asia, and contribute to ambient air quality. In addition, wildfires are of increasing concern as climate changes and human activity expands further into the wildland-urban interface. Understanding the contributions of biomass combustion to air quality is critical for creating mitigation strategies.

In this work, the impact of biomass burning on air quality is examined using numerical and observational methods. The Community Multiscale Air Quality modeling system (CMAQ) and the Weather Research and Forecasting model coupled with Chemistry (WRF-Chem) are used to study two biomass burning scenarios: the combustion of solid biofuels for cooking in rural India and the November 2018 Camp Fire in northern California. Model simulations are combined with surface and satellite observational data to evaluate their performance as well as their applicability to health and economic impact assessment studies. Additionally, discrepancies in methods used in laboratory experiments and field studies of cookstove emissions are investigated. Contributions of cookstove and wildfire emissions to $PM_{2.5}$ are estimated, and climate and health co-benefits of residential solid biofuel use is assessed. This thesis strives to expand the current understanding of sources of $PM_{2.5}$ and provide a base for future computational studies of biomass burning impacts on air quality, climate, and human health.

PUBLISHED CONTENT AND CONTRIBUTIONS

Rooney, B., R. Zhao, Y. Wang, K. Bates, A. Pillarisetti, S. Sharma, S. Kundu, T.C. Bond, N.L. Lam, B. Ozaltun, L. Xu, V. Goel, L.T. Fleming, R. Weltman, S. Meinardi, D.R. Blake, S.A. Nizkorodov, R.D. Edwards, A. Yadav, N.K. Arora, K.R. Smith, J.H. Seinfeld, (2019). "Impacts of household sources on air pollution at village and regional scales in India". In: *Atmospheric Chemistry and Physics* 19, pp. 7719–7742. doi: 10.5194/acp-19-7719-2019.
B.R. prepared emissions inventory data for model input, carried out meteorological and chemical transport simulations, analyzed data, and participated in the writing of the manuscript.

Rooney, B., Y. Wang, J.H. Jiang, B. Zhao, K.R. Verhulst, Z. Zeng, J.H. Seinfeld, (2020). "Air Quality Impact of the Northern California Camp Fire of November 2018". *In preparation.*
B.R. performed meteorological and chemical transport simulations, analyzed data, and participated in the writing of the manuscript.

Weltman, R. M., R. D. Edwards, L.T. Fleming, A. Yadav, C.L. Weyant, B. Rooney, J.H. Seinfeld, N.K. Arora, T.C. Bond, S.A. Nizkorodov, K.R. Smith,, (2020). "Climate and health co benefits from household solid fuel use in Haryana, India". *Accepted: Environmental Science & Technology.*
B.R. participated in data analysis and writing the manuscript.

TABLE OF CONTENTS

C h a p t e r   1

INTRODUCTION

Aerosols are suspensions of liquid or solid particles in gas and describe a broad class of atmospheric pollutants. They vary greatly in size, mass, surface area, and composition. Aerosol is classified as either primary or secondary (Seinfeld and Pandis., 2013). Primary aerosol is directly emitted into the atmosphere from various sources, and secondary aerosols are formed in the atmosphere via gas phase nucleation or partitioning of gas phase compounds to other particles. Secondary organic aerosol results from the oxidation of volatile organic compounds (VOCs) in the atmosphere.

Numerous studies show that aerosol can negatively impact human health. Levels of $PM_{2.5}$ are strongly correlated to occurrence of cardiovascular, cardiopulmonary, and respiratory disease, as well as increased mortality and morbidity (Dockery et al., 1993). The specific pathway and effect of aerosols vary depending on characteristics of the particle. Size and surface area constrain the deposition and translocation of inhaled particles into the body. The relationship of chemical composition to specific health impacts remains largely unknown, however it is suspected to play an important role (Araujo et al., 2008). To protect public health, the United States Environmental Protection Agency regulates particulate matter by mass concentration of two size classes: particulate matter less than 10 micrometers in diameter (PM_{10}) and particulate matter less than 2.5 micrometers in diameter ($PM_{2.5}$).

Aerosols can also impact the climate. Aerosols directly affect the climate by absorbing or scattering incoming solar radiation. Absorbing particles, like black carbon (BC), contribute to the greenhouse gas effect and warm the atmosphere. Additionally, particles can serve as cloud condensation nuclei and participate in the formation and characterization of clouds, indirectly affecting the climate. Because of their complexity, aerosols remain one of the greatest uncertainties in climate models.

Aerosols have a variety of sources, both natural and anthropogenic. Natural sources include sea spray, wind-blown dust, volcanic eruptions, wildfires, and oxidation of biogenic VOCs.

Anthropogenic sources of primary and secondary aerosol include solvent use, fuel combustion for transportation, industry, and power generation, and biomass burning for agricultural and cooking purposes.

The composition of biomass burning aerosol and aerosol precursors varies widely depending on fuel composition and combustion conditions. Common biomass fuel for human use includes crop residue, wood, dung, and peat. Emissions consist largely of black carbon and organics. Recent studies have identified the presence of additional molecules, like polycyclic aromatic hydrocarbons (PAHs), polyphenols, and nitrogen-containing aromatics, that efficiently absorb solar radiation in a narrow spectral range, leading to the classification of biomass burning organic aerosol as brown carbon (BrC) (Laskin et al., 2015, Lin et al., 2016, and Fleming et al., 2018).

Nearly 3 billion people worldwide cook with solid fuels of biomass or charcoal (Edwards et al., 2017). Exposure to $PM_{2.5}$ from household air pollution cause an estimated 3.9 million premature deaths annually (Smith et al., 2014).

Wildfires are part of the natural maintenance of ecological health. However, fire emissions and atmospheric transport of smoke across great distances pose a threat to human health. An estimated 339,000 global deaths annually are due to wildfire smoke (Johnston et al., 2012). Exposure is strongly associated with exacerbations of respiratory conditions, however the links between smoke exposure and various mortalities is uncertain (Reid et al., 2016). As the climate changes, drought and extreme weather events are increasing the frequency of large wildfires. Greater frequency of wildfires and the growth of the wildland-urban interface is increasing the number of people at risk of wildfire smoke exposure (Cascio et al., 2017).

Air quality modeling (AQM) is a useful tool for hypothesis testing of scientific processes and policy and decision making. There are numerous air quality models of varying complexity designed for global, regional, and local scales. AQMs are primarily 3D box models of chemical transport with on the order of 10^5 to 10^6 boxes that produce temporally- and spatially- varying concentrations of many atmospheric chemical species. Atmospheric models generally incorporate meteorology, emissions, chemistry, and thermodynamics, with

additional aerosol-specific mechanisms. They employ data obtained from laboratory experiments, field studies, satellite retrievals, surface monitoring, and reanalysis modeling. AQMs represent the state of the science and can assist in identifying emission sources, testing mitigation strategies, and forecasting pollution events. Additionally, AQMs can inform exposure and risk modeling for health and economic studies.

This thesis focuses on the atmospheric simulation of biomass combustion emissions. Chapter 1 addresses the air quality impacts of biomass burning emissions from cookstoves in a relatively understudied and data-sparse region of India. Chapter 2 addresses further the development and preparation of data from cookstove emissions. Chapter 3 investigates simulation of the regional impact of one of the largest wildfires in California history, the Camp Fire.

References

Araujo, J.A. et al. (2008). "Ambient Particulate Poolutants in the Ultrafine Range Promote Early Atherosclerosis and System Oxidative Stress". In: *Circ. Res.* 102, 589-596.
doi: 10.1161/CIRCRESAHA.107.164970.

Cascio, W. E.: Wildland fire smoke and human health, Science of the Total Environment, 624, 586-595, https://.doi.org/10.1016/j.scitotenv.2017.12.086, 2018.

Reid, C.E. et al. (2016). "Critical review of health impacts of wildfire smoke exposure". *In: Env. Health Perspectives,* 124. Doi: 10.1289/ehp.1409277

Edwards, R. et al. (2017). "Modeling emission rates and exposures from outdoor cooking". *In: Atmospheric Environment*, 164, 50-60. Doi: 10.1016/j.atmosenv.2017.05.029

Dockery, D. W. et al. (1993). "An Association between Air Pollution and Mortality in Six U.S. Cities". In: *N Engl J Med* 329, pp. 1753–1759.

Fleming, L.T. et al. (2018). "Molecular composition of particular matter emissions from dung and brushwood burning household cookstoves in Haryana, India". *In: Atmos. Chem. And Phys.*, 18, 2461-2480. Doi: 10.5194/acp-18-2461-2018.

Johnston, F.H. et al. (2012). "Estimated global mortality attributable to smoke from landscape fires". *In: Env. Health Perspectives,* 120. Doi: 10.1289/ehp.1104422.

Laskin A., et al. (2015). "Chemistry of Atmospheric Brown Carbon". In: *Chem. Rev.*, 115, 4335-4382. Doi: 10.1021/cr5006167.

Lin, P. et al. (2016). "Molecular Characterization of Brown Carbon in Biomass Burning Aerosol Particles. *In: Environ. Sci. Technol.,* 50, 11815-11824. Doi: 10.1021/acs.est.6b03024

Seinfeld, J. H . and S. N. Pandis (2013). *Atmospheric Chemistry and Physics*. Hoboken, New Jersey: John Wiley & Sons, Inc.

Smith, K. R., et al. (2014). "Millions Dead: How do we know and what does it mean? Methods used in the Comparative Risk Assessment of Household Air Pollution". In: *Annu. Rev. Public Health* 35, pp. 185-206. doi: 10.1146/annurev-publhealth-032013-182356.

Chapter 2

IMPACTS OF HOUSEHOLD SOURCES ON AIR POLLUTION
AT VILLAGE AND REGIONAL SCALES IN INDIA

2.1 Introduction

Although outdoor air pollution is widely recognized as a health risk, quantitative understanding remains uncertain on the degree to which household combustion contributes to unhealthy air. Recent studies in China, for example, show that 50-70% of black carbon emissions and 60-90% of organic carbon (OC) emissions can be attributed to residential coal and biomass burning (Cao et al., 2006; Klimont et al., 2009; Lai et al., 2011). Moreover, existing global emissions inventories show a significant contribution of household sources to primary $PM_{2.5}$ (particulate matter of diameter less than or equal to 2.5 micrometers) emissions. The Indo-Gangetic Plain of Northern India (23-31° N, 68-90° E) has among the world's highest values of $PM_{2.5}$. In this region, the major sources of emissions of primary $PM_{2.5}$ and of precursors to secondary $PM_{2.5}$ are coal-fired power plants, industries, agricultural biomass burning, transportation, and combustion of biomass fuels for heating and cooking (Reddy and Venkataraman, 2002; Rehman et al., 2011). The southwest monsoon in summer months in India leads to lower pollution levels than in winter months, which are characterized by low wind speeds, shallow boundary layer depths, and high relative humidity (Sen et al., 2017). With the difficulty in determining representative emissions estimates (Jena et al., 2015; Zhong et al., 2016), simulating the extremely high $PM_{2.5}$ observations in the Indo-Gangetic Plain has remained a challenge (Schnell et al., 2018).

Approximately 3 billion people worldwide cook with solid fuels, such as wood, charcoal, and agricultural residues (Bonjour et al., 2013; Chafe et al., 2014; Smith et al., 2014; Edwards et al., 2017). Used also for residential heating, such solid fuels are often combusted in inefficient devices, producing black carbon (BC) and organic carbon emissions. Between 2.6 and 3.8 million premature deaths occur as a result to exposure to fine particulate matter from household air pollution (Health Effects Institute, 2018a; World Health Organization, 2018). In India, more than 50% of households report use of wood or crop residues, and 8% report use of dung as cooking fuel (Klimont et al., 2009; Census of India, 2011; Pant and Harrison, 2012). Residential biomass burning is one of the largest individual contributors to the burden of disease in India, estimated to be responsible for 780,000 premature deaths in 2016 (Indian Council of Medical Research et al., 2017). The recent GBD MAPS Working Group (Health Effects Institute, 2018b) estimated that household emissions in India produce about 24% of ambient air pollution exposure. Coal combustion, roughly evenly divided between industrial sources and thermal power plants, was estimated by this study to be responsible for 15.3% of exposure in 2015. Open burning of agricultural crop stubble was estimated annually to be responsible for 6.1% nationally, although more important in some areas.

Traditional biomass cookstoves, with characteristic low combustion efficiencies, produce significant gas- and particle-phase emissions. An early study of household air pollution in India found outdoor total suspended particulate matter (TSP) levels in four Gujarati villages well over 2 mg m^{-3} during cooking periods (Smith et al., 1983). Secondary organic aerosol (SOA), produced by gas-phase conversion of volatile organic compounds to the particulate phase, is also important in ambient PM levels, yet there is a dearth of model predictions to which data can be compared. Overall, household cooking in India has been estimated by various groups to produce 22-50% of ambient PM$_{2.5}$ exposure (Butt et al., 2016; Chafe et al., 2014; Conibear et al., 2018; Health Effects Institute, 2018b; Lelieveld et al., 2015; Silva et al., 2016), and Fleming et al. (2018a,b) report characterization of a wide range of particle-phase compounds emitted by cookstoves. In a multi-model evaluation, Pan et al. (2015) concluded that an underestimation of biomass combustion emissions, especially in winter, was the dominant source of model underestimation. Here,

we address both primary and secondary organic particulate matter from household burning of biomass for cooking.
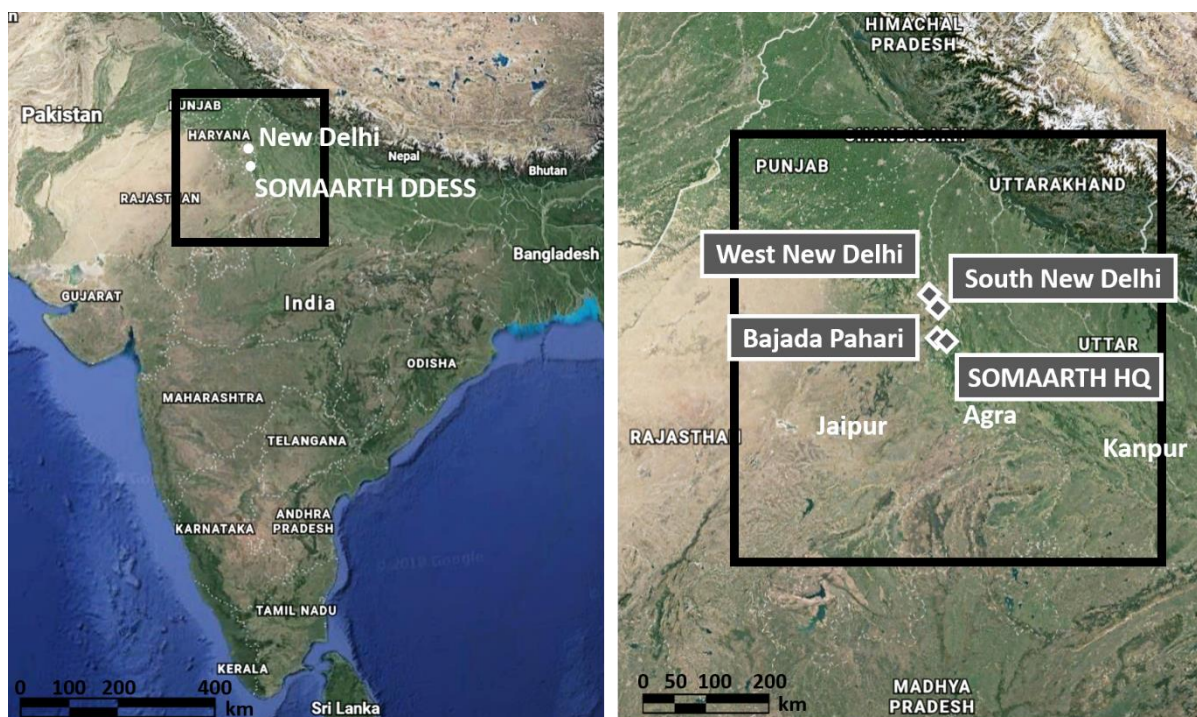
Figure 2.1. Geographic area of simulation. The left panel shows the entirety of India, and the right panel shows a closeup of the model domain. The domain spans a 600 km by 600 km area with a grid resolution of 4 km (150 cells along each axis) and includes both New Delhi and SOMAARTH DDESS.

Air quality in urban areas in India is determined largely, but not entirely, by anthropogenic fuel combustion. In rural areas, residential combustion of biomass for household uses, such as cooking, also contributes to non-methane volatile organic carbon (NMVOC) and particulate emissions (Sharma et al., 2015, 2018). Average daily $PM_{2.5}$ levels frequently exceed the 24-hour Indian standard of 60 µg m^{-3} and can exceed 150 µg m^{-3}, even in rural areas. The local region on which the present study focuses is the SOMAARTH Demographic, Development, and Environmental Surveillance Site (DDESS) run by the International Clinical Epidemiological Network (INCLEN) in the Palwal District of Haryana (Figure 1). Located about 80 km south of New Delhi, SOMAARTH covers an approximate population of 200,000 in 52 villages. Particular focus in the present study is given to the SOMAARTH Headquarters (HQ) and the village of Bajada Pahari within DDESS, coinciding with the work of Fleming et al. (2018b), who studied cookstove non-

methane hydrocarbon (NMHC) emissions and ambient air quality. Demographically, with a coverage of almost 308 sq km, the DDESS has a mix of populations from different religions and socioeconomic and development statuses.

The climate of the region of interest in the present study is primarily influenced by monsoons, with a dry winter and very wet summer. The rainy season, July through September, is characterized by average temperatures around 30 °C and primarily easterly and southeasterly winds. In a study related to the present one, Schnell et al. (2018) used emission datasets developed for the Coupled Model Intercomparison Project Phases 5 (CMIP5) and 6 (CMIP6) to evaluate the impact on predicted $PM_{2.5}$ over Northern India, October-March 2015-2016, with special attention to the effect of meteorology of the region, including relative humidity, boundary layer depth, strength of the temperature inversion, and low level wind speed. In that work, nitrate and organic matter (OM) were predicted to be the dominant components of total $PM_{2.5}$ over most of Northern India.

The goal of the present work is to simulate the distribution of primary and secondary $PM_{2.5}$ and O_3 using recently updated emissions databases and atmospheric chemical transport models to obtain estimates of the total impact on ambient air quality attributable to household combustion. With respect to ozone, the present work follows that of Sharma et al. (2016) who simulated regional and urban ozone concentrations in India using a chemical transport model and included a sensitivity analysis to highlight the effect of changing precursor species on O_3 levels. The present work is based on simulating the levels of both O_3 and $PM_{2.5}$ at the regional level based on recent emissions inventories using state-of-the-science atmospheric chemical transport models.

2.2 Emissions Inventory

Non-Residential Sectors Emissions

The present study uses an emissions inventory conglomerated from two primary sources: (1) an India-scale inventory for all non-residential sectors prepared by TERI (Sharma et al., 2015, 2016) and (2) a high-resolution residential sector inventory detailed here. Emissions data from each source were distributed to a 4 km grid for the present study. The TERI national inventory was prepared at a resolution of 36×36 km^2 using the Greenhouse

Gas and Air Pollution Interactions and Synergies (GAINS ASIA) emission model (Amann et al., 2011). GAINS ASIA estimated emissions based on energy and non-energy sources using an emission factor approach after taking into account various fuel-sector combinations. Following the approach of Kilmont et al. (2002), the emissions were estimated using the basic equation:

$$E_k = \sum_l \sum_m \sum_n A_{k,l,m} ef_{k,l,m}(1 - \eta_{l,m,n}) \cdot X_{k,l,m,n} \qquad (1)$$

where E denotes the pollutant emissions (in kt); k, l, m, and n are region, sector, fuel or activity type, and control technology, respectively; A the activity rate; ef the unabated emission factor (kt per unit of activity); η the removal efficiency (%/100); and X the application rate of control technology n (%/100) where $\sum X = 1$. Energy sources considered include coal, natural gas, petroleum products, biomass fuels, and others and categorized into five sectors – transport, industries, residential, power, and others. The model uses the state-wise energy data and generates emissions of species such as PM, NO_x, SO_2, NMVOCs, NH_3, and CO.

For activity data of source-sectors, TERI employed published statistics (mainly population, vehicle registration, energy use, and industrial production) where possible. Energy use data for industry and power sectors were compiled based on a bottom-up approach, collected from the Ministry of Petroleum and Natural Gas (MoPNG, 2010), the Central Statistics Office (CSO, 2011), and the Central Electricity Authority (CEA, 2011). Transportation activity data were compiled from information on vehicle registrations (Ministry of Road Transport and Highways, 2011), emission standards (MoPNG, 2001), travel demand (CPCB, 2000), and mileage (TERI, 2002). Emission factors for energy-based sources from the GAINS ASIA database were used. Speciation factors are adopted from sector-specific profiles from Wei et al. (2014), primarily developed for China as there is a lack of information for India. In the transportation sector, the Chinese species profiles are dependent on fuel type but not technology.

The TERI inventory was compiled on a yearly basis, with monthly variations for brick kilns and agricultural burning, at a native resolution of 36×36 km^2 then equally distributed to grid resolution of 4×4 km^2 for this study. Emissions for non-residential sectors have no specified diurnal or daily variations; thus, the inventory for non-residential sectors is the

same for each simulated day. Transportation sector emissions were estimated using population and vehicle fleet data at the district level and distributed to the grid using the administrative boundaries. Industry, power, and oil and gas sector emissions were assigned to the grid by their respective locations. Emissions from agriculture were allocated by crop-types produced by state in India. The inventory was vertically distributed to three layers with the lowest layer extending to 30 – 43 m, the middle layer to 75 – 100 m and the top layer to 170 – 225 m layers. VOC emissions were assumed to occur only in the bottom layer. Industry and power emissions were distributed based on stack heights and allocated to the second and third layers.

We incorporated biogenic emissions by using daily-averaged emission rates of isoprene (0.8121 moles s^{-1}) and terpenes (0.8067 moles s^{-1}) per 4 km grid cell, predicted by GEOS-Chem for the region of study. The TERI inventory additionally includes isoprene emissions from the residential sector, so isoprene from natural sources was calculated as the difference of the total rate predicted by GEOS-Chem and the rate of emissions solely from the residential sector. Terpene emissions are assumed to occur only in non-residential source-sectors. Isoprene and terpene emission rates were applied to all computational cells as an hourly average (with no diurnal profile) in the non-residential inventory.

Residential Sector Emissions

To examine local and regional impacts of residential sector emissions in greater detail, an update to the TERI inventory was performed using various sources to consider more granular input data specific to the residential sector (Table 1). Bottom-up estimates of delivered energy for cooking, space heating, water heating, and lighting were informed by those used in Pandey et al. (2014) and converted to fuel consumption at the village level using population size and percentage of reported primary cooking and lighting fuels from the 2011 Census of India (Census of India, 2011). Urban areas of the domain were assumed to have the average cooking and lighting fuel use profiles of the average urban areas of their district. Fuel consumption was converted to emission rates using fuel-specific emission factors informed by a review of field and laboratory studies, which was used to update the Speciated Pollutant Emissions Wizard (SPEW) inventory (Bond et al., 2004) and to generate summary estimates by fuel type. Hourly emissions were generated using

source-specific diurnal emissions profiles (Figure 2). The same diurnal emissions profile is applied to all species from a source category and were informed by real-time emissions measurements taken in homes during cooking reported by Fleming et al. (2018a,b). Profiles for fuel-based lighting were informed by real-time measurements of kerosene lamp usage data reported in Lam et al. (2018). The residential sector inventory represents surface emissions with a native spatial resolution of 30-arc seconds (~1 km).

In deriving summary estimates of emission factors, priority was given to emission factor measurements from field-based studies. Several studies have shown that laboratory-based measurements of stove and lighting emissions tend to be lower than those of devices measured in actual homes (Roden et al., 2009), perhaps due to higher variation in fuel quality and operator behavior. Field-based emission factors utilized in this study include those for non-methane hydrocarbons, measured from fuels and stoves within the study domain (Fleming et al. 2018a,b). $PM_{2.5}$ speciation from cooking fires was informed by Jayarathne et al. (2018) (Tables 2 and 3). Residential emission rates for $PM_{2.5}$, black carbon (BC), organic carbon (OC), CO, NO_x, CH_4, CO_2, and total non-methane hydrocarbons (NMHC) were generated from SPEW, which estimates emissions from combustion by fuel type. As such, solvent emissions are not included for lack of specific input data. Additionally, while SPEW incorporates temperature-dependent heating combustion activity, the inventory assumes temperatures too high for this activity to take effect. Thus, our inventory has no emissions from heating.

We employed various methods to account for pollutant species not explicitly reported by SPEW (Tables 1 and 2). Gas-phase SO_2 and NH_3 emissions were informed by existing residential emissions in the TERI inventory (Sharma et al. 2015); NO and NO_2 were estimated from NO_x emissions assuming a $NO:NO_2$ emission ratio of 10:1. Total NMHC and $PM_{2.5}$ emission factors from SPEW are distributed by fuel type (wood, dung, agriculture residue, or LPG) (Table 2). Given the low $PM_{2.5}$ emission rate of LPG, (Shen et al., 2018), emissions from LPG are assumed to be negligible. To further speciate NMHCs, we employed HC species-specific emission factors (Fleming et al. 2018b), differentiated by fuel and stove type (i.e. traditional stove, or *chulha*, with wood or dung, and simmering stove, or *angithi,* with dung). We assume that all NMHC emissions in each

computational grid cell are produced by either wood or dung, whichever contributes the greater fraction of total PM$_{2.5}$ emissions in that cell (Figure 3). The NMHC emission profile of dung was assumed to be the average of measurements from chulha and angithi stoves. The emission profile for agricultural residue is similar to that of wood; therefore, wood speciation profiles are applied in cells where agricultural residue dominates.

Particle-phase speciation of total PM$_{2.5}$ was based on PM mass emissions from wood- and dung-fueled cooking fires as reported by Jayarathne et al. (2018), and primary cooking fuel type distribution data from the 2011 census (Tables 2 and 3). A single PM$_{2.5}$ speciation profile, defined as the average of that of wood and that of the wood-dung mixture, was applied in all cells for lack of information on pure dung emissions (Table 3). Non-carbon organic particulate matter (PNCOM) and particulate water (PH$_2$O) were assumed to be negligible owing to lack of information on these species. Emissions of remaining particle-phase species (i.e. Al, Ca, Fe, Mg, Mn, Si, and Ti) are also assumed to be negligible for lack of information. Unspeciated fine particulate matter (PM$_{othr}$) is defined in CMAQ as the portion of total PM$_{2.5}$ unassigned to any other species:

$$PM_{othr} = PM_{2.5} - \left(P_{EC} + P_{OC} + P_{Na} + P_{NH_4} + P_K + P_{Cl} + P_{NO_3} + P_{SO_4}\right) \qquad (2)$$

Tables 4 and 5 summarize emission rates for the study domain.
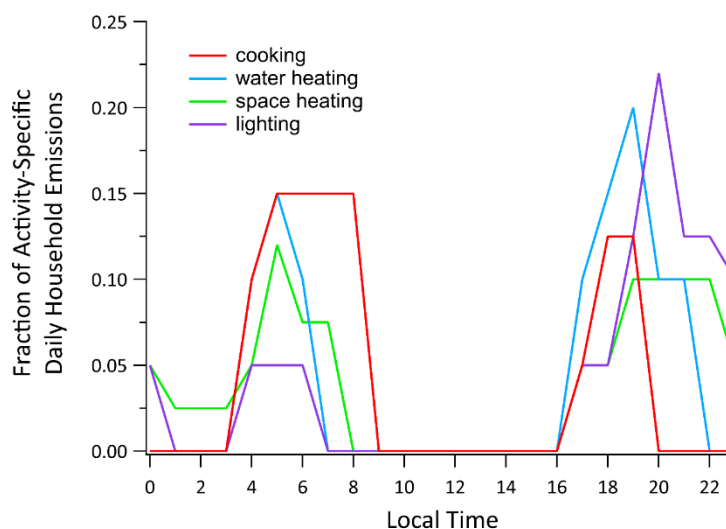
Figure 2.2. Fraction of daily household emissions by quantifiable fuel-use activity. Red, green, blue, and purple indicates cooking, space heating, water heating, and lighting, respectively. This represents the fraction of activity-specific daily emissions at each hour. Each species obeys the same profile. While profiles for heating are shown, the inventory assumes temperatures too high for this activity to take effect.

Table 2.1. Residential Emissions Inventory Sources by Species

	CMAQ Required Species[1]	Source		Solely Emitted by Residential Sector
Gas	NO	T. Bond (University of Illinois) NO_x using Sharma et al. (2015) $NO:NO_2 = 10:1$		No
	NO_2			No
	SO_2	Sharma et al. (2015)		No
	NH_3	Sharma et al. (2015), assumed to be negligible		
	CO	T. Bond (University of Illinois)		No
NMHC	ALD_2	Speciation from T. Bond (University of Illinois) NMHC using Fleming et al. (2018a,b) emission factors		No
	ALD_X			Yes
	ETH			No
	ETHA			No
	ETOH			No
	FORM			No
	MEOH			No
	OLE			No
	$PAR_{calculated}$[3]			No
	TOL			No
	XYL[3]			No
CMAQ AERO6 Species	**ISOP**[2]	All-sector total ISOP emission from GEOS-Chem daily average and subtracted non-residential ISOP emission from Sharma et al. (2015)		No
	TERP[2]	Assumed to be negligible		
	XYLMN	XYLMN = 0.998 * XYL	Pye and Pouliot (2012)	No
	NAPH	NAPH = 0.002 * XYL		No
	PAR_{CMAQ}	$PAR_{CMAQ} = PAR_{calculated} - 0.00001 * NAPH$		No
	SOAALK	SOAALK = 0.108*PAR_{CMAQ}		No
PM	P_{EC}, P_{OC}	T. Bond (University of Illinois)		No
	P_{NA}, P_{CL}	Speciation of $PM_{2.5}$ from T. Bond (University of Illinois) using Jayarathne et al. (2018) mass percentage		Yes
	P_K, P_{NH4}			Yes
	P_{NO3}, P_{SO4}			Yes
	PM_{OTHR}	$PM_{OTHR} = PM_{2.5} - (P_{EC}+ P_{OC}+P_{NA}+P_{NH4}+P_K+P_{CL}+P_{NO3}+P_{SO4})$		No
	PM_C	Sharma et al. (2015)		No
	P_{NCOM} P_{H2O}	Unknown, assumed to be 0		
	$P_{AL}, P_{CA}, P_{FE}, P_{MG}, P_{MN}, P_{SI}, P_{TI}$	Assumed to be negligible		

[1]Bolded species contribute to SOA production via the AERO6 module. [2]Total isoprene and terpene emissions from all sectors are taken from GEOS-Chem and were included only in the O_3

simulations. [3]PAR$_{calculated}$ and XYL are excluded from CMAQ and replaced with PAR$_{CMAQ}$, XYLMN, NAPH, and SOAALK.

Table 2.2. Residential PM$_{2.5}$ and NMHC Emissions Speciation

Emitted Species	Fuel-Specific Data	Use
PM$_{2.5}$ (Bond et al., 2004)	wood, dung, agricultural residue, LPG	Total PM$_{2.5}$ emission rate distributed by wood, dung, and agricultural residue. LPG emissions assumed negligible.
Speciated PM$_{2.5}$ (Jayarathne et al., 2018)	wood, wood/dung mix	Average profile of wood and wood/dung mix applied to all fuel type emissions.
NMHC (Bond et al., 2004)	wood, dung, agricultural residue, LPG	Total PM$_{2.5}$ emission rate distributed by wood, dung, and agricultural residue. LPG emissions assumed negligible.
Speciated HCs (Fleming et al., 2018a,b)	wood, dung	One profile applied to each cell according to which fuel type dominates emissions in that cell. Where agricultural residue dominates, wood profile is assumed.

Table 2.3. PM$_{2.5}$ Speciation by Fuel Type

Emitted Species[1]	% Mass of Total Emitted PM$_{2.5}$		
	Wood[2]	Wood/Dung[2]	Average Employed[3]
P$_{EC}$	14	5.10	9.55
P$_{OC}$	52	61	56.50
P$_{NA}$	0.05	0.39	0.22
P$_{CL}$	3.20	8.58	5.89
P$_{K}$	1.78	0.52	1.15
P$_{NH4}$	1.12	4.46	2.79
P$_{NO3}$	0.42	0.21	0.32
P$_{SO4}$	0.33	0.46	0.40
PM$_{OTHR}$	27.10	19.29	23.19

[1]Total PM$_{2.5}$ mass emission rates from residential combustion were estimated and distributed by fuel type (wood, dung, or agricultural residue) by University of Illinois. [2]Emitted PM$_{2.5}$ weight percent reported by Jayarathne et al. (2018). [3]An average profile applied to all cells, indiscriminate of fuel type.
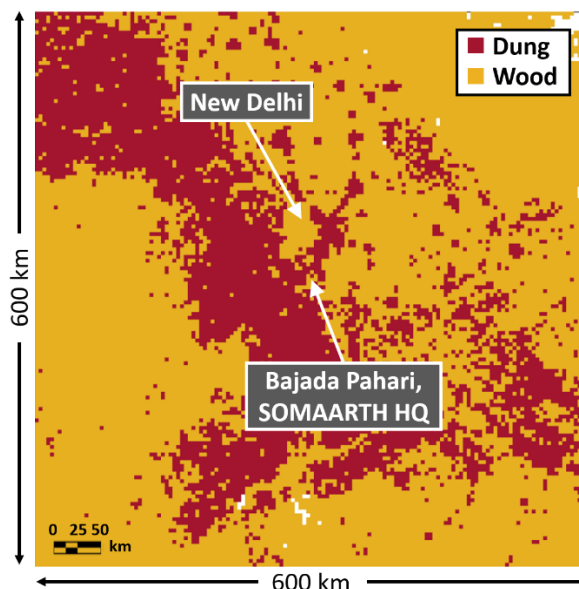
Figure 2.3. Fuel type assumed for speciation of household NMHC emissions. Study domain: 600 by 600 km at 4 km resolution. Red indicates cells where dung use dominated emissions and thus was assumed to be the sole fuel type used. Orange indicates cells where wood and agricultural residue use dominated emissions and was thus assumed to be the sole fuel type used.

Table 2.4. Particulate Matter Surface Emissions over Study Domain

Species		Emission Rate	% Emitted by Residential Sector
Particulate Matter (kg/day)	P_{OC}	1.48×10^6	30.78
	P_{EC}	7.18×10^5	15.89
	P_{CL}	1.69×10^3	100
	P_K	4.61×10^3	100
	P_{NA}	2.46×10^4	10.07
	P_{NH4}	2.11×10^5	1.47
	P_{NO3}	6.51×10^5	27.90
	P_{SO4}	1.18×10^6	61.45
	PM_C	9.00×10^3	100
	PM_{OTHR}	2.18×10^4	100
SOA Precursor VOCs (mol/day)	NAPH	6.82×10^3	2.72
	SOAALK	3.75×10^6	34.54
	TOL	1.54×10^6	27.21
	XYLMN	3.40×10^6	2.72

Table 2.5. Mealtime[1] Particulate Matter Surface Emissions over Corresponding 16 km^2 Grid Cell and the Fraction from the Residential Sector.

Species		Bajada Pahari		SOMAARTH HQ		New Delhi	
		Total	% Res	Total	% Res	Total	% Res
Particulate Matter (kg/day)	P_{OC}	35.17	67.13	36.04	100	609.73	5.70
	P_{EC}	10.22	33.23	6.02	100	346.84	2.21
	P_{CL}	2.19	100	3.40	100	3.40	100
	P_K	0.43	100	0.66	100	0.66	100
	P_{NA}	0.08	100	0.12	100	0.12	100
	P_{NH4}	1.037	100	1.61	100	1.61	100
	P_{NO3}	0.37	32.01	0.18	100	12.59	1.45
	P_{SO4}	2.49	5.90	0.23	100	116.80	0.20
	PM_C	63.99	91.94	72.56	100	275.99	7.12
	PM_{OTHR}	13.92	61.94	13.37	100	276.91	4.83
SOA Precursor VOCs (mol/day)	NAPH	0.11	6.50	0.03	59.56	3.78	0.65
	SOAALK	112.31	50.62	113.20	77.95	1696.26	11.14
	TOL	43.88	42.28	39.38	71.05	750.00	1.04
	XYLMN	56.47	6.50	13.03	59.56	1886.15	0.65

[1]Mealtimes are assumed to be 4 am – 10 am and 4 pm – 8pm (local).

2.3 Atmospheric Modeling

To study the impact of household emissions on ambient air pollution, we simulated two emission scenarios each for three time periods which coincide with available INCLEN observation data (Tables 6 and 7). A "total" emission scenario represents the overall atmospheric environment by including emissions from all source-sectors in the inventory. A "non-residential" emission scenario represents zeroing-out or "turning-off" all household emissions. By considering these scenarios independently, we can isolate the effect of the residential sector on the ambient atmosphere. Each scenario was simulated over a region in northern India (Figure 1) for those periods when measurements were carried out in the region of interest. Figure 1 shows the 600 km by 600 km domain with 4 km grid resolution. The domain is centered over the Palwal District and the SOMAARTH DDESS and includes New Delhi and portions of surrounding states.

Simulation of regional air quality was carried out using the U.S. Environmental Protection Agency Community Multiscale Air Quality modeling system (CMAQ), version 5.2 (Appel et al., 2017; US EPA, 2017). CMAQ is a three-dimensional chemical transport model (CTM) that predicts the dynamic concentrations of airborne species. CMAQ includes

modules of radiative processes, aerosol microphysics, cloud processes, wet and dry deposition, and atmospheric transport. Required input to the model includes emissions inventories, initial and boundary conditions, and meteorological fields. The domain-specific, gridded emissions inventory provides hourly-resolved total emission rates for each species (not differentiated by source) by cell, timestep, and vertical layer. Initial conditions (ICs) and boundary conditions (BCs) are necessary to define the atmospheric chemical concentrations in the domain at the first time step and at the domain edges, respectively. Simulations operating with nested domains require two groups of initial conditions and boundary conditions. The present study uses the global chemical transport model GEOS-Chem v11-02c (acmg.seas.harvard.edu/geos/index.html) to generate concentrations on the boundary of the computational domain and CMAQ to produce initial and boundary conditions for the inner parent domain and nested domain, respectively. Meteorological conditions (including temperature, relative humidity, wind speed and direction and land use and terrain data) drive the atmospheric processes represented in CMAQ. The Weather Research and Forecasting modeling system (WRF) – Advanced Research WRF (WRF-ARW, version 3.6.1), was used to simulate the meteorological input for CMAQ (Skamarock et al., 2008).

GEOS-Chem

We used GEOS-Chem v11-02c, a global chemical transport model driven by assimilated meteorological observations from the NASA Goddard Earth Observing System -- Fast Processing (GEOS-FP) of the Global Modeling and Assimilation Office (GMAO), to simulate the boundary conditions for the CMAQ modeling. Simulations are performed at 2˚x2.5˚ horizontal resolution with 72 vertical layers, including both the full tropospheric chemistry with complex SOA formation (Marais et al., 2016) and UCX stratospheric chemistry (Eastham et al., 2014). Emissions used the standard HEMCO configuration (Keller et al., 2014), including EDGAR v4.2 anthropogenic emissions (http://edgar.jrc.ec.europa.eu/overview.php?v=42), biogenic emissions from the MEGAN v2.1 inventory (Guenther et al., 2012), and GFED biomass burning emissions (http://www.globalfiredata.org). Simulations were run for 1 year, after which hourly time series diagnostics were compiled for the CMAQ modeling period. Using the

PseudoNetCDF processor, we remapped a subset of the 616 GEOS-Chem-produced species to CMAQ species (https://github.com/barronh/pseudonetcdf). The resulting ICs and BCs include 119 gas- and particle-phase species, 80 adapted from GEOS-Chem and the remaining 39 (including OH, HO_2, ROOH, oligomerized secondary aerosols, coarse aerosol, and aerosol number concentration distributions) from the CMAQ default initial and boundary conditions data (which were developed to represent typical clean-air pollutant concentrations in the United States).

Weather Research and Forecasting (WRF) Model

Three monthly WRF version 3.6.1 simulations were conducted in the absence of nudging or data assimilation. The large-scale forcing to generate initial and boundary meteorological fields is adopted from the latest version of the European Centre for Medium-Range Weather Forecasts (ECMWF) ERA5 released in January 2019. These reanalysis data are on a 31 km grid and resolve the atmosphere using 137 levels from the surface to a height of 80 km. WRF simulations were performed with 4 km horizontal resolution and 24 vertical layers (the lowest layer of about 50 m depth), consistent with the setup of the CMAQ model. No cumulus parameterization was used in the simulations. Meteorological outputs from WRF were prepared as inputs to CMAQ by the Meteorology-Chemistry Interface Processor (MCIP) version 4.4 (Otte et al., 2010).

Community Multiscale Air Quality (CMAQ) Modeling System

Within the chemical transport portion of CMAQ, there are two primary components: a gas-phase chemistry module and an aerosol chemistry, gas-to-particle conversion module. The present study employs a CMAQ-adapted gas-phase chemical mechanism, CB6R3 (derived from the Carbon Bond Mechanism 06) (Yarwood et al., 2010), and the aerosol-phase mechanism, AERO6, which define the gas-phase and aerosol-phase chemical resolution. The present study considers 70 non-methane hydrocarbon (NMHC) compounds lumped into 12 groups of volatile organic compounds (VOCs). The emissions inventory provides emission rates for 28 chemical species, including 18 gas-phase species and 10 particle-phase species. The CB6R3 adaptation describes atmospheric oxidant chemistry with 127 gas-phase species and 220 gas-phase reactions, including chlorine and heterogenous

reactions. The CMAQ aerosol module (AERO6) describes aerosol chemistry and gas-to-particle conversion with 12 traditional SOA precursor classes, and 10 semi-volatile primary organic aerosol (POA) precursor reactions. The majority of the gas-phase organic species are apportioned to lumped groups by their carbon bond characteristics, such as single bonds, double bonds, ring structure, and number of carbons. Some organic compounds are apportioned based on reactivity, and others, like isoprene, ethene, and formaldehyde, are treated explicitly.

The secondary organic aerosol module, AERO6, developed specifically for CMAQ, interfaces with the gas-phase mechanism, predicts microphysical processes of emission, condensation, evaporation, coagulation, new particle formation, and chemistry, and produces a particle size distribution comprising the sum of the Aitken, Accumulation, and Coarse log-normal modes (Figure 4). AERO6 predicts the formation of SOA from anthropogenic and biogenic volatile organic compound (VOC) precursors (properties of which are shown in Table 8), as well as semi-volatile POA and cloud processes. CB6R3 accounts for the oxidation of the first-generation products of the anthropogenic lumped VOCs: high-yield aromatics, low-yield aromatics, benzene, PAHs, and long-chain alkanes (Pye and Pouliot, 2012).

In addition to SOA formation from traditional precursors, CMAQv5.2 accounts for the semi-volatile partitioning and gas-phase aging of POA using the volatility basis set (VBS) framework independently from the rest of AERO6 (Murphy et. al., 2017). The module distributes directly emitted POA (as the sum of primary organic carbon, POC, and noncarbon organic matter, NCOM) from the emissions inventory input into five new emitted species grouped by volatility: LVPO1, SVPO1, SVPO2, and SVPO3, and IVPO1 (where LV is low volatility, SV is semi-volatile, IV is intermediate volatility, and PO is primary organic). POA is apportioned to these lumped vapor species using an emission fraction and are oxidized in CB6R3 by OH to LVOO1, LVOO2, SVOO1, SVOO2, and SVOO3 (where OO denotes oxidized organics) with stoichiometric coefficients derived from the 2D-VBS model. AERO6 then partitions the semi-volatile primary organics and their oxidation products to the aerosol phase (Figure 4). Thus, the treatment of POA as

semi-volatile products leads to an additional twenty species, a particle- and vapor-phase component for each primary organic and oxidation product (Murphy et al., 2017).
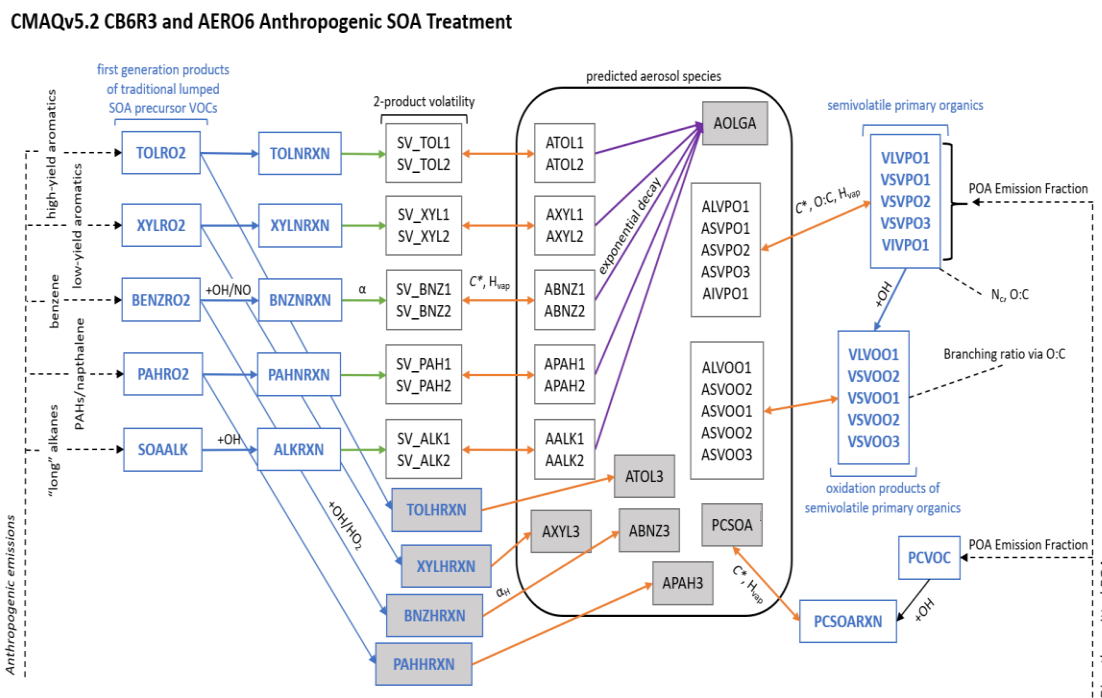
Figure 2.4. Treatment of anthropogenic SOA in CMAQv5.2. Predicted aerosol species are included in the black box. Species in white boxes are semi-volatile and species in gray boxes are nonvolatile. Blue indicates species and processes predicted by CB6R3. All other coloring indicates the AERO6 mechanism where green arrows are 2-product volatility distribution, orange arrows are particle- and vapor-phase partitioning, and purple arrows are oligomerization. In AERO6, anthropogenic and biogenic VOC emissions (lumped by category), are oxidized by OH, NO, and HO_2 and OH, O_3, NO, and NO_3 respectively, to semi-volatile products that undergo partitioning to the particle phase (Pye et al., 2015). Semi-volatile primary organic pathways in CMAQv5.2 are described by Murphy et al. (2017).

Emissions inventory modifications were required to match the most recent aerosol module, AERO6, in the CMAQ model. Initially, the lumped emissions of PAR (a lumped VOC group characterized by alkanes) and XYL (a lumped VOC group characterized by xylene) derived from grouping specific NMHCs, calculated using the University of Illinois estimation and the Fleming et al. (2018a) emission factors, accounted for characteristics of naphthalene (NAPH) and SOA-producing alkanes (SOAALK), which are not individually described by any of the sources used to construct the inventory. Moreover, only a subset of VOCs in the plume could be measured. However, CMAQv5.2 simulations incorporate

a surrogate species, potential secondary organic aerosol from combustion emissions (pcSOA), to address sources of missing SOA, including unspeciated emissions of semivolatile and intermediate volatility organic compounds. AERO6 predicts the formation of SOA from NAPH and SOAALK independently as well as from XYL and PAR; these secondary aerosol precursor emission rates are calculated with:

$$XYLMN = 0.998 * XYL \tag{3}$$

$$NAPH = 0.002 * XYL \tag{4}$$

$$PAR_{CMAQ} = PAR_{calculated} - 0.00001 * NAPH \tag{5}$$

$$SOAALK = 0.108 * PAR_{CMAQ} \tag{6}$$

where XYLMN, NAPH, PARCMAQ, and SOAALK are the new inventory species (Pye and Pouliot, 2012). SOA-producing alkanes are treated separately in AERO6.

Table 2.8. Properties of anthropogenic traditional semi-volatile SOA precursors in CMAQv5.2

SOA species	Precursor	Oxidants	Semi-volatile	α (mass-based)	C* (μg/m^3)	ΔH_{vap} (kJ/mol)	# of C	Molecular weight (g/mol)	OM/OC
AALK1	long-chain alkanes	OH	SV_ALK1	0.0334	0.15	53.0	12	168	1.17
AALK2	long-chain alkanes	OH	SV_ALK2	0.2164	51.9	53.0	12	168	1.17
AXYL1	XYLMN	OH,NO	SV_XYL1	0.0310	1.3	32.0	8	192	2.0
AXYL2	XYLMN	OH,NO	SV_XYL2	0.0900	34.5	32.0	8	192	2.0
AXYL3	XYLMN	OH,HO$_2$	nonvolatile	0.36	NA	NA	NA	192	2.0
ATOL1	TOL	OH,NO	SV_TOL1	0.0310	2.3	18.0	7	168	2.0
ATOL2	TOL	OH,NO	SV_TOL2	0.0900	21.3	18.0	7	168	2.0
ATOL3	TOL	OH,HO$_2$	nonvolatile	0.30	NA	NA	NA	168	2.0
ABNZ1	benzene	OH,NO	SV_BNZ1	0.0720	0.30	18	6	144	2.0
ABNZ2	benzene	OH,NO	SV_BNZ2	0.8880	111	18	6	144	2.0
ABNZ3	benzene	OH,HO$_2$	nonvolatile	0.37	NA	NA	NA	144	2.0
APAH1	naphthalene	OH,NO	SV_PAH1	0.2100	1.66	18	10	243	2.03
APAH2	naphthalene	OH,NO	SV_PAH2	1.0700	265	18	10	243	2.03
APAH3	naphthalene	OH,HO$_2$	nonvolatile	0.73	NA	NA	NA	243	2.03

The semi-volatile reaction products of "long alkanes" (SV_ALK1 and SV_ALK2) are parameterized by Presto et al. (2010). Values for "low-yield aromatics" products (SV_XYL1 and SV_XYL2) are based on xylene, with the enthalpy of vaporization (ΔH_{vap}) from studies of m-xylene and 1,3,5-trimethylbenzene. ΔH_{vap} for products of "high-yield aromatics" (SV_TOL1 and SV_TOL2) are based on the higher end of the range for toluene. The products of benzene (SV_BNZ1 and SV_BNZ2) assume the same value for ΔH_{vap}. All semi-volatile aromatic products are assigned stoichiometric yield (α) and effective saturation concentration (C*) values from laboratory measurements by Ng et al. (2007). Remaining parameters for PAH reaction products (SV_PAH1 and SV_PAH2) are taken from Chan et al. (2009). Properties of semi-volatile primary organic aerosol precursors are given in Murphy et al. (2017).

2.4 Surface Observational Data

Gas-phase air quality data analyzed in the present study come from the Central Pollution Control Board (CPCB) of the Ministry of Environment, Forest & Climate Change, Government of India at two sites in New Delhi (one in the west, and one in the south). Particle-phase data analyzed come from the SOMAARTH Demographic, Development, and Environmental Surveillance Site (Mukhopadhyay et al., 2012; Pillarisetti et al., 2014; Balakrishnan et al., 2015) managed by the International Clinical Epidemiological Network (INCLEN). Palwal District has a population of ~ 1 million over an area of 1400 km^2. In this district, ~39% of households utilize wood burning as their primary cooking fuel, with dung (~25%) and crop residues (~7%) (Census of India, 2011). Specific sites studied are the SOMAARTH headquarters (HQ) in Aurangabad (15 km south of Palwal) and the village of Bajada Pahari (8 km northwest of SOMAARTH HQ). Ambient measurement sites are shown in Fig. 1, and Table 6 details available data for each location. We used meteorological data (hourly surface temperature and near-surface wind speed and direction) from INCLEN and CPCB at the two rural and two urban sites, respectively, to evaluate the WRF simulations performance.

Table 2.6. Ambient Observation Data Availability

Location (Grid Cell)	PM$_{2.5}$	O$_3$
Bajada Pahari[1] (74,74)	12/20/15 – 12/31/15 9/19/16 – 9/30/16	n/a
SOMAARTH HQ[1] (75,74)	9/22/15 – 9/27/15 9/23/16 – 9/30/16	n/a
West New Delhi[2] (71,91)	9/7/15 – 9/30/15 12/7/15 – 12/31/15 9/7/16 – 9/30/16	9/7/15 – 9/30/15 12/7/15 – 12/31/15
South New Delhi[2] (71,89)	9/7/15 – 9/30/15 12/7/15 – 12/31/15 9/7/16 – 9/30/16	9/7/15 – 9/30/15 12/7/15 – 12/31/15 9/7/16 – 9/30/16

[1]Data from the International Epidemiological Clinical Network. Observations at Bajada Pahari are the average of two monitoring locations that coincide within the same grid cell.
[2]Data from the Central Pollution Control Board of India at New Delhi Punjabi Bagh monitoring station.

2.5 Simulation Results

WRF Evaluation

We evaluated WRF simulated meteorology against the available surface observations at different sites during the same periods. Figure 5 shows that there is generally good agreement of surface temperature between WRF and observations for all three months. The surface wind direction is found consistent between model and observations for each site and each month (Table 9). The simulated near-surface wind speeds are overestimated in WRF, with an averaged mean-bias (MB) of about +1.5 m/s. Such a bias is partly a result of the difference in the definition of "near-surface" between the model and observations.
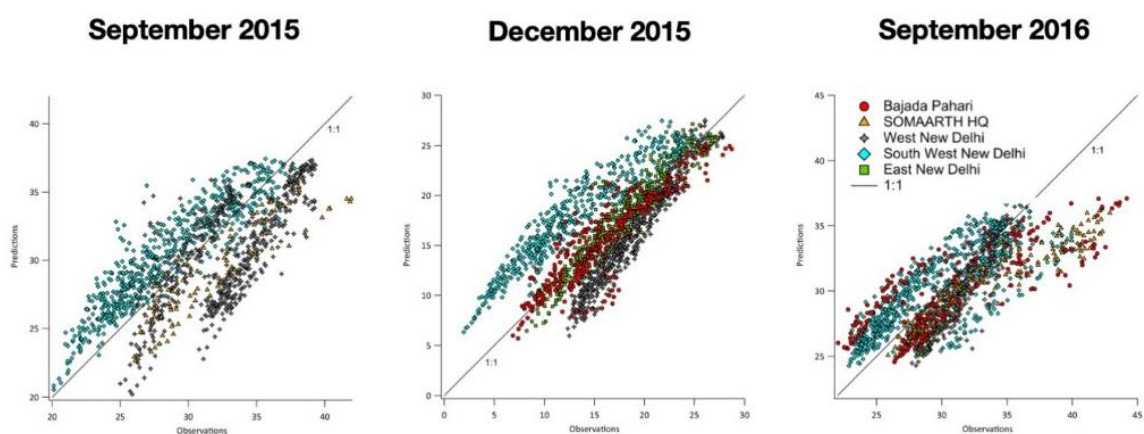
Figure 2.5. Evaluation of WRF simulated meteorological fields versus ground observations.

Particulate Matter

Figures 6–9 show measured and predicted total $PM_{2.5}$ and the average diurnal profile at each site for the periods with available measurements. The diurnal profile in these figures includes that of both emission scenarios: the total scenario with all emissions and the non-residential scenario with zeroed-out residential sector. The simulations capture the general trend well and produce significant diurnal profiles (Table 10). Rural sites show typical $PM_{2.5}$ levels are predicted between 50 µg m^{-3} and 125 µg m^{-3} in December and 25 µg m^{-3} and 75 µg m^{-3} in September months (Figures 6 and 7). On the other hand, typical values at urban sites range from 100 µg m^{-3} to 300 µg m^{-3} in December and 50 µg m^{-3} to 125 µgm^{-3}

Table 2.9. Quantification of WRF model biases in meteorological fields.

		Bajada Pahari			SOMAARTH HQ			West New Delhi			South New Delhi		
		Sep 2015	Dec 2015	Sep 2016	Sep 2015	Dec 2015	Sep 2016	Sep 2015	Dec 2015	Sep 2016	Sep 2015	Dec 2015	Sep 2016
Temp. (°C)	PRE	-	15.28 (4.59)	30.10 (3.19)	29.27 (3.48)	-	30.22 (3.06)	30.45 (3.79)	16.59 (4.91)	30.07 (3.05)	30.32 (3.74)	17.59 (4.82)	29.96 (30.3)
	OBS	-	15.62 (4.91)	30.86 (5.67)	32.15 (4.12)	-	33.26 (5.31)	32.80 (3.60)	19.04 (3.66)	31.46 (2.33)	28.48 (4.30)	12.58 (5.52)	29.22 (4.22)
	MB	-	-0.34	-0.76	-2.89	-	-3.04	-2.35	-2.45	-1.38	1.84	5.02	0.74
	ME	-	1.60	3.08	2.92	-	3.07	3.03	2.58	1.54	2.11	5.02	2.37
	RMSE	-	2.20	3.71	3.39	-	3.99	3.58	2.99	1.88	2.50	5.33	2.75
Wind Speed (m·s^{-1})	PRE	-	2.91 (1.17)	2.31 (1.07)	-	-	2.01 (0.66)	-	-	2.57 (1.28)	2.80 (1.27)	2.72 (1.08)	2.74 (1.39)
	OBS	-	1.18 (0.75)	0.73 (0.40)	-	-	0.55 (0.30)	-	-	1.03 (0.51)	1.26 (0.83)	0.94 (0.71)	1.18 (0.79)
	MB	-	1.72	1.58	-	-	1.46	-	-	1.54	1.54	1.77	1.56
	ME	-	1.75	1.62	-	-	1.50	-	-	1.58	1.61	1.82	1.62
	RMSE	-	1.96	1.85	-	-	1.66	-	-	1.88	1.85	2.01	1.84
Wind Direction (°)	PRE	-	247 (111)	116 (45)	272 (70)	-	111 (51)	-	-	179 (98)	206 (118)	254 (97)	191 (96)
	OBS	-	259 (57)	102 (41)	255 (58)	-	110 (48)	-	-	181 (97)	198 (45)	224 (44)	228 (50)
	MB	-	0.14	14	16	-	-0.14	-	-	-6	9	35	-34
	ME	-	51	38	44	-	32.71	-	-	49	94	74	75
	RMSE	-	66	51	64	-	47.50	-	-	64	106	87	90

PRE is mean predictions; OBS is mean observations; MB is mean bias; ME is mean error; and RMSE is root mean square error. Standard deviation of predictions and observations are noted in parentheses.

in September months (Figures 8 and 9). Observations and predictions show higher $PM_{2.5}$ levels in December than September, owing to frequent temperature inversions in winter and shallower planetary boundary layers. Two daily peaks and lows of $PM_{2.5}$ compare with ambient observations at Bajada Pahari December 2015 and September 2016, SOMAARTH HQ September 2015 and 2016, West New Delhi December 2015, and South New Delhi December and September 2015. Average daily $PM_{2.5}$ levels regularly exceed the 24-hour Indian standard of 60 µg m^{-3} in each month in both rural and urban locations, surpassing even double the standard in the village of Bajada Pahari during mealtimes in December. Afternoon minima tend to be underestimated in September 2015 and December 2015. Diurnal trends of $PM_{2.5}$ were weaker in September 2016 than the other months, with lower predictions but overestimated minima. Urban sites show greater overestimation than rural sites. This is likely due in part to the granularity of the primary emissions inventory datasets. The non-residential sector was prepared from data with a native resolution of 36 km, while the residential sector used data with ~1 km resolution. Underpredictions of peak $PM_{2.5}$ concentrations in September could also result because the emission inventory does not account for day-to-day variations, especially in the agricultural burning sector in which emissions can change significantly on a daily basis. Observed and predicted $PM_{2.5}$ levels in New Delhi can exceed 300 µg m^{-3}, especially in winter. In this highly populated urban environment, particulate matter levels are more than double those reported in the nearby rural areas. The employed emissions inventory specifies particulate matter surface emissions, which surpass those of Bajada Pahari and SOMAARTH HQ more than 30-fold (Table 5). Biogenic emissions are predicted to be of little importance, accounting for less than 10% on average of total $PM_{2.5}$ concentrations for most stations and months (Table 10).
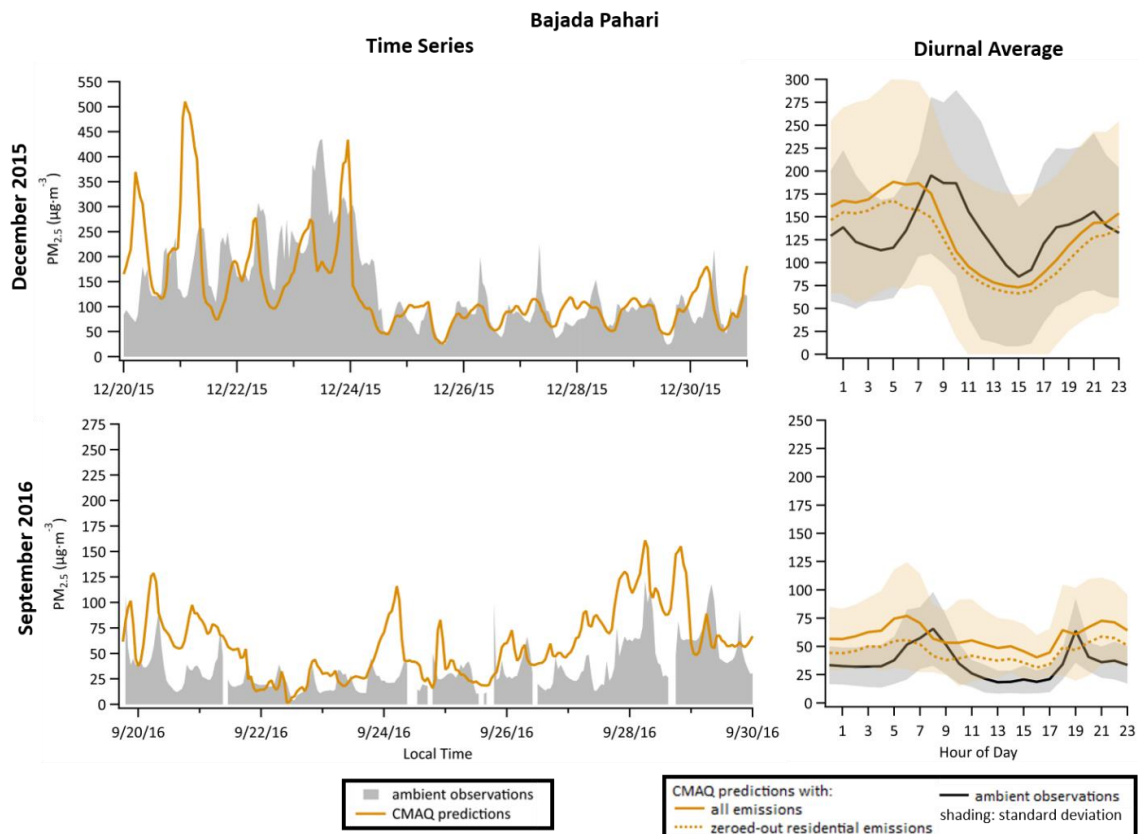
Figure 2.6. Measured and predicted PM$_{2.5}$ (left) and average diurnal cycle (right) in Bajada Pahari for 12/20/15 – 12/31/15 (top) and 09/20/16 – 09/30/16 (bottom). Here the yellow lines correspond to CMAQ predictions of the "total" (solid) and "non-residential" (dotted) simulations. The solid black line represents ambient observations. Standard deviations of the diurnal profiles for observations and predictions are indicated, respectively, by colored shading. Diurnal profiles were averaged over simulation durations (Table 7). Computations were carried out at 4 km resolution.
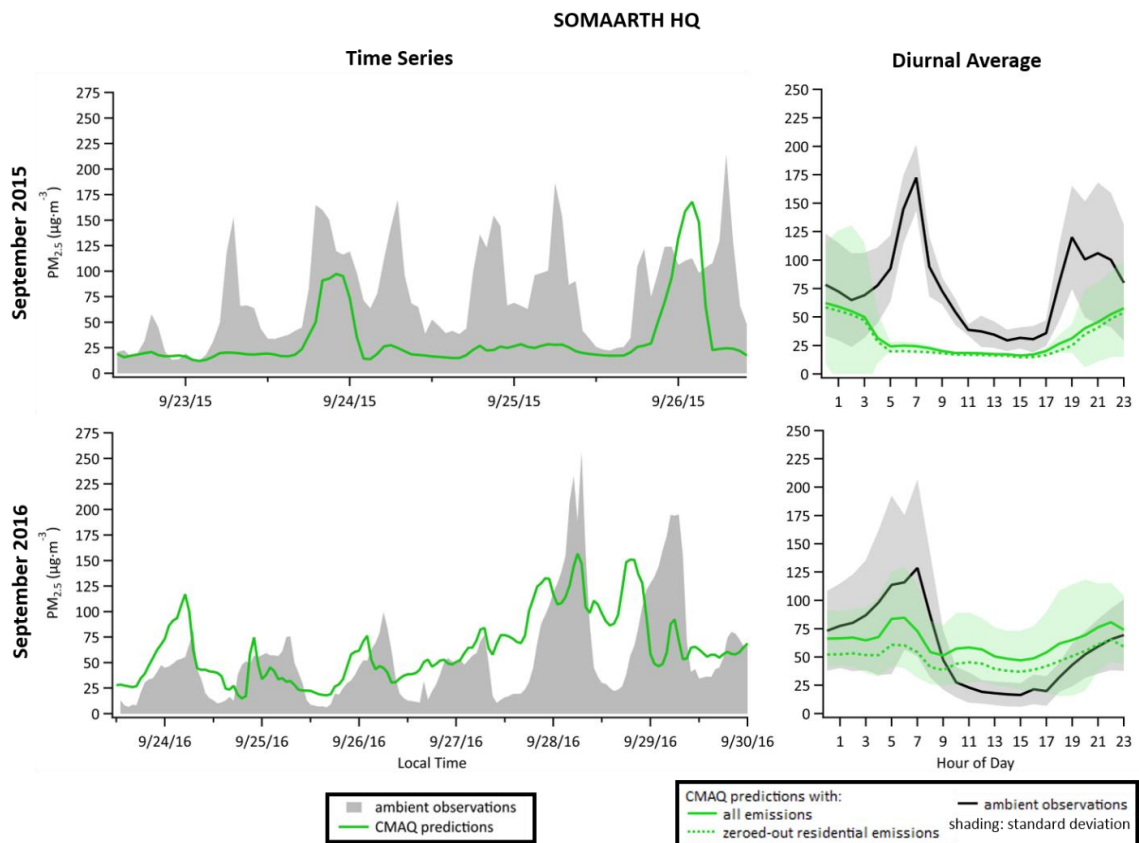
Figure 2.7. Measured and predicted PM$_{2.5}$ (left) and average diurnal cycle (right) at SOMAARTH HQ for 12/20/15 – 12/31/15 (top) and 09/20/16 – 09/30/16 (bottom). Here the green lines correspond to CMAQ predictions of the "total" (solid) and "non-residential" (dotted) simulations. The solid black line represents ambient observations. Standard deviations of the diurnal profiles for observations and predictions are indicated, respectively, by colored shading. Diurnal profiles were averaged over simulation durations (Table 7). Computations were carried out at 4 km resolution.
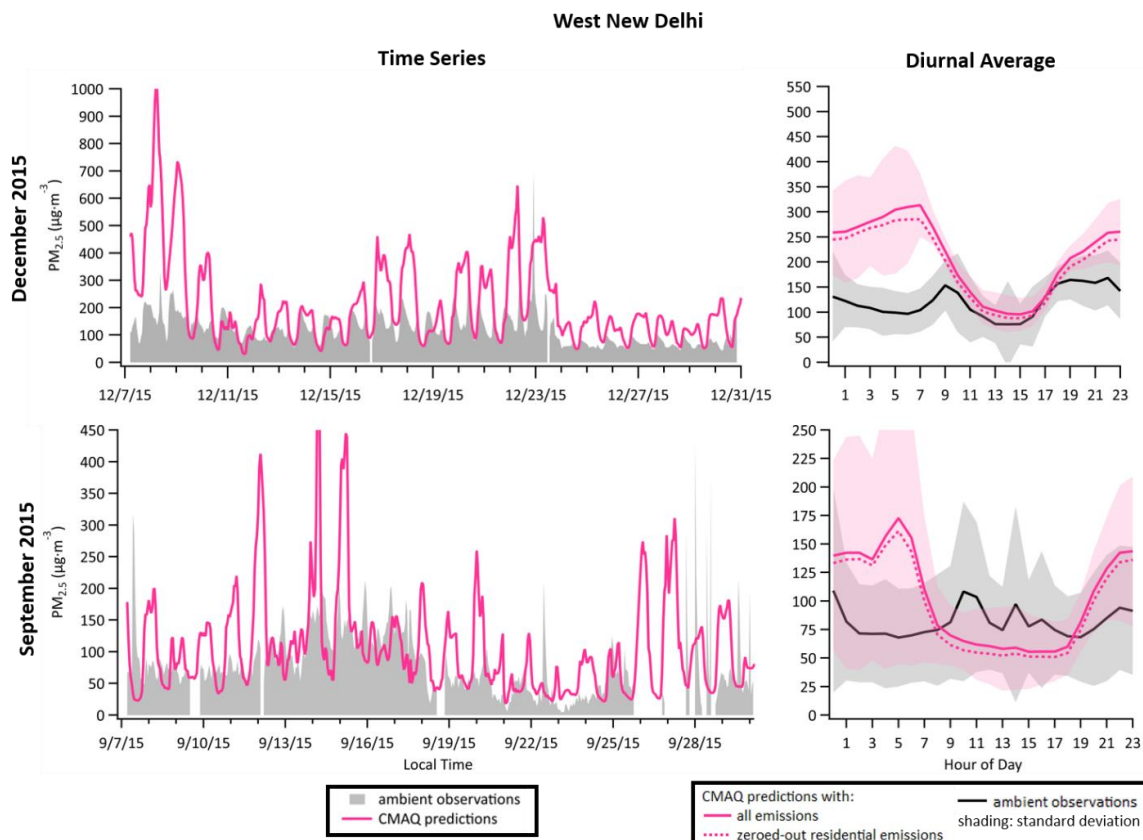
Figure 2.8. Measured and predicted PM$_{2.5}$ (left) and average diurnal cycle (right) in West New Delhi for 12/20/15 – 12/31/15 (top) and 09/20/16 – 09/30/16 (bottom). Here the pink lines correspond to CMAQ predictions of the "total" (solid) and "non-residential" (dotted) simulations. The solid black line represents ambient observations. Standard deviations of the diurnal profiles for observations and predictions are indicated, respectively, by colored shading. Diurnal profiles were averaged over simulation durations (Table 7). Computations were carried out at 4 km resolution.
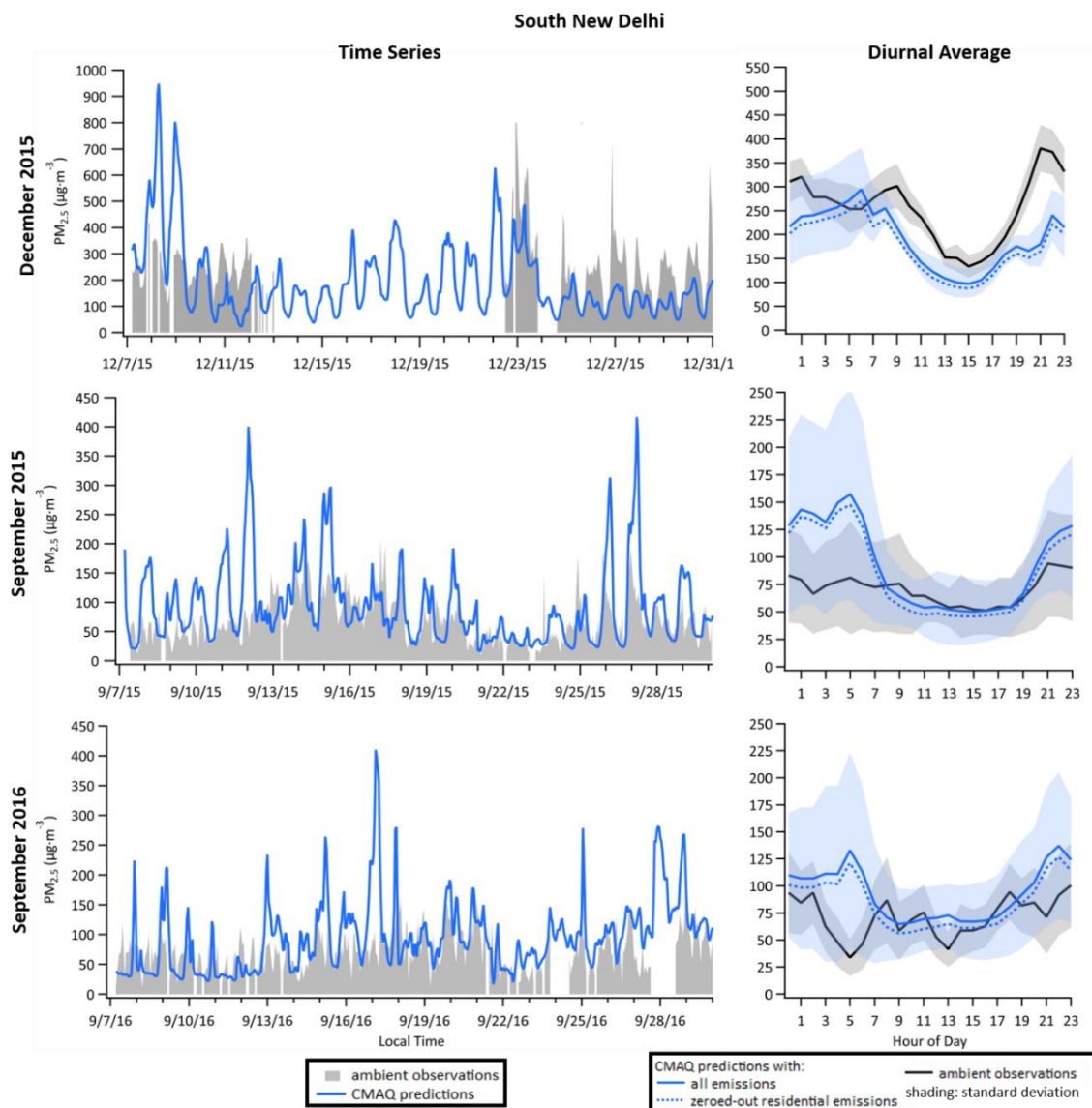
South New Delhi

Figure 2.9. Measured and predicted PM$_{2.5}$ (left) and average diurnal cycle (right) in South New Delhi for 12/20/15 – 12/31/15 (top) and 09/20/16 – 09/30/16 (bottom). Here the blue lines correspond to CMAQ predictions of the "total" (solid) and "non-residential" (dotted) simulations. The solid black line represents ambient observations. Standard deviations of the diurnal profiles for observations and predictions are indicated, respectively, by colored shading. Diurnal profiles were averaged over simulation durations (Table 7). Computations were carried out at 4 km resolution.

Table 2.10. CMAQ Model Performance and Summary Statistics.

		Bajada Pahari			SOMAARTH HQ			West New Delhi			South New Delhi		
		Dec '15	Sep '15	Sep '16	Dec '15	Sep '15	Sep '16	Dec '15	Sep '15	Sep '16	Dec '15	Sep '15	Sep '16
$PM_{2.5}$	PRE	133.49	54.83	59.22	131.80	32.16	63.66	212.29	101.71	106.44	191.35	92.68	92.85
		(40.66)	(21.24)	(9.89)	(42.81)	(15.99)	(11.24)	(75.55)	(41.49)	(28.58)	(61.03)	(39.46)	(24.37)
	OBS	136.01	-	35.55	-	75.83	58.03	120.49	81.53	-	254.15	70.24	70.97
		(28.35)	-	(13.76)	-	(37.16)	(35.19)	(29.92)	(12.72)	-	(70.89)	(13.04)	(18.72)
	MB	-2.52	-	23.67	-	-43.67	5.64	91.80	20.19	-	-62.81	22.44	21.88
	ME	35.20	-	24.66	-	43.67	25.04	91.93	41.02	-	67.67	26.42	25.71
	RMSE	40.23	-	26.35	-	56.23	27.71	115.76	48.60	-	81.02	37.50	35.37
O_3	PRE	72.76	80.72	47.24	71.83	80.75	47.22	32.59	57.14	31.66	40.90	62.76	36.29
		(39.47	(3.87)	(17.56)	(39.99)	(34.06)	(17.60)	(41.34)	(53.36)	(30.16)	(44.87)	(53.52)	(29.89)
	OBS	-	-	-	-	-	-	21.74	71.09	-	43.57	59.47	29.28
		-	-	-	-	-	-	(8.05)	(42.41)	-	(37.07)	(36.30)	(20.27)
	MB	-	-	-	-	-	-	10.93	-13.95	-	-2.67	3.29	7.01
	ME	-	-	-	-	-	-	16.83	18.74	-	12.62	24.72	19.29
	RMSE	-	-	-	-	-	-	22.96	22.10	-	14.08	27.64	23.31
SOA	PRE	44.60	17.89	23.30	44.81	18.06	22.95	44.22	23.76	33.28	43.95	22.44	31.78
		(7.76)	(2.40)	(3.96)	(7.59)	(2.34)	(3.77)	(3.76)	(4.74)	(8.80)	(3.82)	(4.11)	(7.84)
F_{bio}	PRE	0.09	0.18	0.08	0.09	0.18	0.08	0.04	0.06	0.04	0.04	0.03	0.05
		(0.03)	(0.10)	(0.02)	(0.03)	(0.11)	(0.02)	(0.01)	(0.01)	(0.01)	(0.01)	(0.01)	(0.01)
$F_{SOA,res}$	PRE	0.15	0.24	0.26	0.15	0.24	0.26	0.13	0.15	0.16	0.13	0.16	0.16
		(0.02)	(0.05)	(0.04)	(0.02)	(0.05)	(0.04)	(0.03)	(0.02)	(0.03)	(0.03)	(0.02)	(0.03)
$F_{an,res}$	PRE	0.12	0.16	0.20	0.12	0.17	0.20	0.07	0.08	0.09	0.07	0.08	0.10
		(0.03)	(0.04)	(0.03)	(0.03)	(0.04)	(0.04)	(0.02)	(0.03)	(0.02)	(0.02)	(0.03)	(0.02)
$F_{res,SOA}$	PRE	0.48	0.51	0.52	0.47	0.50	0.52	0.43	0.51	0.55	0.45	0.53	0.54
		(0.16)	(0.20)	(0.18)	(0.16)	(0.21)	(0.18)	(0.18)	(0.21)	(0.17)	(0.18)	(0.22)	(0.17)

Statistics are calculated for average diurnal profiles of predicted parameters. $PM_{2.5}$, O_3, and SOA are the mass concentrations in µg m^{-3} of total fine particulate matter, ozone, and secondary organic matter, respectively. F_{bio} is the fraction of total $PM_{2.5}$ that is produced by biogenic emissions; $F_{SOA,res}$ is the fraction of total secondary organic matter attributable to the residential sector; $F_{an,res}$ is the fraction of total anthropogenic $PM_{2.5}$ attributable to the residential sector; and $F_{res,SOA}$ is the fraction of residential $PM_{2.5}$ attributable to SOA. PRE is mean predictions; OBS is mean observations; MB is mean bias; ME is mean error; and RMSE is root mean square error. Standard deviation of predictions and observations are noted in parentheses.

Figure 10 shows CMAQ predictions of secondary organic $PM_{2.5}$ (SOA). Like $PM_{2.5}$, SOA is typically predicted to be higher in New Delhi than in the rural sites, due to higher $PM_{2.5}$ and precursor VOC emissions and ambient concentrations in urban environments (Tables 5 and 6). Higher levels are similarly attained in December than in September due to longer residence times and more aging during winter. SOA has high day-to-day variability. Values range from below 20 µg m^{-3} to over 200 µg m^{-3} in December, with average peaks up to 55 µg m^{-3} at the rural sites. September months predict lower SOA, ranging from 10 µg m^{-3} to 130 µg m^{-3}. Diurnal average SOA maxima in December for the rural stations is nearly double that of September 2016, which can be attributed to temperature inversions and a shallower planetary boundary layer in winter.

The significance of household emissions on outdoor $PM_{2.5}$ concentrations is demonstrated by the diurnal profiles in Figure 11. The top row of plots shows the predicted contribution of the residential sector to anthropogenic $PM_{2.5}$, while the middle row of plots describes the predicted contribution of the residential sector to secondary organic $PM_{2.5}$, as in Equations 7 and 8 respectively:

$$\frac{\text{Residential Anthropogenic } PM_{2.5}}{\text{Total Anthropogenic } PM_{2.5}} \tag{7}$$

$$\frac{\text{Residential SOA}}{\text{Total SOA}} \tag{8}$$

The bottom row of plots shows the predicted SOA portion of residential $PM_{2.5}$, as

$$\frac{\text{Residential SOA}}{\text{Residential } PM_{2.5}} \tag{9}$$

where residential PM is calculated as the difference in predictions from the non-residential and total emission scenario and averaged over simulation durations (Table 7). Importance of household emissions to ambient PM is strongly correlated with mealtimes. Predicted maximum contributions to anthropogenic $PM_{2.5}$ in Bajada Pahari and SOMAARTH HQ are about double that of South and West New Delhi for each month. Household energy-use is estimated to account for up to 27% of anthropogenic $PM_{2.5}$ (at SOMAARTH HQ during September 2016), remaining consistently above 10% for each rural site during all months. Similar behavior is predicted for SOA (middle plots of Fig. 11). An estimated 15% to 34% of secondary organic matter is attributable to residential emissions in September

and 2016. Again, the impact is smaller in West and South New Delhi (up to 19% and 21%, respectively in September 2016), where there are greater emissions of SOA precursor from precursors from other sectors. The diurnal profile of the contribution to SOA is subdued for all sites in December, suggesting that SOA generation is less efficient in winter when radiation and temperatures are lower. Aging of VOCs is captured by the phase shift of the impact on SOA daily trend, where peaks consistently occur an hour after the residential sector shows greatest importance to anthropogenic $PM_{2.5}$.

At each measurement site during all months, SOA is predicted to make up more than 40% of $PM_{2.5}$ produced by the residential sector on average (bottom row of plots of Fig. 11). SOA is least significant to residential $PM_{2.5}$ in the first half of mealtimes (~20% during breakfast and ~40% during dinner) at rural sites, when primary particulate matter is largest. Aging of precursor VOCs from cooking emissions, paired with maximum incoming radiation, lead to maximum $\frac{\text{Residential SOA}}{\text{Residential PM}_{2.5}}$ values in early afternoon, when SOA accounts for more than 75% of residential $PM_{2.5}$ at both rural and urban sites during each simulated month.

The fractional contribution of total SOA to total $PM_{2.5}$ is shown in Fig. 12. While concentrations of SOA depend significantly on the site and time period, their contribution to total $PM_{2.5}$ shows little variation. At all stations, SOA is predicted to make up to 55% of $PM_{2.5}$ in September months and to be most significant around midday. However, diurnal variation of the significance of SOA is greater in New Delhi than in Bajada Pahari or SOMAARTH HQ, owing to greater diversity of energy-use activities and emissions characteristics in the urban environment.

Table 2.7. Simulation Durations

CMAQ[1]	09/07/15 - 09/30/15	12/07/15 - 12/31/15	09/07/16 - 09/30/16
WRF[2] (Meteorology)	09/02/15 - 09/30/15	12/02/15 - 12/31/15	09/02/16 - 09/30/16
GEOS-Chem[3] (Boundary Conditions)	09/07/15 - 09/30/15	12/07/15 - 12/31/15	09/07/16 - 09/30/16

[1]Five days prior to date shown were run and omitted from analysis as spinup. [2]One day prior to date shown was run and omitted from analysis as spinup. [3]GEOS-Chem was run for one year before extracting atmospheric diagnostics.
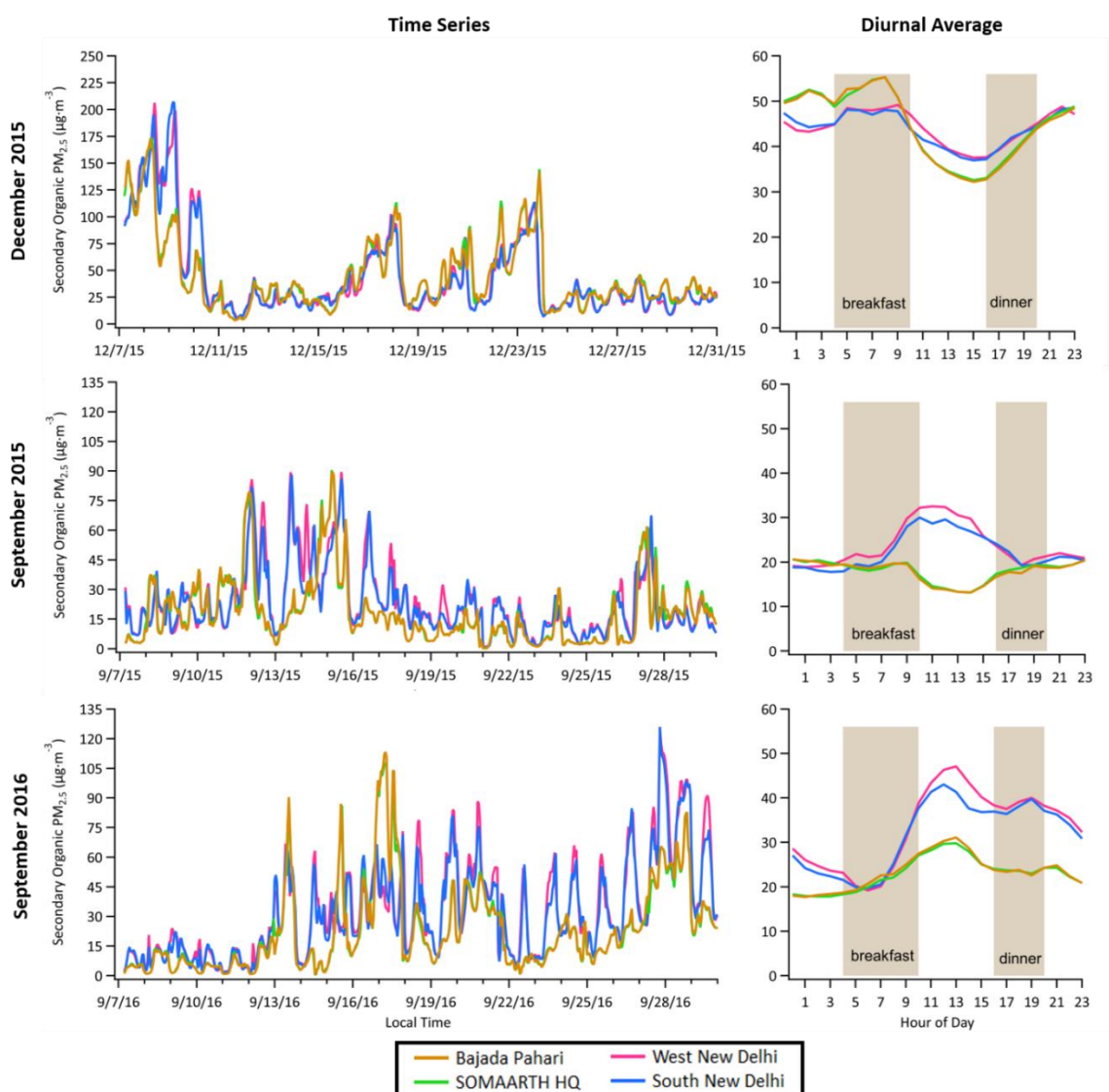
Figure 2.10. Predicted secondary organic PM$_{2.5}$ (left) and average diurnal cycle (right) for 12/20/15 – 12/31/15 (top), 09/07/09/30/15 (middle), and 09/20/16 – 09/30/16 (bottom). Bajada Pahari is shown in yellow, SOMAARTH HQ in green, West New Delhi in pink, and South New Delhi in blue. Diurnal profiles were averaged over simulation durations (Table 7). Computations were carried out at 4 km resolution. Statistics are shown in Table 10.
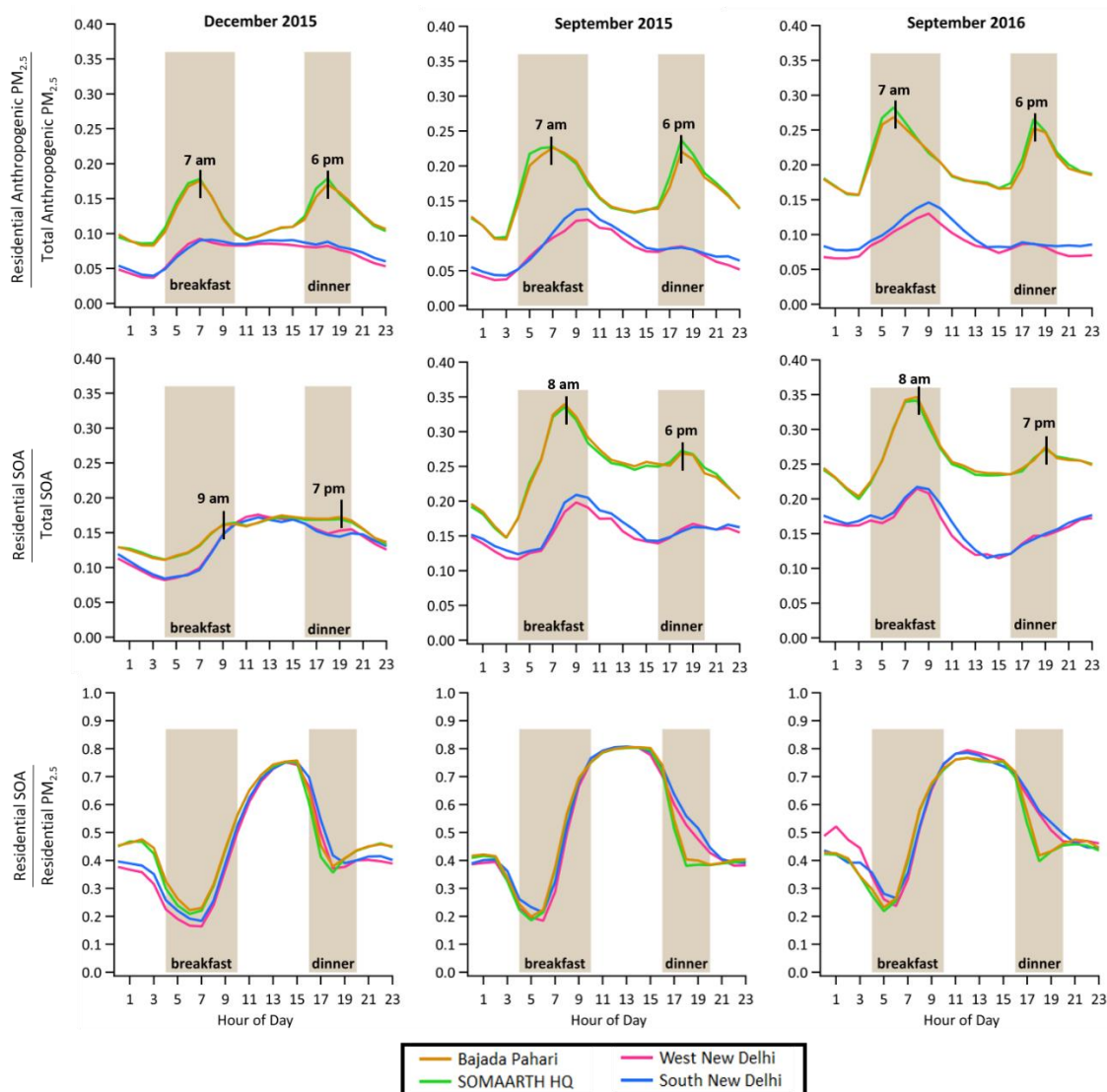
Figure 2.11. Average diurnal $\frac{\text{Residential Anthropogenic PM}_{2.5}}{\text{Total Anthropogenic PM}_{2.5}}$ (top), $\frac{\text{Residential SOA}}{\text{Total SOA}}$ (middle), and $\frac{\text{Residential SOA}}{\text{Residential PM}_{2.5}}$ (bottom). Bajada Pahari is shown in yellow, SOMAARTH HQ in green, West New Delhi in pink, and South New Delhi in blue. Shading indicates mealtimes. Residential PM is calculated as the difference in predictions from the non-residential and total emission scenario and averaged over simulation durations (Table 7). Computations were carried out at 4 km resolution. Statistics are shown in Table 10.
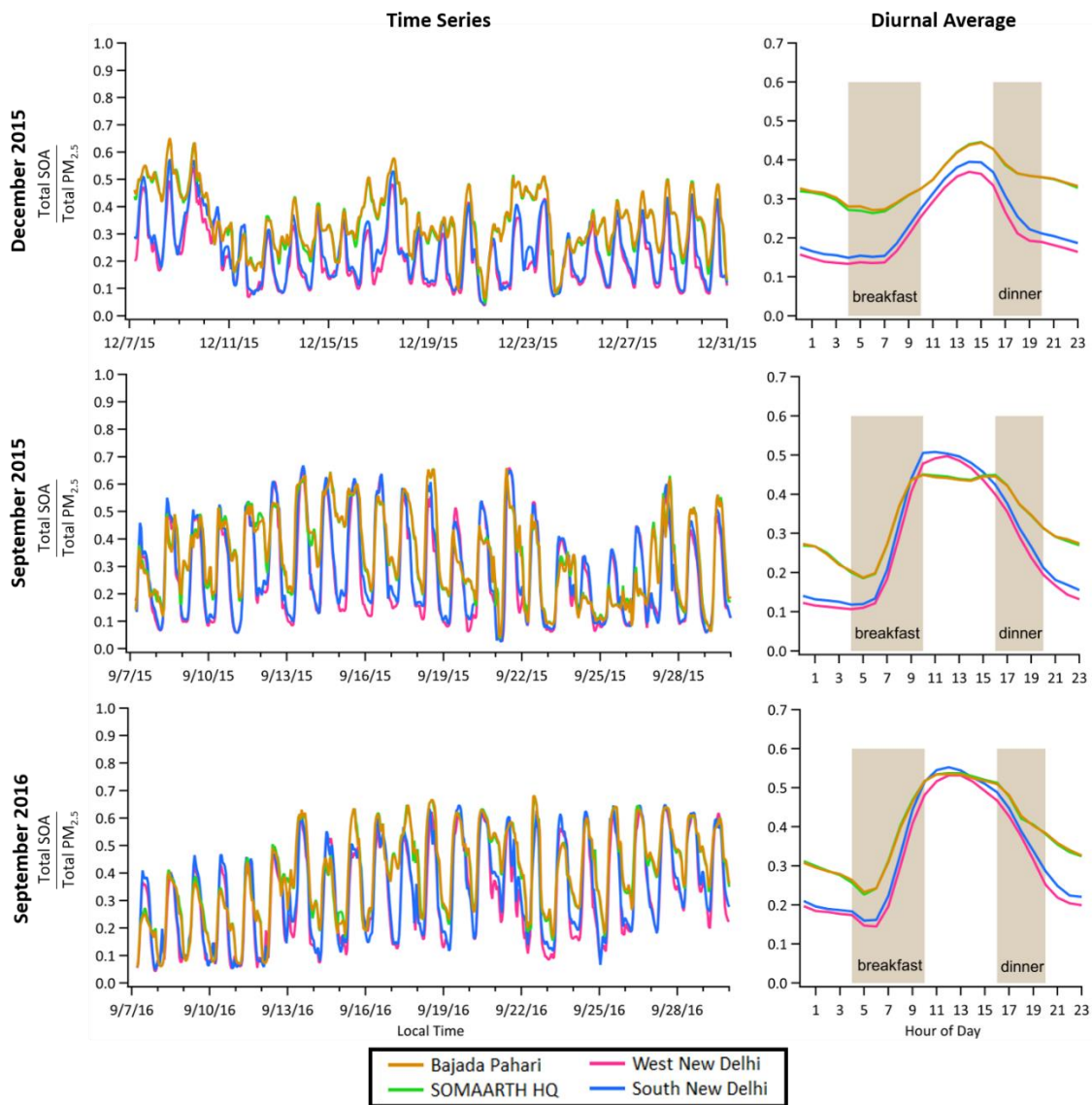
Figure 2.12. Predicted $\frac{\text{Total SOA}}{\text{Total PM}_{2.5}}$ (left) and average diurnal cycle (right) for 12/20/15 – 12/31/15 (top), 09/07/09/30/15 (middle), and 09/20/16 – 09/30/16 (bottom). Bajada Pahari is shown in yellow, SOMAARTH HQ in green, West New Delhi in pink, and South New Delhi in blue. Diurnal profiles were averaged over simulation durations (Table 7). Computations were carried out at 4 km resolution.

Ozone

The 8-hour India Central Pollution Control Board (CPCB) standard for ozone is 100 µg m^{-3} for an 8-hour average. In the alternative unit of ozone mixing ratio, a mass concentration of ozone of 100 µg m^{-3} at a temperature of 298 K at the Earth's surface equates to a mixing ratio of 51 parts-per-billion (ppb). A number of atmospheric modeling studies of ozone over India exist (Kumar et al., 2010; Chatani et al., 2014; Sharma et al., 2016).

Sharma et al. (2016) carried out baseline CMAQ simulations for 2010 and compared ozone predictions with measurements at six monitoring locations in India (Thumba, Gadanki, Pune, Anantpur, Mt. Abu, and Nainital). Also carried out were sensitivity simulations in which each emissions sector (transport, domestic, industrial, power, etc.) was systematically set to zero. The domestic sector was predicted to contribute ~60% of the non-methane volatile organic carbon emissions, followed by 12% from transportation and 20% from solvent use and the oil and gas sector. The overall NO_x-to-VOC mass ratio in the region simulated by Sharma et al. (2016) was 0.55. This exceptionally low NO_x-to-VOC ratio was attributed, in part, to the widespread use of biomass fuel for cooking (leading to high VOC emissions), coupled with relatively low NO_x emissions. (Although vehicle emissions are high in urban areas, overall vehicle ownership is relatively low at the national level. In addition, Euro equivalent norms have led to reduction of NO_x emissions.) Predicted O_3 levels at the six observation sites tended to exceed measured values, with the ratio of predicted to observed annual average O_3 being in the range of 1.04–1.37 at the six locations. Moreover, the overall low NO_x-to-VOC ratios in India lead to NO_x-sensitive O_3 formation conditions. Based on emissions inventories, the overall anthropogenic NMVOC/NO_x mass emissions ratio in India in 2010 as computed by Sharma et al. (2016) was 1.82. Considering only ground-level sources, the ratio increases to 3.68.

Ozone surface measurements and predicted mass concentrations based on the CMAQ 4 km resolution simulations at two sites in New Delhi over the periods 9/7/2015 – 9/29/2015, 12/7/2015 – 12/30/2015, and 9/7/2016 – 9/29/2016 in the present study are shown in the three panels in Fig. 13. The predicted O_3 concentrations are reproduced well at the West New Delhi and South New Delhi stations, especially in September (Table 10). However,

when NO concentrations are higher due to meteorological inversion conditions, ozone concentrations are underestimated, as local $NO+O_3$ titration reactions near the monitoring site are not resolved. The performance of the model improves in prediction of higher values of ozone (as in the case of September), which are of greater importance for assessing exposures. High ozone concentrations in September are quite well reproduced by the model. This shows that, on the larger scale, the model captures photochemistry quite well; however, micro-scale titration is not well represented due to the limitations of inventory resolution. This would require further enhancement of emission inventories at even higher resolution. The results of ozone simulations in the present study are generally consistent with those of previous simulations over India. For example, also using WRF-CMAQ, Kota et al. (2018) showed that the relative bias in ozone simulation ranges from −30% to +50% in major cities of India. In South New Delhi, the bias in O_3 predictions in the present study lies between -2.67 and +7.01 µg m^{-3}, as compared to the observations of 29.28 to 62.76 µg m^{-3}.
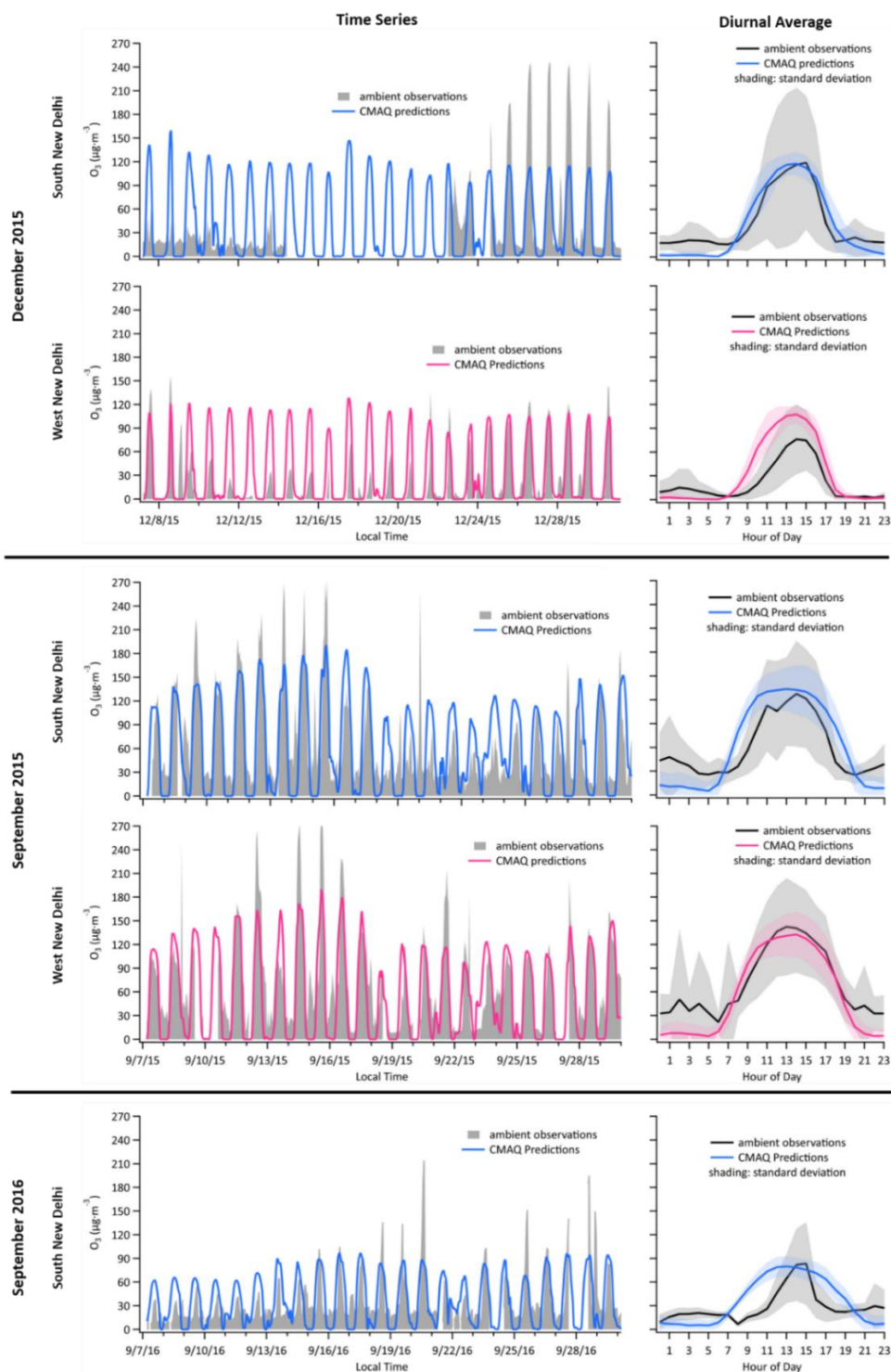
Fig. 2.13. Predicted O₃ (left) and average diurnal cycle (right) for 12/20/15 – 12/31/15 (top), 09/07/09/30/15 (middle), and 09/20/16 – 09/30/16 (bottom) in West New Delhi (pink), and South New Delhi (blue). Standard deviations of the diurnal profiles for observations and predictions are indicated, respectively, by colored shading. Diurnal profiles were averaged over simulation durations (Table 7). Computations were carried out at 4 km resolution.

2.6 Conclusions

Air quality in India is determined by a mixture of industrial and motor vehicle emissions, and anthropogenic fuel combustion, that includes residential burning of biomass for household uses, such as cooking. Average daily $PM_{2.5}$ levels frequently exceed the 24-hour standard of 60 µg m^{-3} and can exceed 200 µg m^{-3}, even in rural areas. $PM_{2.5}$ is a mixture of directly-emitted particulate matter and that formed by the atmospheric conversion of volatile organic compounds to secondary organic aerosol. Here, we assess the extent to which observed O_3 and $PM_{2.5}$ levels in India can be predicted using state-of-the-science emissions inventories and atmospheric chemical transport models. We have focused on the 308 sq km of the SOMAARTH Demographic, Development, and Environmental Surveillance Site (DDESS) in the Palwal District of Haryana, India.

Atmospheric simulation of particulate matter levels over a complex region like India tends to be demanding, owing to the combination of a wide range of primary particulate emissions and the presence of secondary organic matter from atmospheric gas-phase reactions generating low-volatility gas-phase products that condense into the particulate phase, forming secondary organic aerosol (SOA). Consequently, the main focus of the present work has been the evaluation of the extent to which ambient particulate matter levels over the current region of India can be predicted. Simulations capture the general trend of observed daily peaks and lows of particulate matter, with $PM_{2.5}$ reaching values as high as 250 µg m^{-3}. Secondary organic matter accounts for 10% to 55% of total $PM_{2.5}$ mass on average. In India, over 50% of households report use of wood, crop residues, or dung as cooking fuel; such fuels produce significant gas- and particle-phase emissions. We evaluated the fractional impact of the residential sector emissions on the formation of secondary organic aerosol, as a function of time of day, for New Delhi, SOMAARTH HQ, and Bajada Pahari. The predicted fractional contribution of residential sector emissions to secondary organic $PM_{2.5}$ in Bajada Pahari and SOMAARTH HQ reaches values as high as 34% and, moreover, displays a distinct diurnal profile, with maxima corresponding to the morning and evening mealtimes. In both rural and urban areas, SOA is predicted to account

for more than 40% of residential $PM_{2.5}$, reaching up to 80% in early afternoon in September months.

Simulations of ozone levels in New Delhi reported here are largely in agreement with ambient monitoring data, although the simulations fail to capture several one- to two-day ozone episodes that exceed predictions by a factor of two or more. The overall agreement between observed and predicted O_3 levels, also demonstrated in the study of Sharma et al. (2016), suggests that gas-phase atmospheric chemistry over India is reasonably well understood. While ozone and particulate matter were simulated for September and December months, we employed a single emissions inventory, regardless of season. Thus, the inventory does not capture December-specific characteristics, including heating combustion. Furthermore, information regarding household solvent use, emissions profiles by fuel type, and speciation of certain emissions (such as semi volatile organic compounds and intermediate volatility organic compounds) is lacking. Variation in the resolution of specific input data additionally contributes to uncertainty.

Air quality studies such as the present one provide a quantification of the elements of atmospheric composition in India, especially that owing to household sources. The importance of replacing traditional household combustion devices with modern technology is evident in studies such as the present one.

References

Amann, M., Bertok, I., Borken-Kleefeld, J., Cofala, J., Heyes, C., Hoeglund-Isaksson, L., Klimont, Z., Nguyen, B., Posch, M., Rafaj, P., Sandler, R., Schoepp, W., Wagner, F., Winiwarter, W., 2011. Cost-effective control of air quality and greenhouse gases in Europe: modeling and policy applications. Environ. Model. Softw. 26 (12), 1489.

Appel, K. W., Napelenok, S. L., Foley, K. M., Pye, H. O. T., Hogrefe, C., Luecken, D. J., Bash, J. O., Roselle, S. J., Pleim, J. E., Foroutan, H., Hutzell, W. T., Pouliot, G. A., Sarwar, G., Fahey, K. M., Gantt, B., Gilliam, R. C., Heath, N. K., Kang, D. W., Mathur, R., Schwede, D. B., Spero, T. L., Wong, D. C., and Young, J. O.: Description and evaluation of the Community Multiscale Air Quality (CMAQ) modeling system version 5.1, Geosci. Model Dev., 10, 1703–1732, 2017.

Balakrishnan, K., Sambandam, S., Ghosh, S., Mukhopadhyay, K., Vaswani, M., Arora, N. K., Jack, D., Pillarisetti, A., Bates, M. N., and Smith, K. R.: Household air pollution

exposures of pregnant women receiving advanced combustion cookstoves in India: Implications for intervention, Ann. Glob. Health, 81, 375–385, 2015.

Bond, T. C., Streets, D. G., Yarber, K. F., Nelson, S. M., Woo, J.-H., and Klimont, Z.: A technology-based global inventory of black and organic carbon emissions from combustion, J. Geophys. Res., 109, D14203, 2004.

Bonjour, S., Adair-Rohani, H., Wolf, J., Bruce, N. G., Mehta, S., Prüss-Ustün, A., Lahiff, M., Rehfuess, E. A., Mishra, V., and Smith, K. R.: Solid fuel use for household cooking: Country and regional estimates for 1980-2010, Environ. Health Persp., 121, 784–790, 2013.

Butt, E., W., Rap, A., Schmidt, A., Scott, C. E., Pringle, K. J., Reddington, C. L., Richards, N. A. D., Woodhouse, M. T., Ramirez-Villegas, J., Yang, H., Vakkari, V., Stone, E. A., Rupakheti, M., Praveen, P. S., Van Zyl, P. G., Beukes, J. P., Josipovic, M., Mitchell, E. J. S., Sallu, S. M., Forster, P. M., and Spracklen, D. V.: The impact of residential combustion emissions on atmospheric aerosol, human health, and climate, Atmos. Chem. Phys., 16, 873–905, 2016.

Cao, G., Zhang, X., and Zheng, F.: Inventory of black carbon and organic carbon emissions from China, Atmos. Environ., 40, 6516–6527, 2006.

Census of India, http://www.censusof india.gov.in/2011census/Hlo-series/HH10, 2011.

Chafe, Z. A., Brauer, M., Klimont, Z., Van Dingenen, R., Mehta, S., Rao, S., Riahi, K., Dentener, F., and Smith, K. R.: Household cooking with solid fuels contributes to ambient $PM_{2.5}$ air pollution and the burden of disease, Environ. Health Persp., 122, 1314–1320, 2014.

Chan, A. W. H., Kautzman, K. E., Chhabra, P. S., Surratt, J. D., Chan, M. N., Crounse, J. D., Kurten, A., Wennberg, P. O., Flagan, R. C., and Seinfeld, J. H.: Secondary organic aerosol formation from photooxidation of naphthalene and alkylnaphthalenes: implications for oxidation of intermediate volatility organic compounds (IVOCs), Atmos. Chem. Phys., 9, 3049–3060, 2009.

Chatani, S., Amann, M., Goel, A., Hao, J., Klimont, Z., Kumar, A., Mishra, A., Sharma, S., Wang, S. X., Wang, Y. X., and Zhao, B.: Photochemical roles of rapid economic growth and potential abatement strategies on tropospheric ozone over South and East Asia in 2030, Atmos. Chem. Phys., 14, 9529–9277, 2014.

CEA, 2011. Performance Review of Thermal Power Stations 2009e10. Central Electricity Authority, New Delhi.

Conibear, L., Butt, E. W., Knote, C., Arnold, S. R., and Spracklen, D. V.: Residential energy use emissions dominate health impacts from exposure to ambient particulate matte in India, Nat. Commun., 9, 1–9, 2018.

CPCB, 2000. Transport Fuel Quality 2005. Central Pollution Control Board, New Delhi.

CSO, 2011. Energy statistics, 2011. Central Statistics Office, New Delhi.

Derwent, R. G., Jenkin, M. E., Utembe, S. R., Shallcross, D. W., Murrells, T. P., and Passant, N. R.: Secondary organic aerosol formation from a large number of reactive man-made compounds, Sci. Total Environ., 408, 3374–3381, 2010.

Eastham, S. D., Weisenstein, D. K., and Barrett, S. R. H.: Development and evaluation of the unified tropospheric-stratospheric chemistry extension (UCX) for the global chemistry-transport model GEOS-Chem, Atmos. Environ., 89, 52–63, 2014.

Edwards, R., Princevac, M., Weltman, R., Ghasemian, M., Arora, N. K., and Bond, T.: Modeling emission rates and exposures from outdoor cooking, Atmos. Environ., 164, 50–60, 2017.

Fleming, L. T., Lin, P., Laskin, A., Laskin, J., Weltman, R., Edwards, R. D., Arora, N. K., Yadav, A., Meinardi, S., Blake, D. R., Pillarisetti, A., Smith, K. R., and Nizkorodov, S. A.: Molecular composition of particulate matter emissions from dung and brushwood burning cookstoves in Haryana, India, Atmos. Chem. Phys., 18, 2461–2489, 2018a.

Fleming, L. T., Weltman, R., Yadav, A., Edwards, R. D., Arora, N. K., Pillarisetti, A., Meinardi, S., Smith, K. R., Blake, D. R., and Nizkorodov, S. A.: Emissions from village cookstoves in Haryana, India and their potential impacts on air quality, Atmos. Chem. Phys. 18, 15169–15182, 2018b.

Guenther, A. B., Jiang, X., Heald, C. L., Sakulyanontvittaya, T., Duhl, T., Emmons, L. K., and Wang, X.: The Model of Emissions of Gases and Aerosols from Nature version 2.1 (MEGAN2.1): an extended and updated framework for modeling biogenic emissions, Geosci. Model Dev., 5, 1471–1492, 2012.

Health Effects Institute: State of Global Air 2018. Special Report, www.stateofglobalair.org/report, 2018a.

Health Effects Institute: Burden of Disease Attributable to Major Air Pollution Sources in India, Special Report 21, GBD MAPS Working Group, https://www.healtheffects.org/publication/gbd-air-pollution-india, 2018b.

Indian Council of Medical Research, Public Health Foundation of India, and Institute for Health Metrics and Evaluation: GBD India Compare Data Visualization, http://vizhub.healthdata.org/gbd-compare/india, 2017.

Jayarathne, T., Stockwell, C. E., Bhave, P. V., Praveen, P. S., Rathnayake, C. M., Islam, M. R., Panday, A. K., Adhikari, S., Maharjan, R., Goetz, J. D., DeCarlo, P. F., Saikawa, E., Yokelson, R. J., and Stone, E. A.: Nepal Ambient Monitoring and Source Testing Experiment (NAMaSTE): Emissions of particulate matter from wood and dung cooking fires, garbage and crop residue burning, brick kilns, and other sources, Atmos. Chem. Phys., 18, 2259–2286, 2018.

Jena, C., Ghude, S. D., Beig, G., Chate, D. M., Kumar, R., Pfister, G. G., Lal, D. M., Surendran, D. E., Fadnavis, S., and van der A, R. J.: Inter-comparison of different NO_x emission inventories and associated variation in simulated surface ozone in Indian region, Atmos. Environ., 117, 61–73, 2015.

Keller, C. A., Long, M. S., Yantosca, R. M., Da Silva, A. M., Pawson, S., and Jacob, D. J.: HEMCO v1.0: a versatile, ESMF-compliant component for calculating emissions in atmospheric models, Geosci. Model Dev., 7, 1407–1417, 2014.

Kleindienst, T. E., Lewandowski, M., Offenberg, J. H., Jaoui, M., and Edney, E. O.: Ozone-isoprene reaction: reexamination of the formation of secondary organic aerosol, Geophys. Res. Lett., 34, L01805, 2007.

Klimont, Z., Cofala, J., Xing, J., Wei, W., Zhang, C., and Wang, S.: Projections of SO_2, NO_x and carbonaceous aerosol emissions in Asia, Tellus B, 61, 602–617, 2009.

Klimont, Z., Streets, D.G., Gupta, S., Cofala, J., Fu, L., Ichikawa, Y., 2002. Anthropogenic emissions of non-methane volatile organic compounds in China. Atmos. Environ. 36 (8), 1309e1322.

Kota, S.H., Guo, H., Myllyvirta, L., Hu, J., Sahu, S., Garaga, R., Ying, Q., Gao, A., Dahiya, S., Wang, Y., and Zhang, H., 2018. Year-long simulation of gaseous and particulate air pollutants in India, Atmospheric Environment, 180, 244-255.

Kumar, R., Naja, M., Venkataramani, M., and Wild, S.: Variations in surface ozone at Nainital: A high-altitude site in the central Himalayas, J. Geophys. Res., 115, D16302, 2010.

Kumar, R., Naja, M., Pfister, G. G., Barth, M. C., Wiedinmyer, C., and Brasseur, G. P.: Simulations over South Asia using the weather research and forecasting model with chemistry (WRF-Chem): Chemistry evaluation and initial results, Geosci. Model Dev., 5, 619–648, 2012.

Lam, N. L., Muhwezi, G., Isabirye, F., Harrison, K., Ruiz-Mercado, I., Amukoye, E., Mokaya, T., Wambua, M., and Bates, N.: Exposure reductions associated with introduction of solar lamps to kerosene lamp-using households in Busia County, Kenya, Indoor Air, 28, 218–227, 2018.

Lei, Y., Zhang, Q., He, K. B., and Streets, D. G.: Primary anthropogenic emission trends for China, Atmos. Chem. Phys., 11, 931–954, 2011.

Lelieveld, J., Evans, J. S., Fnais, M., Giannadaki, D., and Pozzer, A.: The contribution of outdoor air pollution sources to premature mortality on a global scale, Nature, 525, 367–371, 2015.

Marais, E. A., Jacob, D. J., Jimenez, J. L., Campuzano-Jost, P., Day, D. A., Hu, W., Krechmer, J., Zhu, L., Kim, P. S., Miller, C. C., Fisher, J. A., Travis, K., Yu, K., Hanisco, T. F., Wolfe, G. M., Arkinson, H. L., Pye, H. O. T., Froyd, K. D., Liao, J., and McNeill, V. F.: Aqueous-phase mechanism for secondary organic aerosol formation from isoprene: application to the southeast United States and co-benefit of SO_2 emission controls, Atmos. Chem. Phys., 16, 1603–1618, 2016.

Ministry of Environment and Forest, Government of India, Central Pollution Control Board, Continuous Ambient Air Quality Monitoring, http://www.cpcb.gov.in/CAAQM/frmUserAvgReportCriteria.aspx.

MoPNG, 2002. Auto Fuel Policy of India. Ministry of Petroleum & Natural Gas, Government of India, New Delhi.

MoPNG, 2010. Indian Petroleum and Natural Gas Statistics, 2009e10. Ministry of Petroleum & Natural Gas, Government of India, New Delhi. MoRTH, 2011. Road Transport Yearbook (2009e10 & 2010e11). Ministry of Road Transport and Highways, Government of India, New Delhi.

Mukhopadhyay, R., Sambandam, S., Pillarisetti, A., Jack, D., Mukhopadhyay, K., Balakrishnan, K., Vaswani, M., Bates, M. N., Kinney, P. L., Arora, N., and Smith, K. R.: Cooking practices, air quality, and the acceptability of advanced cookstoves in Haryana, India: An exploratory study to inform large-scale interventions, Glob. Health Action, 5, 1–13, 2012.

Murphy, B. N., Woody, M. C., Jimenez, J. L., Carlton, A. M. G., Hayes, P. L., Liu, S., Ng, N. L., Russell, L. M., Setyan, A., Xu, L., Young, J., Zaveri, R. A., Zhang, Q., and Pye, H. O. T.: Semivolatile POA and parameterized total combustion SOA in CMAQ v5.2: impacts on source strength and partitioning, Atmos. Chem. Phys., 17, 11107–11133, 2017.

Ng, N. L., Kroll, J. H., Chan, A. W. H., Chhabra, P. S., Flagan, R. C., and Seinfeld, J. H.: Secondary organic aerosol formation from m-xylene, toluene, and benzene, Atmos. Chem. Phys., 7, 3909–3922, 2007.

Otte, T. L. and Pleim, J. E.: The Meteorology-Chemistry Interface Processor (MCIP) for the CMAQ modeling system: updates through MCIPv3.4.1, Geosci. Model Dev., 3, 243-256, https://doi.org/10.5194/gmd-3-243-2010, 2010.

Pan, X., Chin, M., Gautam, R., Bian, H., Kim, D., Colarco, P. R., Diehl, T. L., Takemura, T., Possoli, L., Tsigaridis, K., Bauer, S., and Bellouin, N.: A multi-model evaluation of aerosols over South Asia: common problems and possible causes, Atmos. Chem. Phys., 15, 5903–5928, 2015.

Pandey, A., Sadavarte, P., Rao, A. B., and Venkataraman, C.: Trends in multi-pollutant emissions from a technology-linked inventory for India: II. Residential, agricultural and informal industry sectors, Atmos. Environ., 99, 341–352, 2014.

Pant, P. and Harrison, R. M.: Critical review of receptor modelling for particulate matter: A case study of India, Atmos. Environ., 49, 1–12, 2012.

Pillarisetti, A., Vaswani, M., Jack, D., Balakrishnan, K., Bates, M. N., Arora, N. K., and Smith, K. R.: Patterns of stove usage after introduction of an advanced cookstove: The long-term application of household sensors, Environ. Sci. Technol., 48, 14525–14533, 2014.

Presto, A. A., Miracolo, M. A., Donahue, N. M., and Robinson, A. L.: Secondary organic aerosol formation from high-NO_x photooxidation of low volatility precursors: n-Alkanes, Environ. Sci. Technol., 44, 2029–2034, 2010.

Pye, H. O. T. and Pouliot, G. A.: Modeling the role of alkanes, polycyclic aromatic hydrocarbons, and their oligomers in secondary organic aerosol formation, Environ. Sci. Technol., 46, 6041–6047, 2012.

Pye, H. O. T., Luecken, D. J., Xu, L., Boyd, C. M., Ng, N. L., Baker, K. R., Ayres, B. R., Bash, J. O., Baumann, K., Carter, W. P. L., Edgerton, E., Fry, J. L., Hutzell, W. T., Schwede, D. B., and Shepson, P. B.: Modeling the current and future roles of particulate organic nitrates in the southeastern United States, Environ. Sci. Technol., 49, 14195–14203, 2015.

Reddy, M. S. and Venkataraman, C.: Inventory of aerosol and sulphur dioxide emissions from India: I-Fossil fuel combustion, Atmos. Environ., 36, 677–697, 2002.

Reddy, B .S. K., Kumar, K. R., Balakrishnaiah, G., Gopal, K. R., Reddy, R. R., Sivakumar, V., Lingaswamy, A. P., Arafath, S. M., Umadevi, K., Kumari, S. P., Ahammed, Y. N., and Lal, S.: Analysis of diurnal and seasonal behavior of surface ozone and its precursors (NOx) at a semi-arid rural site in southern India, Aerosol Air Qual. Res., 12, 1081–1094, 2012.

Rehman, I., Ahmed, T., Praveen, P., Kar, A., and Ramanathan, V.: Black carbon emissions from biomass and fossil fuels in rural India, Atmos. Chem. Phys., 11, 7289–7299, 2011.

Roden, C. A., Bond, T. C., Conway, S., Osorto Pinel, A. B., MacCarty, N., and Still, D.: Laboratory and field investigations of particulate and carbon monoxide emissions from traditional and improved cookstoves, Atmos. Environ., 43, 1170–1181, 2009.

Schnell, J. L., Naik, V., Horowitz, L. W., Paulot, F., Mao, J., Ginoux, P., Zhao, M., and Ram, K.: Exploring the relationship between surface $PM_{2.5}$ and meteorology in Northern India, Atmos. Chem. Phys., 18, 10157–10175, 2018.

Sen, A., Abdelmaksoud, A. S., Ahammed, Y. N., Alghamdi, M. A., Banerjee, T., Bhat, M. A., Chatterjee, A., Choudhuri, A. K., Das, T., Dhir, A., Dhyani, P. P., Gadi, R., Ghosh, S., Kumar, K., Khan, A. H., Khoder, M., Kumari, K. M., Kuniyal, J. C., Kumar, M., Lakhani, A., Mahapatra, P. S., Naja, M., Pal, D., Pal, S., Rafiq, M., Romshoo, S. A., Rashid, I., Saikia, P., Shenoy, D. M., Sridhar, V., Verma, N., Vyas, B. M., Saxena, M., Sharma, A., Sharma, S. K., and Mandal, T. K.: Variations in particulate matter over the Indo-Gangetic Plain and Indo-Himalayan Range during four field campaigns in winter monsoon and summer monsoon: Role of pollution pathways, Atmos. Environ., 154, 200–224, 2017.

Sharma, S. and Khare, M.: Simulating ozone concentrations using precursor emission inventories in Delhi National Capital Region of India, Atmos. Environ., 151, 117–132, 2017.

Sharma, S., Goel, A., Gupta, D., Kumar, A., Mishra, A., Kundu, S., Chatani, S., and Klimont, Z.: Emission inventory of non-methane volatile organic compounds from anthropogenic sources in India, Atmos. Environ., 102, 209–219, 2015.

Sharma, S., Chatani, S., Mahtta, R., Goel, A., and Kumar, A.: Sensitivity analysis of ground level ozone in India using WRF-CMAQ models, Atmos. Environ., 131, 29–40, 2016.

Sharma, S., Bawase, M. A., Ghosh, P., Saraf, M. R., Goel, A., Suresh, R., Datta, A., Jhajhjra, A. S., Kundu, S., Sharma, V. P., Kishan, J., Mane, S. P., Reve, S. D., Markad, A. N., Vijayan, V., Jadhav, D. S., and Shaikh, A. R.: Source apportionment of $PM_{2.5}$ and PM_{10} of Delhi NCR for identification of major sources, The Energy Resources Institute, Delhi and Automative Research Association of India, 2018.

Shen, G., Hays, M. D., Smith, K. R., Williams, C., Faircloth, J. W., and Jetter, J. J.: Evaluating the performance of household liquified petroleum gas cookstoves, Environ. Sci. Technol., 52, 904–915, 2018.

Silva, R. A., Adelman, Z., Fry, M. M., and West, J. J.: The impact of individual anthropogenic emissions sectors on the global burden of human mortality due to ambient air pollution, Environ. Health Persp., 124, 1776–1784, 2016.

Skamarock, W. C., Klemp, J. B., Dudhia, J., Gill, D. O., Barker, D. M., Duda, M. G., Huang, X. Y., Wang, W., and Powers, J. G.: A description of the advanced research WRF Version 3, NCAR Technical Note, NCAR/TN-475+STR, 2008.

Smith, K. R., Aggarwal, A. L., and Dave, R. M.: Air pollution and rural biomass fuels in developing countries – A pilot study in India and implications for research and policy, Atmos. Environ., 17, 2343–2362, 1983.

Smith, K. R., Uma, R., Kishore, V. V. N., Zhang, J., Joshi, V., Khalil, M. A. K.: Greenhouse implications of household stoves: An analysis for India, Ann. Rev. Energy Environ., 25, 741–763, 2000.

Smith, K. R., Bruce, N., Balakrishnan, K., Adair-Rohani, H., Balmes, J., Chafe, Z., Dherani, M., Hosgood, H. D., Mehta, S., Pope, D., and Rehfuess, E.: Millions dead: How do we know and what does it mean? Methods used in the comparative risk assessment of household air pollution, Annu. Rev. Publ. Health, 35, 185–206, 2014.

TERI, 2002. Pricing and Infrastructure Costing, for Supply and Distribution of CNG and ULSD to the Transport Sector, Mumbai, India (Supported by Asian Development Bank). The Energy and Resources Institute, New Delhi.

US EPA Office of Research and Development, CMAQ (Version 5.2). Zenodo. http://doi.org/10.5281/zenodo.1167892, 2017 (June 30).

World Health Organization: Household air pollution and health, http://www.who.int/en/news-room/fact-sheets/detail/household-air-pollution-and-health, 2018.

Yarwood, G., Jung, J., Whitten, G. Z., Heo, G., Melberg, J., and Estes, M.: CB6: Version 6 of the Carbon Bond Mechanism, 2010 CMAS Conference, Chapel Hill, NC, 2010.

Zhong, M., Saikawa, E., Liu, Y., Naik, V., Horowitz, L. W., Takigawa, M., Zhao, Y., Lin, N. H., and Stone, E. A.: Air quality modeling with WRF-Chem v3.5 in East Asia: sensitivity to emissions and evaluation of simulated air quality, Geosci. Model Dev., 9, 1201–1218, 2016.

Chapter 3

CLIMATE AND HEALTH CO-BENEFITS FROM HOUSEHOLD SOLID FUEL USE IN HARYANA, INDIA

3.1 Introduction

Cleaner cookstoves can have direct health benefits through reductions in pollutant exposures in homes, through reduced downstream ambient pollution (by preventing formation of secondary air pollutants including ozone and secondary organic aerosol), and through reductions in emissions affecting climate, including black carbon and short-lived climate forcing compounds[1, 2]. Recent chemical characterization of fuel-specific particulate matter emissions[1], and emissions of 76 volatile organic compounds (VOCs)[2] from minimally directed cooking tests in India demonstrated that use of dung patties leads to approximately three times more secondary organic aerosol and ozone formation compared to wood. These studies also found that stove type significantly influenced VOCs, such as benzene and previously unidentified nitrogen-containing organic compounds, in the particulate emissions. Because emissions of particulate and volatile species are dependent on combustion conditions, these data demonstrate the need to evaluate whether combustion conditions during either in-home or laboratory testing are representative of typical household cooking activities. They additionally highlight the need for methods that allow collection of household emissions measurements that are representative of combustion conditions during typical household cooking activities[3].

Evaluating the climate and health benefits of cookstoves can help prioritize policies that maximize co-benefits for near-term climate, human health, agriculture, and the cryosphere[4]. In addition, climate finance, based on emission reduction credits, provides a mechanism to reduce up-front installation costs for clean cooking solutions, allowing them to be

competitive with cost-effective health interventions[5, 6]. While a number of studies have estimated climate and health implications of cookstoves[7-10], they have been hampered by a lack of emissions data from stoves during normal usage. Furthermore, few detailed co-benefit analyses have been based on actual measurements of stove performance in-field[11]. A growing body of evidence has demonstrated substantial differences between laboratory testing and in-field observations[12-17]. There are therefore significant concerns whether climate and health co-benefits estimated from controlled emissions testing represent the reality in homes.

In this paper, we compare uncontrolled, in-home measurements of fuel consumption and emission factors of carbon dioxide (CO_2), carbon monoxide (CO), elemental carbon (EC), organic carbon (OC), and $PM_{2.5}$ during daily cooking events in three villages in Haryana, India, with minimally directed cooking tests in an adjacent village kitchen and also separately to previous laboratory and fuel-based measurements of emissions in India. We also evaluate the climate impact of total emissions from these same stoves including secondary pollutants. A non-traditional cookstove, the Philips HD4012 fan stove, was also evaluated during uncontrolled, in-home cooking to compare to previous laboratory measurements. The results demonstrate that minimally directed cooking tests, by performing similar cooking tasks using local fuels and fuel mixtures, generate representative emissions and estimates of climate and health   co-benefits   in   these   communities.

3.2 Methods

Sample Selection. For the uncontrolled testing, village homes were identified within the SOMAARTH demographic site in Manpur, Gehlab, Banchari and Mitrol[18, 19]. Sampling occurred during both morning and evening cooking periods. Cookstoves included chulhas (traditional Indian mud cookstoves used for cooking), angithis/haros (two names for similar traditional Indian mud cookstoves, used primarily to cook animal feed, differing only in that haros are fixed in place while angithis are portable), and the Philips HD4012 fan stoves (a modern, fan-driven, top-loading partial-gasifier stove). Fuel was not provided and homes were selected as a convenience sample in the village.

Minimally Directed Cooking Tasks. A local cook was hired and instructed to prepare a meal with either rice or chapatti (an Indian flatbread) as starch, vegetables, and dahl based on market availability of ingredients for 4 people. Each meal was prepared by the same local cook who determined fuel loading and fire-tending from a load of fuel preselected for fuel type (dung or brushwood or both mixed together) and moisture content (wet or dry). When fuels were mixed, the ratio of dung to wood was chosen by the cook. The cook was also instructed to cook typical village meals rather than specialty meals. No other instructions regarding cooking were given to the cook in order to maximize the cook's ability to cook in their typical fashion. The minimally directed testing was also done in SOMAARTH and was conducted in an outdoor kitchen in the village of Khatela, Palwal, Haryana, India (supporting information figure S1). Palwal District has ~170000 homes in which 39% use wood as their primary cooking fuel, followed by dung (25%), and crop residues (7%)[20]. In SOMAARTH, the percent of households using biomass and agricultural residue as their primary fuel for cooking has been estimated at 96.6%[21].

Fuel Assessment. For both the minimally directed and uncontrolled cooking tests, the total mass of each fuel type utilized was calculated by weighing the total fuel of each type before and after each cooking event using a postal scale (Model PE10, Pelouze, China). Fuel moisture was assessed using a 9-volt digital moisture meter for both wood and dung patties (Model: 50270, SONIN Inc., China). Moisture measurements for dung patties were adjusted in accordance with Gautam et al. 2016[22]. For the uncontrolled in-home testing fuel selection, meal-type, fuel loading, and fire-tending were determined by the individual cooks (n=5). Two homes were measured twice during uncontrolled testing for a total of 7 meals.

Sampling and Analysis. For all testing emissions were sampled and analyzed for CO_2, CO, and $PM_{2.5}$ using established methods[23]. In brief, three-pronged metal probes were hung above each stove and emissions sampled using PCXR8 pumps (SKC Inc. Universal, Pennsylvania, USA). Simultaneous measurements were conducted in the kitchen yard for determination of background concentrations for subtraction during analysis. Flows were evaluated via a Mesalabs Defender 530 (BGI Mesa Labs, Lakewood, CO) during the in-

home testing and a TSI 4140 flowmeter (TSI, Shoreview, MN) during controlled testing before and after each cooking event. Pumps were turned on before cooking began so that entire cooking events were captured and turned off when cooking was completed. Johnson et al. reported less than a 1% difference between modified combustion efficiency (MCE, the ratio of emitted moles of CO_2 to CO_2 and CO) between sampling hoods and the three-pronged probes used in this study[23]. Similarly, Zhang et al. also reported no significant changes in emission ratios between flue gas and hood samples[24]. Concentrations of CO_2 and CO were analyzed for all samples using a TSI Q-Trak 7575 (TSI, Shoreview, MN), and adjusted for background ambient concentrations[25].

Size selection of aerosols to collect $PM_{2.5}$, EC, and OC was achieved using a SCC 1.062 (Triplex) personal sampling cyclone (Triplex, BGI Incorporated, Waltham, MA). Polytetrafluoroethylene (PTFE) filters (PTFE Filter with PMP support ring, 2.0 µm, 47 mm, SKC Inc., Fullerton, CA) were pre and post-weighed on a Cahn-28 electrobalance with a repeatability of ± 1.0 µg after equilibrating for a minimum of 24 hours in a humidity and temperature-controlled environment. Five field blanks were collected, by opening filters in the field site and resealing, which had an average mass difference of 0.4 ± 3.1 µg, equivalent to less than 0.1% of average mass deposition of emissions samples and 0.2% of background samples. All sample filters, background and emissions, had a minimum of 109 µg collected material, above the limit detection for the method calculated at 9.3 µg or three-times the standard deviation of the measurement of the field blanks. Quartz filters were collected and analyzed for EC and OC with a Sunset Laboratory OC/EC analyzer using established methods[26].

Emission factors (EFs) for gases and $PM_{2.5}$ were determined using the carbon-balance method[27]. In brief, ERs and EFs were determined by multiplying the carbon fraction of each pollutant emissions by the total emitted carbon during the burn. The carbon content of the fuel was taken to be 33.4% for buffalo dung and 45.4% for brushwood fuels based on Smith et al[27]. Carbon in ash was estimated as 2.9% and 80.9% of the mass of char for dung and brushwood, respectively[27].

Climate impacts were estimated using 100-Year global warming commitments potentials (GWP$_{100}$, see supporting information table S1) as tCO$_2$e per kilogram dry fuel incorporating the fraction of non-renewable harvesting of fuels[28]. Species included in estimating climate impacts were CO$_2$, CO, EC, and OC emission factors. In order to convert PM$_{2.5}$ emission factors from water boiling tests (WBTs)[27] into EC and OC, EFs assumptions on the relationships between organic matter, organic carbon, elemental carbon and PM$_{2.5}$ were utilized in a similar manner to Grieshop et al.[10]. Elemental carbon was estimated as 21% of PM$_{2.5}$ mass, organic matter estimated as the remaining 79%, and organic carbon estimated as organic matter divided by 1.9 based on the values suggested for fireplace combustion of pine or oak in Roden and Bond[29]. The fraction of the fuel that is from non-renewable biomass was assumed to be zero for dung and taken as 19% for wood based on a reported value for Haryana[28]. GWC$_{100}$ estimations are also limited by assumptions made on GWP$_{100}$ values and the fraction of the fuel that is from non-renewable biomass. By assuming that organic matter is 1.9 times organic carbon we may either over or underestimate the contribution of organic carbon to GWP$_{100}$, as this relationship has been shown to vary between ~1 and 3 depending on the source and age of the aerosol[29]. In order to account for the effects of secondary organic aerosols on climate impacts, total PM$_{2.5}$ SOA was calculated from primary PM$_{2.5}$ emissions. Based on previous modeling work, 1.64 grams of organic carbon SOA was added when calculating GWP for each gram of primary PM$_{2.5}$[30]. Additional information on equations used for climate impacts can be found in the supporting information with GWP values in SI table S1.

Statistical analysis was performed with R version 3.3.1 and figures produced in either Microsoft Excel 2010 or R version 3.3.1.

3.3 Results

Table 1 lists the geometric mean EFs for PM$_{2.5}$, EC, and OC in grams per kilogram dry fuel and fuel consumption rates for the uncontrolled in-home and minimally directed tests of mixed-fuel use in the chulha. Results for mixed fuels are presented since this was the typical

practice in village homes, although use of mixed fuels complicates comparisons with controlled testing, as the majority of results from WBT tests typically use only one fuel type. Overall $PM_{2.5}$ emission rates from minimally directed cooking were on the upper end of the range of uncontrolled emission factors, but no statistically significant differences ($p<0.05$) were observed for particulate EFs ($PM_{2.5}$, organic or elemental carbon) or fuel consumption rates between the uncontrolled and minimally directed testing.

While CO_2 emission factors in g/kg dry fuel were significantly higher in uncontrolled testing compared to minimally directed cooking tests($p<0.01$), they were not significantly different on a carbon basis (g /kg Carbon; see SI table S2), due in part to differences in the ratio of dung: wood in the mixed fuels. Because wood and dung have different carbon contents as a percent of dry weight, as the ratio of dung: wood changes, the total carbon per kilogram of dry fuel is also altered. Thus, relatively minor compositional changes in the ratio of dung: wood lead to differences in g/kg dry fuel not observed when analyzing on a per kilogram of carbon basis. Fuel consumption was also more highly variable in uncontrolled testing likely due to household size and specific cooking demands, which may also partially explain why the standard deviations for PM, EC, and OC emissions factors and fuel consumption were higher in uncontrolled testing.

Table 1: Geometric mean MCEs and EF consumption rates for the uncontrolled in-home and controlled tests of mixed-fuel use in the chulha alongside differences in the arithmetic

	Uncontrolled (n=7)	Minimally directed (n=13)	Difference in Mean	P(T<=t) Two-Tail
MCE	89.2% (1.1%)	86.4% (2.5%)	2.80%	**<0.01**
$PM_{2.5}$ EF g/kg Dry Fuel	8.7 (7.6)	12.3 (2.5)[‡]	-1.6	0.61
EC EF g/kg Dry Fuel	0.4 (0.5)[‡]	0.6 (0.2)	-0.1	0.69
OC EF g/kg Dry Fuel	3.9 (5.7)[‡]	5.6 (0.9)	0.3	0.91
Dry Fuel g/min	23.5 (9.6)	25.8 (2.3)	-2	0.54

mean values and P values from Welch's two-sided t tests. Values for the uncontrolled and marginally-directed tests are listed as geometric mean (standard deviation). [‡]: Sample size reduced by one due to a damaged filter

Differences between in-home measurements and WBT. Table 3.2 and figure 3.1 show a comparison between geometric mean EFs for total suspended particles (TSP) from select WBTs of traditional cookstoves for various fuel types (Smith, et al., 2000) and minimally directed in-home field tests for $PM_{2.5}$. Differences observed between partially controlled testing and WBT are thus slightly conservative because TSP includes both $PM_{2.5}$ and particles with larger aerodynamic diameters. Previous measurements of mass fractions for burning of biomass in traditional stoves showed emission factors for TSP 17% higher than $PM_{2.5}$ for firewood and 20% higher for dung cakes[31].

Fuel/Stove Type	Cow Dung in Chulha		Wood in Chulha		All Chulha Tests		Cow Dung in Haro	
	n	Geomean	n	Geomean	n	Geomean	n	Geomean
India measurements from Smith et al. 2000 (g TSP/kg dry fuel)	3	2.2	3	0.6	6	1.2	3	0.5
Minimally directed in Haryana (g $PM_{2.5}$/kg dry fuel)	15	18.2	14	6.3	41	10.8	10	32.3
Approximate Factor Difference	9		9		9		65	

Table 3.2: Factor differences between water boiling tests and in-home field testing of particulate emission factors. Geometric mean EFs for TSP by both stove and fuel type for both WBTs and minimally directed tests alongside factor differences. The "All Chulha" category includes the cow dung, wood, and mixed-fuel tests. These EFs were generated based on WBTs of traditional Chulha cookstoves[27].
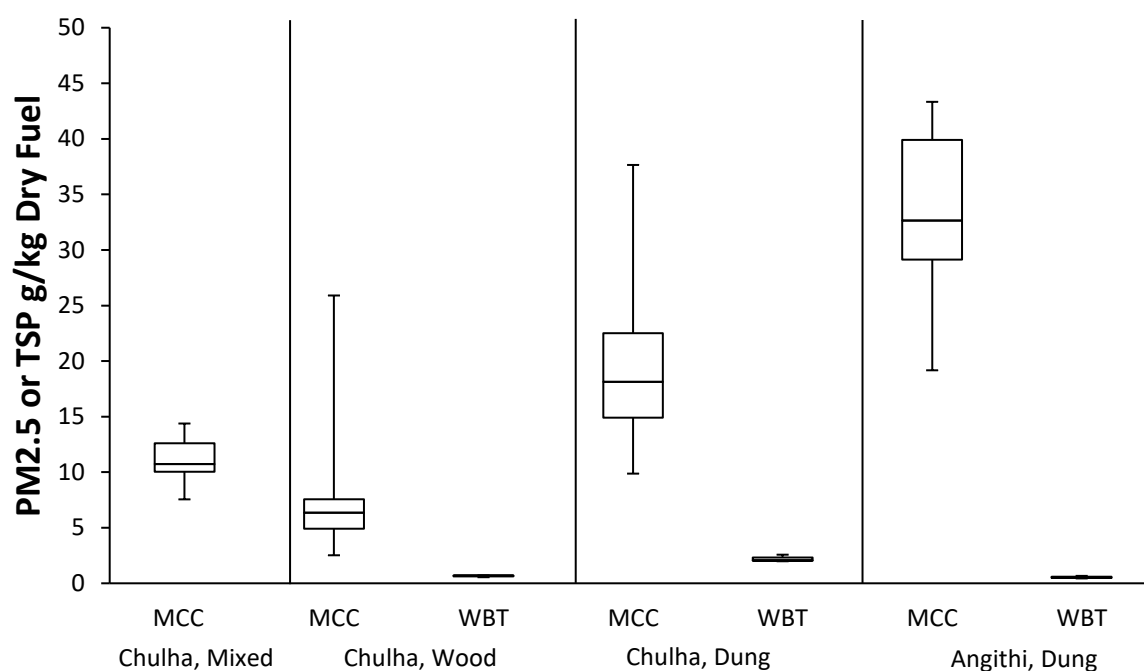
Figure 3.1: Particulate emission factors for both in-home minimally directed cooking tests (labeled as MCC) and water boiling tests (labeled as WBT). Data for this figure are presented in Table 2. There were 12 mixed-fuel Chulha MCC tests.

TSP emission factors per kilogram of dry fuel derived from the WBT were a factor ~9 lower than the chulha across all fuel combinations when compared with minimally directed cooking. Use of mixed fuels or wood resulted in significantly lower PM emissions compared to use of solely dung. Pandey et al. also show an underestimation of PM emission factors by WBT compared to prescribed cooking tests in a rural Indian home by a factor of 2-8[15]. Similarly, both Johnson et al. and Roden et al. reported a factor of 2-4 difference in particulate matter emissions between laboratory WBTs and field experiments for traditional stoves[14, 16]. Although factor differences were larger when comparing the Smith inventory and the current minimally directed cooking study, both Johnson et al. and Roden et al. report emission factors of >2 g $PM_{2.5}$/kg dry fuel for WBTs, which would result in a factor of ~2-3 difference when comparing to the minimally directed cooking. The range of factors observed, suggests that predicting field emissions based on laboratory tests in unlikely to lead to reliable estimates.

 Average reported field EFs for Rajasthan fuel wood and Bihar dung were 10.5 (95% confidence interval 7.7-13.4) and 22.6 (14.9-32.9) g kg^{-1} for the burn cycles, however wood from Punjab had PM EFs ranging from 3-15 g kg^{-1} (depending on combustion phase) and dung from Uttar Pradesh had PM EFs ranging from 5-28 g kg^{-1} [15]. The low number of samples for each location (n≤4) precluded detecting any statistical differences between fuel wood types[15]. Emissions from the angithi/haro, which is typically used for slow simmering of milk or animal fodder using smoldering dung patties, were 65 times higher in uncontrolled testing compared to WBTs, which may indicate that the test protocol used to perform a WBT created highly uncharacteristic combustion conditions.

Table 3.3 shows a comparison of emissions from the wood-burning Philips stoves in the laboratory and from uncontrolled in-field testing. Emissions of PM$_{2.5}$ per kg dry fuel for the Philips stoves in the current study were substantially higher than those measured during laboratory tests of both wet and dry wood by Jetter et al.[32]. Laboratory-based testing of cookstoves utilizing the WBT employed three separate phases of testing; a cold start, a hot start and a simmering phase (Water Boiling Test version 4.2.3). Emissions of PM$_{2.5}$ per kg dry fuel were substantially higher in the current tests compared to the laboratory by factors of 2.4-9.0. Uncontrolled cooking tests and the wet wood WBTs had similar mean moisture contents (22.7% in the uncontrolled cooking versus 22.1 to 23% in the WBTs) although the variability in uncontrolled in-home testing was much larger as the standard error was 25.6% of the mean for uncontrolled cooking versus 3.1 to 12.3% for WBTs). ER and EF differences between uncontrolled cooking and laboratory testing were smallest for comparisons of the cold-start with wet wood (factors of 0.8-2.4), although significant differences in MCE were observed across all three phases of laboratory testing when comparing to the uncontrolled cooking via Welch's two-sided t tests (p<0.05, shown in supporting figure S2).

Philips Stove	n	MCE	PM$_{2.5}$ EF	PM$_{2.5}$ ER	CO EF	CO ER
Uncontrolled Cooking (current study)	7	0.95	3.2	22.3	42.9	0.3
WBT Simmer[20]	3	0.99/0.98	0.5/0.5	2.8/3.3	10.8/21.3	0.1/0.1
Factor differences for Simmering			6.6/6.4	7.9/6.7	4.0/2.0	4.5/2.0
p-Values		0.015/0.033	0.019/0.019	0.031/0.034	0.024/0.081	0.008/0.038
WBT Cold Start[20]	3	0.99/0.98	0.5/1.4	7.3/19.3	10.4/25.8	0.2/0.4
Factor differences for Cold Start			6.9/2.4	3.0/1.2	4.1/1.7	1.7/0.8
p-Values		0.014/0.049	0.018/0.103	0.074/0.790	0.019/0.186	0.069/0.474
WBT Hot Start[20]	3	1.00/0.99	0.4/0.6	6.0/10.5	2.4/11.0	0.0/0.2
Factor differences for Hot Start			9.0/5.2	3.7/2.1	17.9/3.9	6.7/1.5
p-Values		0.007/0.013	0.016/0.027	0.057/0.243	0.007/0.021	0.004/0.134

Table 3.3: Comparison of average emissions from the Philips stove in laboratory[32] and uncontrolled testing. Laboratory testing is listed as average values for triplicate (or more) measurements of dry wood/wet wood, with the wet wood value as the second entry. EFs are listed as averages in g/kg dry fuel and ERs are listed as averages in g/minute for CO and mg/min for PM.

Comparison to Laboratory Fuel-Burning. PM$_{2.5}$ emission factors from in-laboratory burning of fuel in non-cooking settings by Saud et al. determined using a modified dilution sampler for dung cake and fuel-wood collected from Delhi, Uttar Pradesh, Punjab, Haryana, Uttarakhand and Bihar of 16.3 ± 2.3 g kg^{-1} and 4.3 ± 1.1 g kg^{-1} for dung and fuel-wood, respectively[33] were similar to uncontrolled field measurements in Haryana using the same fuels (18.2 ± 7.1 and 6.3 ± 5.7 g kg^{-1} for dung and fuel-wood respectively) for the chulha, but were not reflective of the mixed fuel use typical of homes in the region, and of emissions from Phillips and angithi stoves showing that fuel tests need to reflect the way in which the fuel is burned in real stoves.

3.4 Discussion

Although laboratory testing serves a critical function in evaluating stove design, the use of the results to draw wide conclusions about environmental and health co-benefits of cookstoves can provide misleading information of the relative benefits, as they do not reflect emissions from regular use in real homes. Minimally directed cooking tests in our study villages resulted in emissions that were more reflective of actual usage in real homes than

laboratory testing. Emission factors from minimally directed cooking were close to those from uncontrolled tests in these villages and overlapping with those measured by Johnson et al. (2019)[17]. Previous research has mostly indicated that emission factors for non-CO_2 species increase relative to CO_2 in cookstoves when fuel moisture is increased as a result of increased products of incomplete combustion[34, 35], although this effect is not universally true for all stove testing[29, 36]. Selection of high and low moisture dung patties and/or wood for minimally directed cooking tests, however, did not lead to significant difference in emissions rates although verbal complaints about high moisture patties and compensatory behavior was expressed by the cook during cooking. Matching the moisture content of fuels for testing minimally directed cooking tasks to those used on a regular basis for that cooking task would likely generate emissions estimates that more closely match those from uncontrolled cooking, and shows promise for testing approaches that would provide more realistic estimates of climate and health co-benefits.

While the minimally directed cooking tests in these villages in Haryana show promise in producing more representative emissions, there are a number of limitations. The sample size was limited in our study, villages and a larger number of samples from a wider set of locations would be required for wider applicability, both in India and further afield. In real homes, stove types, usage, and stove maintenance vary. Each of these parameters has significant impacts on combustion conditions, which in turn will change emissions. Use of minimally directed cooking tasks does not inherently capture the wide range of stove types, maintenance, chimney heights, draft characteristics, and variations in operation and tending seen in homes. Further, consideration should also be made for the range of fuels used during different seasonal periods of the year, and the degree of stove-stacking present in homes. Given the widespread presence of stove and fuel stacking in different parts of the world, estimating environmental and health implications of cookstoves by simply comparing results from water boiling tests from one stove to another assuming total replacement will lead to misplaced expectations for stove programs. In addition, incorporating stove stacking into current international emission guidelines for stoves, emission inventories and climate and health co-benefit estimates is a priority. Use of minimally directed cooking tests allows for

multiple stoves to be used according to user preferences, and may generate more representative measurements of emissions in homes.

Geometric mean fuel consumption rates for the Philips stove during uncontrolled tests in these 3 villages in Haryana utilizing only wood were 6.9 ± 1.4 g/min, which were closer to those seen in the simmering phase of the water boiling test, and were considerably lower than those seen in the cold start and hot start (5.7/6.4 for the simmering using dry/wet wood, 15.5/14.0 for the cold start and 17.5/16.8 g/min for the hot start phase, respectively) [32]. Thus, similar to cooking in Michoacan Mexico[13], the majority of cooking involved low-power tasks, and high-power tasks represent a small fraction of total stove usage. For the Phillips in this study, a burn cycle for dry wood where approximately 11% of the fuel was consumed in the cold-start phase and 89% in the simmering phase would achieve equivalent fuel-consumption rates to that seen during uncontrolled cooking, suggesting that task-based emission factors can provide more representative, realistic expectations of climate and health co-benefits for programs that provide alternative stoves.

Climate and health co-benefits. Figure 3.2 shows climate warming potentials and particulate EFs for chulha stoves (data labeled "Chulha") in minimally directed cooking tests (data labeled "MCC") and uncontrolled tests (data labeled "U") in village kitchens using wood, mixed fuels, and dung. Minimally directed cooking results for the angithi stove burning dung (labeled "MCC Angithi Dung") were also included as well as literature values for in-home emissions of 22 traditional Indian chulhas (labeled "Johnson et al. 2019"), utilizing wood as their primary fuel[17]. In order to account for the effects of secondary organic aerosol (SOA) on both climate and health co-benefits, SOA was calculated as a function of primary $PM_{2.5}$ emissions. SOA mass was assumed to be 164% of the primary $PM_{2.5}$ emissions' mass, based on previous secondary organic $PM_{2.5}$ mass concentrations predicted by CMAQ simulations for September 2015 at SOMAARTH headquarters[30]. SOA mass was assumed to be OC for estimating climate benefits. A negative correlation between $PM_{2.5}$ emission factors and GWC_{100} ($R^2 = 0.99$) implies cookstoves are climate neutral for emissions at 9.8 grams of primary $PM_{2.5}$ per kilogram of dry fuel (26 g/kg of $PM_{2.5}$ including SOA).

Similarly, for GWC_{20}, cookstoves would be climate neutral at 8.8 grams of primary $PM_{2.5}$ per kilogram of dry fuel (23 g/kg of $PM_{2.5}$ including SOA). In field emissions factors of traditional unvented biomass stoves from inventories average around 7.4 g/kg dry fuel, with a typical range of 5 to 12 g/kg dry fuel[37], implying that these stoves may be slightly warming or cooling with values close to neutral at both 20 and 100-year time horizons. Improvements in combustion efficiency through transition to cleaner burning cookstoves will tend to increase warming commitments from these stoves as the organic carbon emissions decrease. Estimates of warming or cooling are not sensitive to the ratio of $PM_{2.5}$ to organic carbon, as previous uncontrolled measurements have found robust linear relationships between ratios of $PM_{2.5}$:OC, with slopes of 1.29 to 1.35 for a variety of biomass stoves across 174 measurements representing a wide range of fuel types, stove types, flues, altitudes, and cooking locations[38]. Although there are issues with time horizons when using GWP to compare the effects of short-lived and long-lived atmospheric species on climate[39-41], Figures S3 and S4 show contributions of each species to the GWC_{20} and GWC_{100}, respectively, demonstrating how warming commitments from these stoves are dominated by contributions of short lived climate forcing species OC and SOA.

The fraction of non-renewable biomass harvested and secondary organic aerosol generated in the atmosphere differ between agro-climatic regions, and thus the relative impacts of stoves will vary across regions. Current estimates of the fraction of non-renewable woodfuels have large geographic variations. For example in 2009, while India had seen a net gain in afforestation in recent years, 23-24% of India's woodfuel and 29.6% of Asia and Oceania's woodfuel was harvested unsustainably[28]. Using Asia and Oceania's average fraction of non-renewable biomass of 29.6% would raise the PM intercept for climate-neutral emissions to 10.4 g/kg dry fuel for a 100-year horizon and 8.9 g/kg for a 20-year horizon. Using this cut-off, some uncontrolled field tests of biomass burning stoves in Nepal, Cambodia, and Tibet would imply a net cooling[42-45]. Assuming that SOA formation processes are similar between different regions, the difference between the 29% regional estimates of the fraction of non-renewable harvesting and the 19% for Haryana result in only a modest difference in the intercept between warming and cooling emissions. Large fractions of global emissions,

therefore, would be close to climate neutral based on these estimates. Clearly, however, in fuelwood harvesting hotspots the intercept where primary emissions are warming would be higher, which highlights that the climate implications of stoves will depend on the specific communities in which the stoves are distributed. Similarly, where households use different mixtures of fuels the intercept for climate neutral emissions will also vary from those presented here based on the specific fuel mixture present and fraction of renewable harvesting of each fuel. In spite of these limitations, these findings show that when SOA and other climate forcing particulate species are included in estimates, along with regional estimates of non-renewable harvesting, emissions from stoves using biomass fuels are likely to be much less climate warming than previously thought, and some may be climate cooling. Although beyond the scope of the current paper, this has large implications both for methods to estimate carbon offsets, and for the viability of climate offsets from solid biomass cookstoves, as improved combustion will lead to less $PM_{2.5}$ emissions primarily as a result of reduced OC. While these results cannot capture the full range of emissions, SOA formation conditions and harvesting from different agroclimatic regions, these findings highlight the importance of calculating global warming from cookstoves including a full suite of climate forcing species including SOA formed after emission into the atmosphere, and also including realistic estimates of the fraction of non-renewable harvesting of biomass.
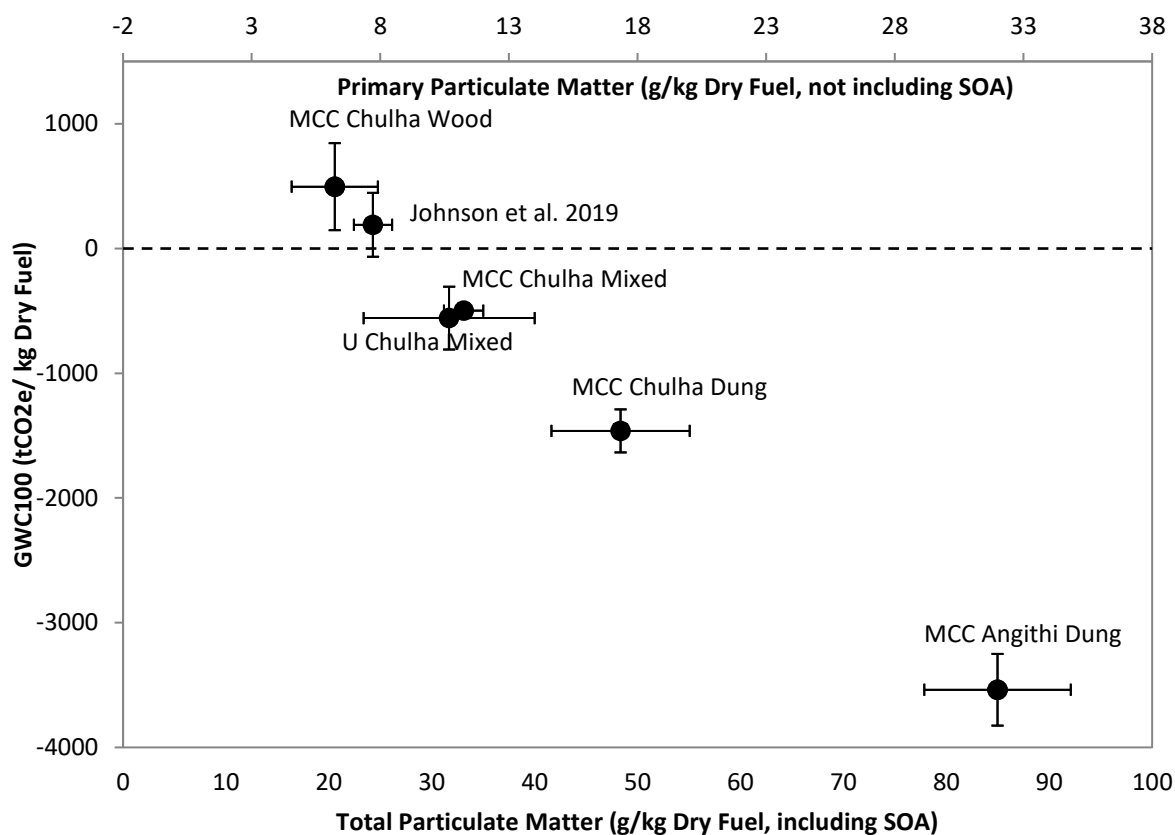
Figure 3.2: A plot of GWC100 versus particulate matter EFs for wood, dung, and mixed fuels. Error bars indicate the standard error of measurements. Particulate matter is expressed as both primary emissions only (top horizontal axis) and as total emissions including SOA mass (bottom horizontal axis).

References

1. Fleming, L. T.; Lin, P.; Laskin, A.; Laskin, J.; Weltman, R.; Edwards, R. D.; Arora, N. K.; Yadav, A.; Meinardi, S.; Blake, D. R., Molecular composition of particulate matter emissions from dung and brushwood burning household cookstoves in Haryana, India. *Atmospheric Chemistry and Physics* **2018,** *18*, (4), 2461-2480.

2. Fleming, L. T.; Weltman, R.; Yadav, A.; Edwards, R. D.; Arora, N. K.; Pillarisetti, A.; Meinardi, S.; Smith, K. R.; Blake, D. R.; Nizkorodov S.A., Emissions from village cookstoves in Haryana, India and their potential impacts on air quality. *Atmospheric Chemistry and Physics* **2018**.

3. Johnson, M.; Edwards, R.; Berrueta, V.; Masera, O., New approaches to performance testing of improved cookstoves. *Environmental science & technology* **2009,** *44*, (1), 368-374.

4. Shindell, D.; Kuylenstierna, J. C. I.; Vignati, E.; van Dingenen, R.; Amann, M.; Klimont, Z.; Anenberg, S. C.; Muller, N.; Janssens-Maenhout, G.; Raes, F.; Schwartz, J.; Faluvegi, G.; Pozzoli, L.; Kupiainen, K.; Höglund-Isaksson, L.; Emberson, L.; Streets, D.; Ramanathan, V.; Hicks, K.; Oanh, N. T. K.; Milly, G.; Williams, M.; Demkine, V.; Fowler, D., Simultaneously Mitigating Near-Term Climate Change and Improving Human Health and Food Security. *Science* **2012,** *335*, (6065), 183.

5. Freeman, O. E.; Zerriffi, H., How you count carbon matters: implications of differing cookstove carbon credit methodologies for climate and development cobenefits. *Environmental science & technology* **2014,** *48*, (24), 14112-14120.

6. Hewitt, J.; Ray, C.; Jewitt, S.; Clifford, M., Finance and the improved cookstove sector in East Africa; Barriers and opportunities for value-chain actors. *Energy Policy* **2018,** *117*, 127-135.

7. Chafe, Z. A.; Brauer, M.; Klimont, Z.; Van Dingenen, R.; Mehta, S.; Rao, S.; Riahi, K.; Dentener, F.; Smith, K. R., Household cooking with solid fuels contributes to ambient PM2. 5 air pollution and the burden of disease. *Environmental health perspectives* **2014,** *122*, (12), 1314.

8. Venkataraman, C.; Sagar, A.; Habib, G.; Lam, N.; Smith, K., The Indian national initiative for advanced biomass cookstoves: the benefits of clean combustion. *Energy for Sustainable Development* **2010,** *14*, (2), 63-72.

9. Anenberg, S. C.; Schwartz, J.; Shindell, D.; Amann, M.; Faluvegi, G.; Klimont, Z.; Janssens-Maenhout, G.; Pozzoli, L.; Van Dingenen, R.; Vignati, E., Global air quality and health co-benefits of mitigating near-term climate change through methane and black carbon emission controls. *Environmental Health Perspectives* **2012,** *120*, (6), 831.

10. Grieshop, A. P.; Marshall, J. D.; Kandlikar, M., Health and climate benefits of cookstove replacement options. *Energy Policy* **2011,** *39*, (12), 7530-7542.

11. García-Frapolli, E.; Schilmann, A.; Berrueta, V. M.; Riojas-Rodríguez, H.; Edwards, R. D.; Johnson, M.; Guevara-Sanginés, A.; Armendariz, C.; Masera, O., Beyond fuelwood savings: Valuing the economic benefits of introducing improved biomass cookstoves in the Purépecha region of Mexico. *Ecological Economics* **2010,** *69*, (12), 2598-2605.

12. Bailis, R.; Berrueta, V.; Chengappa, C.; Dutta, K.; Edwards, R.; Masera, O.; Still, D.; Smith, K. R., Performance testing for monitoring improved biomass stove interventions: experiences of the Household Energy and Health Project. *Energy for sustainable development* **2007,** *11*, (2), 57-70.

13. Berrueta, V. M.; Edwards, R. D.; Masera, O. R., Energy performance of wood-burning cookstoves in Michoacan, Mexico. *Renewable Energy* **2008,** *33*, (5), 859-870.

14. Johnson, M.; Edwards, R.; Alatorre Frenk, C.; Masera, O., In-field greenhouse gas emissions from cookstoves in rural Mexican households. *Atmospheric Environment* **2008,** *42*, (6), 1206-1222.

15. Pandey, A.; Patel, S.; Pervez, S.; Tiwari, S.; Yadama, G.; Chow, J. C.; Watson, J. G.; Biswas, P.; Chakrabarty, R. K., Aerosol emissions factors from traditional biomass cookstoves in India: insights from field measurements. *Atmospheric Chemistry Physics* **2017,** *17*, (22), 13721-13729.

16. Roden, C. A.; Bond, T. C.; Conway, S.; Pinel, A. B. O.; MacCarty, N.; Still, D., Laboratory and field investigations of particulate and carbon monoxide emissions from traditional and improved cookstoves. *Atmospheric Environment* **2009,** *43*, (6), 1170-1181.

17. Johnson, M. A.; Garland, C. R.; Jagoe, K.; Edwards, R.; Ndemere, J.; Weyant, C.; Patel, A.; Kithinji, J.; Wasirwa, E.; Nguyen, T., In-Home Emissions Performance of Cookstoves in Asia and Africa. *Atmosphere* **2019,** *10*, (5), 290.

18. Mukhopadhyay, R.; Sambandam, S.; Pillarisetti, A.; Jack, D.; Mukhopadhyay, K.; Balakrishnan, K.; Vaswani, M.; Bates, M. N.; Kinney, P.; Arora, N., Cooking practices, air

quality, and the acceptability of advanced cookstoves in Haryana, India: an exploratory study to inform large-scale interventions. *Global health action* **2012,** *5*, (1), 19016.

19. Pillarisetti, A.; Vaswani, M.; Jack, D.; Balakrishnan, K.; Bates, M. N.; Arora, N. K.; Smith, K. R., Patterns of stove usage after introduction of an advanced cookstove: the long-term application of household sensors. *Environmental science & technology* **2014,** *48*, (24), 14525-14533.

20. Delhi, R. N., Office of the Registrar General and Census Commissioner of India; 2011. *Special bulletin on maternal mortality in India* **2011,** *9*.

21. SOMAARTH, SOMAARTH Demographic Development & Environmental Surveillance Site Key Indicators Factsheet. In Somaarth.Org. Accessed on 3/2/2020. .

22. Gautam, S.; Edwards, R.; Yadav, A.; Weltman, R.; Pillarsetti, A.; Arora, N. K.; Smith, K. R., Probe-based measurements of moisture in dung fuel for emissions measurements. *Energy for sustainable development* **2016,** *35*, 1-6.

23. Johnson, M.; Edwards, R.; Ghilardi, A.; Berrueta, V.; Gillen, D.; Frenk, C. A.; Masera, O.; Technology, Quantification of carbon savings from improved biomass cookstove projects. *Environmental Science* **2009,** *43*, (7), 2456-2462.

24. Zhang, J.; Smith, K.; Ma, Y.; Ye, S.; Jiang, F.; Qi, W.; Liu, P.; Khalil, M.; Rasmussen, R.; Thorneloe, S., Greenhouse gases and other airborne pollutants from household stoves in China: a database for emission factors. *Atmospheric Environment* **2000,** *34*, (26), 4537-4549.

25. Fleming, L. T.; Weltman, R.; Yadav, A.; Edwards, R. D.; Arora, N. K.; Pillarisetti, A.; Meinardi, S.; Smith, K. R.; Blake, D. R.; Nizkorodov, S. A., Emissions from village cookstoves in Haryana, India, and their potential impacts on air quality. *Atmospheric Chemistry and Physics* **2018,** *18*, (20), 15169-15182.

26. Safety, N. I. f. O.; Health, Method 5040, Diesel particulate matter (as elemental carbon). In NIOSH Washington, DC: 2003.

27. Smith, K. R.; Uma, R.; Kishore, V.; Zhang, J.; Joshi, V.; Khalil, M., Greenhouse implications of household stoves: an analysis for India. *Annual Review of Energy the Environment* **2000,** *25*, (1), 741-763.

28. Bailis, R.; Drigo, R.; Ghilardi, A.; Masera, O., The carbon footprint of traditional woodfuels. *Nature Climate Change* **2015,** *5*, (3), 266.

29. Roden, C. A.; Bond, T. C.; Conway, S.; Pinel, A. B. O., Emission factors and real-time optical properties of particles emitted from traditional wood burning cookstoves. *Environmental science & technology* **2006,** *40*, (21), 6750-6757.

30. Rooney, B.; Zhao, R.; Wang, Y.; Bates, K. H.; Pillarisetti, A.; Sharma, S.; Kundu, S.; Bond, T. C.; Lam, N. L.; Ozaltun, B., Impacts of household sources on air pollution at village and regional scales in India. *Atmospheric Chemistry and Physics* **2019,** *19*, (11), 7719-7742.

31. Huang, Y.; Shen, H.; Chen, H.; Wang, R.; Zhang, Y.; Su, S.; Chen, Y.; Lin, N.; Zhuo, S.; Zhong, Q., Quantification of global primary emissions of PM2. 5, PM10, and TSP from combustion and industrial process sources. *Environmental science & technology* **2014,** *48*, (23), 13834-13843.

32. Jetter, J.; Zhao, Y.; Smith, K. R.; Khan, B.; Yelverton, T.; DeCarlo, P.; Hays, M. D., Pollutant emissions and energy efficiency under controlled conditions for household biomass cookstoves and implications for metrics useful in setting international test standards. *Environmental science & technology* **2012,** *46*, (19), 10827-10834.

33. Saud, T.; Mandal, T.; Gadi, R.; Singh, D.; Sharma, S.; Saxena, M.; Mukherjee, A., Emission estimates of particulate matter (PM) and trace gases (SO2, NO and NO2) from biomass fuels used in rural sector of Indo-Gangetic Plain, India. *Atmospheric Environment* **2011,** *45*, (32), 5913-5923.

34. Islam, N.; Smith, K. R., Finding a clean woodstove–A 300-year quest. *Energy for Sustainable Development* **2019,** *52*, 147-153.

35. Shen, G.; Preston, W.; Ebersviller, S. M.; Williams, C.; Faircloth, J. W.; Jetter, J. J.; Hays, M. D., Polycyclic aromatic hydrocarbons in fine particulate matter emitted from burning kerosene, liquid petroleum gas, and wood fuels in household cookstoves. *Energy & Fuels* **2017,** *31*, (3), 3081-3090.

36. van Zyl, L.; Tryner, J.; Bilsback, K. R.; Good, N.; Hecobian, A.; Sullivan, A.; Zhou, Y.; Peel, J. L.; Volckens, J., Effects of Fuel Moisture Content on Emissions from a Rocket-Elbow Cookstove. *Environmental science & technology* **2019,** *53*, (8), 4648-4656.

37. Bruce, N.; Pope, D.; Rehfuess, E.; Balakrishnan, K.; Adair-Rohani, H.; Dora, C., WHO indoor air quality guidelines on household fuel combustion: Strategy implications of new evidence on interventions and exposure–risk functions. *Atmospheric Environment* **2015,** *106*, 451-457.

38. Edwards, R. D., Bond, Tami C. , Smith, Kirk R. , Final Report: Characterization Of Emissions From Small, Variable Solid Fuel Combustion Sources For Determining Global Emissions And Climate Impact. **2019**.

39. Boucher, O.; Reddy, M., Climate trade-off between black carbon and carbon dioxide emissions. *Energy Policy* **2008,** *36*, (1), 193-200.

40. Peters, G. P.; Aamaas, B.; Berntsen, T.; Fuglestvedt, J. S., The integrated global temperature change potential (iGTP) and relationships between emission metrics. *Environmental Research Letters* **2011,** *6*, (4), 044021.

41. Allen, M. R.; Shine, K. P.; Fuglestvedt, J. S.; Millar, R. J.; Cain, M.; Frame, D. J.; Macey, A. H., A solution to the misrepresentations of CO 2-equivalent emissions of short-lived climate pollutants under ambitious mitigation. *Npj Climate and Atmospheric Science* **2018,** *1*, (1), 1-8.

42. Weyant, C. L.; Chen, P.; Vaidya, A.; Li, C.; Zhang, Q.; Thompson, R.; Ellis, J.; Chen, Y.; Kang, S.; Shrestha, G. R., Emission measurements from traditional biomass cookstoves in South Asia and Tibet. *Environmental science & technology* **2019,** *53*, (6), 3306-3314.

43. Jayarathne, T.; Stockwell, C. E.; Bhave, P. V.; Praveen, P. S.; Rathnayake, C. M.; Islam, M.; Panday, A. K.; Adhikari, S.; Maharjan, R.; Goetz, J. D., Nepal Ambient Monitoring and Source Testing Experiment (NAMaSTE): emissions of particulate matter from wood-and dung-fueled cooking fires, garbage and crop residue burning, brick kilns, and other sources. *Atmospheric Chemistry and Physics* **2018,** *18*, (3), 2259-2286.

44. Dang, J. In Field Measurements of Solid Fuel Cookstove Emissions. UC Irvine, 2016.

45. Garland, C.; Delapena, S.; Prasad, R.; L'Orange, C.; Alexander, D.; Johnson, M., Black carbon cookstove emissions: A field assessment of 19 stove/fuel combinations. *Atmospheric environment* **2017,** *169*, 140-149.

Chapter 4

AIR QUALITY IMPACT OF THE NORTHERN CALIFORNIA CAMP FIRE
OF NOVEMBER 2018

Rooney, B., Y. Wang, J.H. Jiang, B. Zhao, K.R. Verhulst, Z. Zeng, J.H. Seinfeld, (2020). "Air Quality Impact of the Northern California Camp Fire of November 2018". *In preparation.*

4.1 Introduction

Wildfires have become increasingly prevalent in California. It has been reported that between 2007 and 2016, as many as 3672 fires occurred in California, consuming up to 434,667 acres (Pimlott et al., 2016). Increasingly, the population has expanded into high fire-risk areas and near wildland-urban interfaces (Brown et al., 2020). The intense smoke consisting of airborne particulate matter of diameter < 2.5 micrometers ($PM_{2.5}$) associated with these fires leads to an increased risk of morbidity and mortality (Cascio, 2018). $PM_{2.5}$ from wildfires consists of a spectrum of light scattering and absorptive particles largely comprising organic and black carbon. It is increasingly important to understand the cause and nature of wildfires as the number of extreme events and the length of the wildfire season continue to grow (Kahn, 2020; Shi et al., 2019). Fire-related studies have estimated exposures to $PM_{2.5}$ based on ground-level monitoring-station measurements (Shi et al., 2019; Herron-Thorpe et al., 2014; Archer-Nicholls et al., 2015). Spatial coverage of such monitoring stations often tends to be scarce, especially in rural areas. Satellite remote sensing offers a powerful method to monitor air quality during fire events. One study used radiance measurements from the TROPOspheric Monitoring Instrument (TROPOMI) to derive atmospheric carbon monoxide and assess the resulting air quality burden in major cities due to emissions from the California wildfires from November 2018 (Schneising, et al., 2020). Ideally, analysis of fire events is based on a combination of satellite-based measurements and ground-level observations to obtain spatial and temporal distributions of emissions. The Camp Fire of November 2018 was, to date, the deadliest and most destructive wildfire in California (Kahn,

2020; Brown et al., 2020). Originating along the Sierra Nevada mountain range, smoke from the fire spread across the Sacramento Valley to the San Francisco Bay Area. Peak levels of $PM_{2.5}$ in the San Francisco area exceeded 200 µg m^{-3} and remained above 50 µg m^{-3} for nearly two weeks.

Numerous studies have addressed wildfire events using a variety of model frameworks and data sources (Shi et al., 2019; Herron-Thorpe et al., 2014; Archer-Nicholls et al., 2015; Sessions et al., 2011). Shi et al. (2019) used the WRF-Chem model with Moderate Resolution Imaging Spectroradiometer (MODIS) and VIIRS fire data to study the wildfire of December 2017 in Southern California. Herron-Thorpe et al. (2014) evaluated simulations of the wildfires in the Pacific Northwest of 2007 and 2008 using the Community Multi-scale Air Quality (CMAQ) model with fire emissions generated by the BlueSky framework and fire locations determined by the Satellite Mapping Automated Reanalysis Tool for Fire Incident Reconciliation (SMART-FIRE). That study suggested that underprediction of $PM_{2.5}$ was the result of underestimated burned area as well as underpredicted secondary organic aerosol (SOA) production and incomplete speciation of SOA precursors within the CMAQ model. Archer-Nicholls et al. (2015) simulated biomass burning aerosol during the 2012 dry season in Brazil using WRF-Chem and fire emissions prepared from MODIS. That study proposed that biases in the model were likely a result of uncertainty in the plume injection height and emissions inventory, as well as simulated aerosol sinks (e.g., wet deposition), and lack of inclusion of SOA production in the Model for Simulating Aerosol Interactions and Chemistry (MOSAIC). Sessions et al. (2011) investigated methods for injecting wildfire emissions using WRF-Chem. That study tested two fire data preprocessors: PREP-CHEM-SRC (included with WRF-Chem) and the Naval Research Laboratory's Fire Locating and Monitoring of Burning Emissions (FLAMBE), and three injection methods: the 1-D plume rise model within WRF-Chem, releasing emissions only within the planetary boundary layer, and releasing emissions between 3 and 5 km. That study compared results from simulating wildfires during the NASA Arctic Research of the Composition of the Troposphere from Aircraft and Satellites (ARCTAS) field campaign in

2008 with satellite data. Sessions et al. (2011) found that differences in injection heights result in different transport pathways.

The present study is a comprehensive investigation of air quality impacts of the Camp Fire using a combined analysis of ground-based and space-borne observations and WRF-Chem simulations. Descriptions of the observation and model are presented in Section 2; model evaluation is presented in Section 3; results of analysis are given in Section 4, followed by discussion and conclusion in Section 5.

4.2 Model Description and Observational Data

The present study employs WRF-Chem (version 3.8.1) driven by the latest version of meteorological reanalysis data for initialization and boundary conditions. Fire emissions are determined by pairing active fire location data from VIIRS Satellite with the Brazilian Biomass Burning Emission Model (3BEM), which calculates species mass emissions from the burned biomass carbon density, combustion factors, emission factors, and the burning area. WRF-Chem simulations are evaluated against EPA surface observations and TROPOMI satellite products.

4.2.1 WRF-Chem Configuration

The WRF-Chem simulation time period is 7 November 2018 (a day before the fire began) to 22 November 2018 (when the fire was 90% contained). We carried out simulations over two domains (Fig. 4.1): Domain 1 includes all of California at 8 km × 8 km horizontal resolution, while Domain 2 covers Northern California at 2 km × 2 km horizontal resolution. 49 vertical layers are used from the surface to 100 hPa with 50 m vertical resolution in the planetary boundary layer. The meteorological boundary and initial conditions for the outer domain are generated from the fifth generation of European Centre for Medium-range Weather Forecasts (ECMWF) Re-Analysis dataset (ERA5) at 30 km × 30 km resolution (Copernicus Climate Change Service, 2017). Chemical boundary and initial conditions for the outer domain are generated from the Model for Ozone and Related

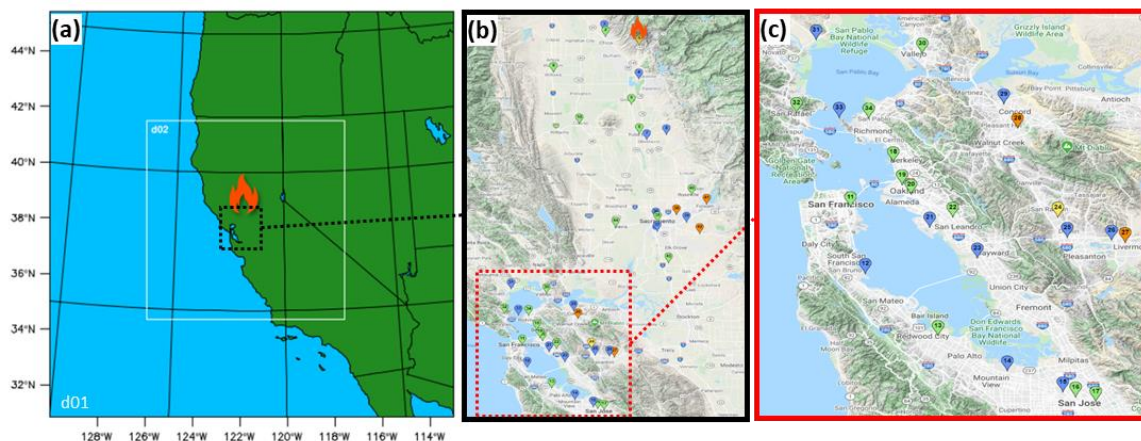Chemical Tracers version 4 (MOZART-4) (University Corporation for Atmospheric Research, 2013).

Figure 4.1. Study domain (a) and observation station locations (b,c). Domain d01 covers the western US with a horizontal resolution of 8 km. Domain d02 is centered over northern California with a horizontal resolution of 2 km. AQS and NCDC observation sites are shown in panel b and panel c, where stations marked in green measure only PM$_{2.5}$, stations in blue measure wind and temperature, stations in orange measure both PM$_{2.5}$ and meteorology, and stations in yellow measure temperature only. Additionally, BC and CO are measured at 8 and 12 sites in the Bay Area, respectively.

We use physical options of the Noah Land-Surface Model (Tewari et al., 2004), the Mellor-Yamada-Janjic (MYJ) boundary layer scheme (Janjic, 1994), and the RRTM (longwave) and Dudhia (shortwave) radiative transfer schemes (Dudhia, 1989). Cumulus parameterization is not included. The second-generation Regional Acid Deposition Model (RADM2) chemical mechanism coupled with the Modal Aerosol Dynamics model for Europe (MADE) and Secondary Organic Aerosol Model (SORGAM) (Zhao et al., 2011) are employed. Aerosol optical properties are calculated based on the volume approximation, for which the volume average of each aerosol species is used to calculate refractive indices (Jin, et al., 2015). Aerosol radiative feedbacks on meteorology and chemistry are included in the simulations.

We use the National Emission Inventory for anthropogenic emissions (US EPA, 2018). Biogenic emissions are calculated online using the Guenther scheme (Guenther et. al., 2006). Dust emissions are calculated online using the Goddard Chemical Aerosol Radiation Transport (GOCART) dust emission scheme with University of Cologne (UOC)

modifications (Shao et al., 2011). Sea salt emissions are excluded. Technical details of wildfire emissions and the plume rise calculation are discussed in the next section.

4.2.2 Fire Emissions Inventory and Plume Rise Model

Wildfire emissions are generated using the PREP-CHEM-SRC v1.5 preprocessor (Freitas et al., 2011) employing the Brazilian Biomass Burning Emission Model (3BEM, Longo et al., 2010) with satellite data on detected fires. For each pixel with fire detected, the mass of emitted species is calculated by:

$$M^{[\eta]} = \alpha_{veg} \cdot \beta_{veg} \cdot EF_{veg}^{[\eta]} \cdot a_{fire} \qquad (1)$$

for a certain species η, where α_{veg} is the carbon density (the mass of burnable above-ground biomass per unit area of vegetation), β_{veg} is the combustion factor, EF_{veg} is the emission factor by species and vegetation type, and a_{fire} is the burning area of each fire pixel.

Active fire detection is retrieved from the VIIRS fire product with 375 m spatial resolution. Vegetation type is generated from the MODIS data following IGBP land cover classification. Vegetation type-specific emission factors and combustion factors are derived from Ward et al. (1992) and Andreae and Merlet (2001). Carbon density is based on Olson et al. (2000) and Houghton et al. (2001). A limitation of the VIIRS fire count product is its relatively low temporal resolution. As a polar-orbiting satellite, VIIRS provides fire detection during the daytime only once (about 13:30 local time) at each location. In the absence of data to the contrary, we assume equal fire emission rates for each hour of the day.

The emission preprocessor generates a file formatted for WRF-Chem containing the smoldering-phase surface emission fluxes of each species, the fire size for each vegetation type, and flaming factor. Flaming factor is the ratio of biomass consumed in the flaming phase to biomass consumed in the smoldering phase. The 17 IGBP land cover classes are aggregated into four main types: tropical forest, extratropical forest, savanna, and grassland. The size of the wildfire and phase of combustion play important roles in the structure of the plume and the vertical distribution of emissions. Wildfire combustion is generally considered to occur in two phases: smoldering and

flaming. Emissions from the smoldering phase are allotted to the first layer of the computational grid, while those from the flaming phase are released at injection heights above the surface, as determined by the plume rise model described below. Fire size determines the total surface heat flux, as well as the entrainment radius of the plume. Fire parameters are ascribed a daily temporal resolution and are distributed to the WRF-Chem domains. The fire parameters are then input to the plume rise model (Freitas et al., 2007, 2010). The plume rise model is a 1-dimensional model implemented in each WRF-Chem grid cell with an independent vertical grid resolution of 100 m. It calculates the maximum height to which a plume reaches and distributes emissions therein (Fig. 4.2). The plume top height, determined by the surface heat flux from the fire and the thermodynamic stability of the atmospheric environment, is defined as the height at which the in-plume parcel vertical velocity < 1 m s^{-1}. The plume rise model uses upper and lower bounds of heat fluxes determined by each land type to calculate the minimum and maximum plume top height. Flaming emissions are distributed equally to each vertical level within the injection layer with the following calculation: *Flaming Emission per Level = Smoldering Emission × Flaming Factor × DZ^{-1}*, where *DZ = Maximum Plume Top Height – Minimum Plume Top Height*. The model also accounts for entrainment, water balance, and internal gravity wave damping.
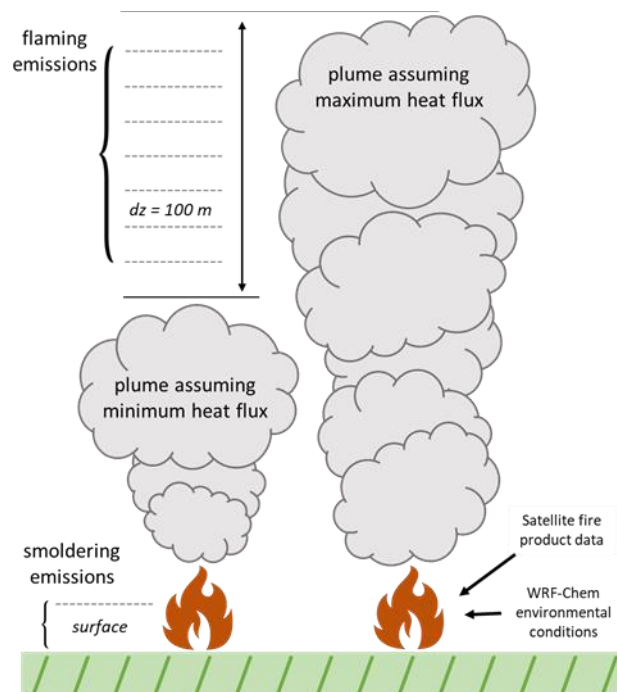
Figure 4.2. Plume rise model schematic. For each grid cell in which wildfire occurs, the plume rise model uses satellite fire products and the surrounding WRF-Chem environmental conditions to calculate two plume top heights by using the land-type dependent minimum and maximum wildfire heat fluxes. Smoldering phase emissions are allotted to the surface layer, while flaming phase emissions are distributed linearly aloft within the injection layers at a vertical resolution of 100 m.

Figure 4.3 shows the fire size and particulate matter emissions produced from MODIS and VIIRS data. The Camp Fire burned primarily extratropical forest vegetation (which comprised 68% of the total burned area), followed by savanna (23% of total area). The flaming emission rate for species *n* from vegetation type *v*, is calculated by

$$Flaming\ Phase\ Rate_{n,v} = \sum\nolimits_{Fire\ Cells} Area_v \cdot Smoldering\ Phase\ Flux_n \cdot Flaming\ Factor_v \quad (2)$$

At maximum, the carbon monoxide (CO) emission flux was 4.1×10^7 mol km^{-2} hr^{-1}, and PM$_{2.5}$ flux was 3.7×10^4 µg m^{-2} s^{-1}. On average, 46% of the fuel burned is estimated to have been consumed during the flaming phase.
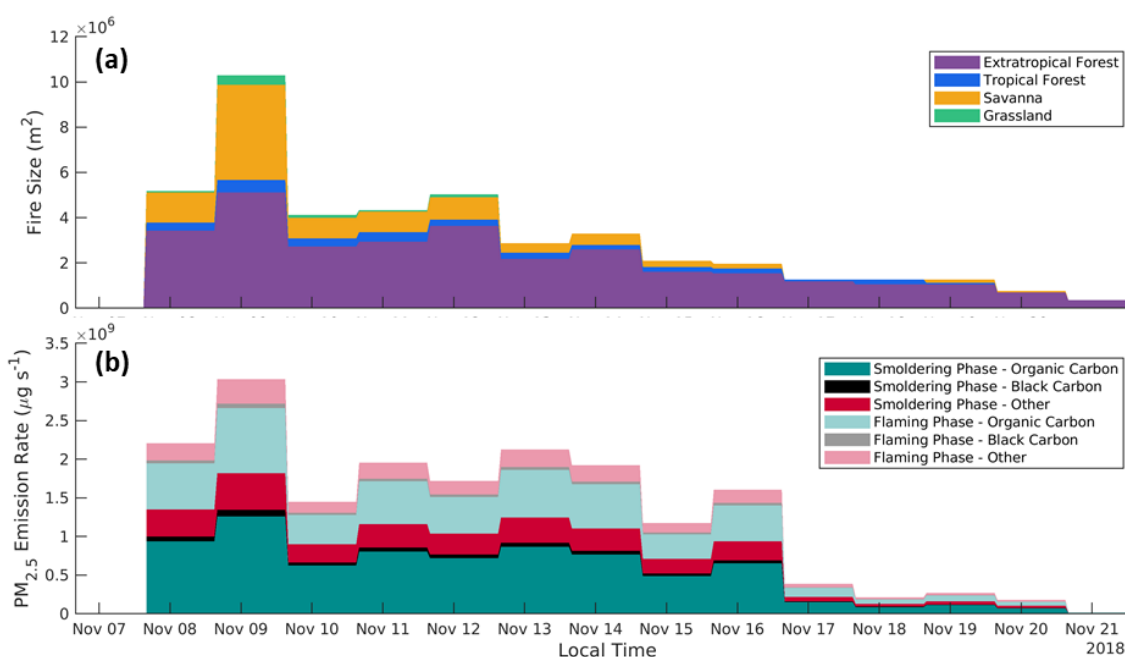
Figure 4.3. Wildfire area by vegetation type in m² (a) and PM$_{2.5}$ emission rate in µg s⁻¹ by combustion phase and species (b) input into WRF-Chem. The base inventory is produced from VIIRS and MODIS fire products using the PREP-CHEM-SRC processor and is employed by S_EMRAW. The control and remaining sensitivity simulations use an inventory with triple emission flux of all species on 13 November and double during 13-16 November, shown here. About 59% of total PM$_{2.5}$ emissions occur in the smoldering phase (darker colors in panel b). The total PM$_{2.5}$ emitted is composed of 69.5% organic carbon and 4.5% black carbon. The Camp Fire burned primarily extratropical forest (purple) followed by savanna (yellow). Burning of extratropical forest generated the greatest fraction of emissions in the flaming phase at 44.2%, followed by savanna at 22.9% and tropical forest at 17.4%. Grassland emits only in the smoldering phase.

Fire Inventory from NCAR (FINN) Version 1.5 (Wiedinmyer, 2011) is another fire emissions product that we will test in a sensitivity analysis. It is assembled for atmospheric chemistry models with a daily temporal resolution and a 1 km horizontal resolution. FINN is generated using satellite observations of active fires and land cover paired with emission factors and fuel loading estimates. The emissions are allocated to a diurnal cycle following WRAP (2005). FINN outputs the total wildfire emission flux, fire size, and land type fraction. As FINN does not include a smoldering-to-flaming phase ratio, the plume rise model calculates a ratio based on CO emissions.

4.2.3 Surface and Satellite Observations

The observational data include both ground-based measurements and satellite observations. Meteorological and surface concentration data were obtained from the NOAA's National Climatic Data Center (NCDC) and EPA Air Quality System (AQS), respectively. We focus on three areas: the region closest to the fire, the Sacramento Metro Area (population of 2.5 million), and the San Francisco Bay Area (population of 7 million). Hourly observations of wind speed at 10 m, wind direction at 10 m, temperature at 2 m, $PM_{2.5}$, black carbon (BC), and CO are available for the sites shown in Fig. 4.1. We use level-2 products from the TROPOMI onboard the Copernicus Sentinel-5 Precursor satellite (S5P) to evaluate the spatial and vertical distribution of predictions. We compare TROPOMI aerosol layer height retrievals (3.5 km × 7 km) with the predicted WRF-Chem height of maximum $PM_{2.5}$, and ultraviolet aerosol index (UVAI, 3.5 km × 7 km) with the predicted WRF-Chem BC columns. The model results are sampled around 13:30 local time when S5P passes over California.

4.2.4 Control and Sensitivity Simulations

To investigate the effects of key model parameters on the ability to predict the atmospheric impact of the wildfire, we conduct a range of sensitivity simulations. As meteorology and atmospheric structure play important roles in plume dynamics and the transport of particulate matter, we separately perturb the aerosol radiative feedback to meteorology, the planetary boundary layer parameterization, and the plume entrainment coefficient. To understand further the extent to which fire characteristics provided by satellite data can affect the simulations, we analyze the influence of fire data sources, the emission rate, and partitioning between smoldering phase and flaming phase emissions. A summary of these simulations is provided in Table 4.1.

Table 4.1. Summary of sensitivity simulation setup.

Name	Fire Data	Smoldering Emissions	Flaming Factor	Entrainment Constant	LSM	Aerosol Radiative Feedback
S_CTRL[1]	VIIRS	x3 Nov. 13, x2 Nov. 14-16	Native	0.05	Noah/ MYJ	Yes
S_EMRAW	VIIRS	**Native**	Native	0.05	Noah/ MYJ	Yes
S_NOAERO	VIIRS	x3 Nov. 13, x2 Nov. 14-16	Native	0.05	Noah/ MYJ	**No**
S_FCTX2	VIIRS	x3 Nov. 13, x2 Nov. 14-16	**x2**	0.05	Noah/ MYJ	Yes
S_ENTR	VIIRS	x3 Nov. 13, x2 Nov. 14-16	Native	**0.02**	Noah/ MYJ	Yes
S_LSM	VIIRS	x3 Nov. 13, x2 Nov. 14-16	Native	0.05	**P-X/ ACM2**	Yes
S_FINN	**FINN**	-	-	0.05	Noah/ MYJ	Yes

[1]Scenario that agrees best with surface observations and is of primary focus in this study. Bold denotes parameter perturbed from the S_CTRL scenario.

Our evaluation focuses on the control simulation (S_CTRL). S_CTRL applies a factor of 3 to the smoldering emissions on 13 November and a factor of 2 to the smoldering emissions on 14-16 November due to the intermittent cloudy conditions over the northern California on those days. S_CTRL uses the native flaming factor and fire size products, the default entrainment constant of 0.05, and the Mellor-Yamada-Janjic planetary boundary layer scheme. In the following scenarios, one parameter is individually perturbed from this configuration. S_EMRAW uses the native emissions input with unaltered smoldering phase emissions, S_NOAERO turns off the aerosol radiative feedback to meteorological fields, S_FCTX2 doubles the flame factor for the entire simulation period (thus increasing flaming phase emissions without changing the smoldering phase), S_ENTR reduces the entrainment coefficient within the plume rise model from 0.05 to 0.02, and S_LSM

employs an alternative land surface model and planetary boundary layer scheme. We perform another sensitivity simulation using FINN in place of VIIRS (S_FINN).

4.3 Evaluation of Fire Simulations

4.3.1 Meteorology

The three spatial areas of our interest differ significantly in topography and meteorology. Figure 4.4 shows the averaged wind observations and S_CTRL predictions. S_CTRL captures general wind patterns and achieves strong correlation with observed temperatures in each of the areas (Fig. 4.5). In the first few days of the Camp Fire, the foothills and the Sacramento area experienced strong northerly winds, while the Bay Area experienced northeasterly winds, both predicted by the simulation. Other distinct features like those on 11 November near the fire and in the Bay Area are also reproduced by S_CTRL with some bias in timing. In the Bay Area, winds were typically southerly at speeds less than 2 m s^{-1} and consistent through most of the simulation duration. In the relatively dry Sacramento Valley inland, winds were also predominantly southerly, but were calmer (< 1 m s^{-1}) and varied more than those on the coast. After 11 November, the wind speeds were much slower. Coastal air regulates Bay Area temperatures, whereas the drier Sacramento area experiences a greater temperature range. S_CTRL also produced these relative characteristics, but, in general, generated faster winds and higher temperatures than those observed. A summary of model performance statistics is provided in Table 4.2. The complex terrain of the Bay Area and the Sierra Nevada Foothills near the fire location likely contribute to uncertainty in predicting meteorological parameters.
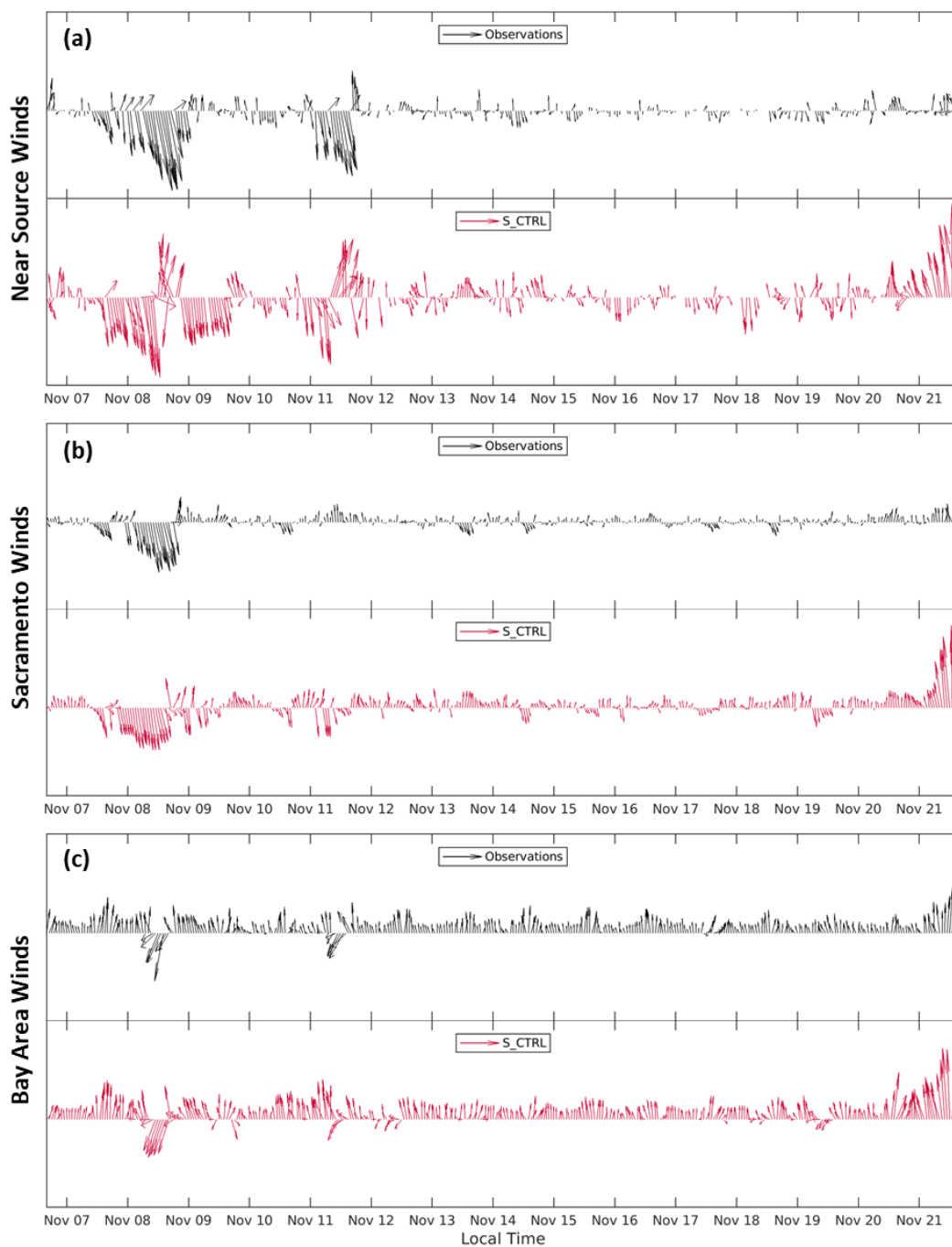
Figure 4.4. Comparison of AQS and NCDC wind observations (black) with S_CTRL predictions (red) averaged over the three areas of study: a) near the wildfire (N = 4), b) Sacramento (N = 6), and c) the Bay Area (N = 12). Arrows indicate the wind direction and their length represents wind speed. For reference, S_CTRL predicts maximum wind speeds of 8.7, 7.5, and 7.1 m s^{-1} near the source, in Sacramento, and in the Bay Area, respectively. Paradise and the Sacramento areas experienced strong northerly winds during the first few days of the fire. S_CTRL generally predicted faster and more variable winds, but broader trends in Sacramento and the Bay Area were represented well.
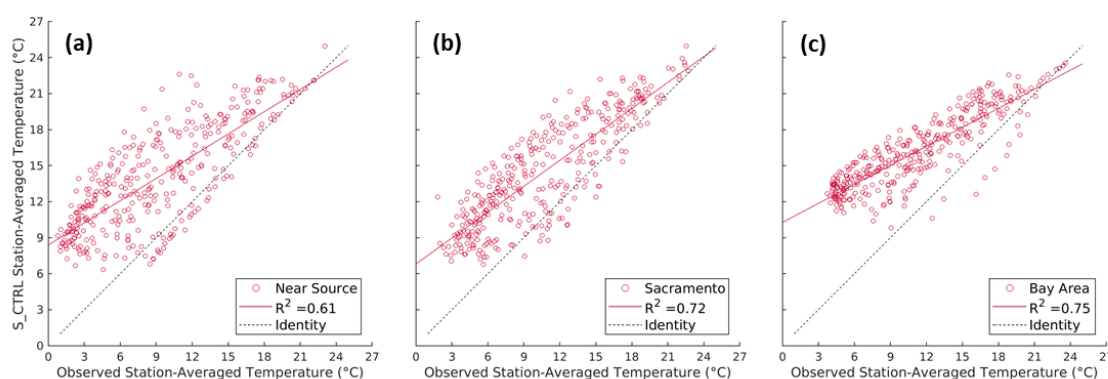
Figure 4.5. Comparison of AQS and NCDC temperature observations versus S_CTRL predictions: a) near the wildfire (N = 10), b) Sacramento (N = 7), and c) the Bay Area (N = 13). The solid red lines show a linear regression fit, while the dotted black lines denote 1:1 simulations vs. observations. The simulations achieved a correlation coefficient R^2 of 0.61 near the fire, 0.72 in Sacramento, and 0.75 in the Bay Area.

Table 4.2. Summary of meteorological model performance metrics for the simulation duration.

Variable	Parameter	Near Source[1]	Sacramento[1]	Bay Area[1]	Station 27	Station 28
Wind Speed[2] (m s^{-1})	Observation Mean	1.4 (0.2)	1.0 (0.2)	1.6 (0.7)	1.5	0.7
	S_CTRL Mean	2.6 (0.3)	1.4 (0.4)	2.0 (0.7)	2.3	1.0
	Mean Bias	1.2	0.5	0.5	0.9	0.3
Wind Direction[3] (deg)	Observation Mean	360.0	338.2	73.9	68.9	148.8
	S_CTRL Mean	356.9	325.9	26.7	72.8	11.8
	Mean Bias	2.9	11.0	0.2	2.8	10.1
Temp (°C)	Observation Mean	8.2 (2.3)	10.1 (1.7)	10.8 (1.9)	9.9	8.1
	S_CTRL Mean	12.5 (3.6)	13.7 (1.4)	15.7 (1.2)	15.5	13.8
	Mean Bias	4.4	3.6	4.9	5.6	5.7

[1]Area winds are averaged for 4 stations near source, 6 stations in Sacramento, and 12 stations in the Bay Area. Area temperatures are averaged for 10 stations near source, 7 in Sacramento, and 13 in the Bay Area. Standard deviation of station averages is noted in parenthesis.
[2]Mean wind speed is calculated as the average of the magnitude of the wind vector.
[3]Mean wind direction is calculated assuming a unity vector.

4.3.2 Surface-Level Particulate Matter

Figure 4.6 shows the predicted evolution of surface $PM_{2.5}$ from AQS observations and S_CTRL over the period of the wildfire. Within hours of the onset of the Camp Fire, observed $PM_{2.5}$ concentrations in Sacramento and the San Francisco Bay Area (130 and 240 km downwind) increased from below the National Ambient Air Quality Standard (NAAQS) 24-h average of 35 µg m^{-3} to 50 µg m^{-3}. Both areas remained above the standard for more than a week, reaching values of three times the standard for multiple days. The region near the fire, Sacramento, and the San Francisco Bay Area were each out of attainment of the NAAQS 24-h average of $PM_{2.5}$ for 11, 11, and 12 days, respectively, during 7-20 November, while S_CTRL predicted 12, 11, and 11 days, respectively. Much of northern California did not return to attainment until 22 November when the wildfire reached 90% containment. Table 4.2 summarizes the ability of S_CTRL to reproduce observed values of surface $PM_{2.5}$ in the three focus areas and at stations 27 and 28 in the Bay Area. The model prediction exhibits a mean bias of 64.8 µg m^{-3} in the region of the Camp Fire, -11.4 µg m^{-3} in Sacramento, and -16.8 µg m^{-3} in the Bay Area. Mean bias was smaller at some individual monitoring stations, such as Station 27 and 28 that has mean bias of -9.9 µg m^{-3} and -6.2 µg m^{-3}, respectively. In the broader area near the fire, S_CTRL significantly overestimates surface $PM_{2.5}$, reaching nearly 1 mg m^{-3} while observed concentrations peaked closer to 300 ug m^{-3}. However, S_CTRL shows a similar temporal trend to that observed, capturing many peak times. The Sacramento area experienced maxima near 300 µg m^{-3}, while the Bay Area reached around 200 µg m^{-3}. S_CTRL shows good agreement of the magnitude and temporal evolution of surface $PM_{2.5}$ in the Bay Area and Sacramento for most days, with the exception of 10 November and 14-16 November (to be discussed subsequently). Time series of observed and predicted surface CO and BC in the Bay Area are shown in Fig. 4.7. Again, S_CTRL shows good agreement with the magnitude and trend of both species. While $PM_{2.5}$ is largely underpredicted in the period of 14-16 November, BC is over predicted by 5-10 µg m^{-3} at peaks. S_CTRL also produces positive bias in surface CO over 16-18 November.
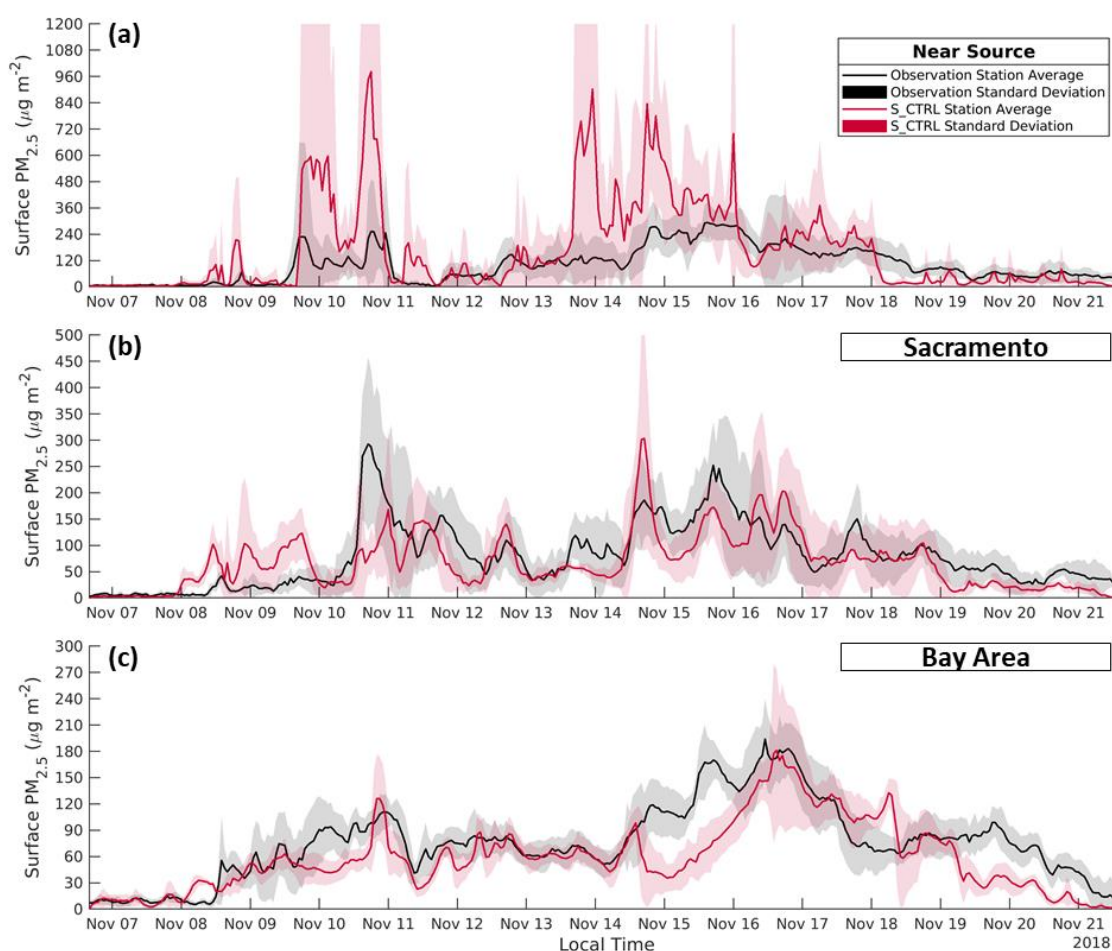
Figure 4.6. Comparison of AQS surface PM$_{2.5}$ observations (black) with S_CTRL predictions (red) averaged over the three areas of study: a) near the wildfire (N = 5), b) Sacramento (N = 7), and c) the Bay Area (N = 13). Shading indicates the standard deviation of the sampled stations. S_CTRL overpredicted PM$_{2.5}$ in the region in the vicinity of the fire but performed well in the areas downwind.

Table 4.3. Summary of model performance metrics for surface PM$_{2.5}$ (µg m^{-3}) for the simulation duration.

Parameter	Near Source*	Sacramento*	Bay Area*	Station 27	Station 28
Observation Mean	98.3 (39.7)	77.2 (24.9)	74.1 (5.4)	77.9	69.8
S_CTRL Mean	163.1 (108.5)	65.8 (16.3)	57.2 (6.4)	68.1	63.6
Mean Bias	64.8	-11.4	-16.8	-9.9	-6.2
Normalized Mean Bias	76.5%	-17.4%	-23.1	-12.7%	-8.9%

*Area values are averaged for 5 stations near source, 7 stations in Sacramento, and 13 stations in the Bay Area. Standard deviation of station averages is noted in parenthesis.

Error in surface PM$_{2.5}$ can, in part, be attributed to error in the predicted wind fields. In the latter hours of 8 November near the Camp Fire, S_CTRL predicts southerly winds, while observations are steadily northerly, leading to some return of initially transported plume. Again, on 11 November, predicted winds show a dramatic reversal, and surface PM$_{2.5}$ spikes. In Sacramento on 10 November, observed and predicted northerly winds at midday initially lead to increased PM$_{2.5}$ concentrations, but winds swing southerly in the later hours. On 13 November, observed winds blow south and transport emissions to Sacramento, while S_CTRL predicts winds in the opposing direction, leading to an underprediction in PM$_{2.5}$. However, error in predicted wind fields does not explain the substantial underprediction of surface PM$_{2.5}$ in the Bay Area over 14-16 November, as the station-averaged winds of the area do not show significant deviation from observations. We tested the Four-Dimensional Data Assimilation (FDDA) of large-scale horizontal wind from the ERA5, but it could not reduce the aforementioned biases in wind, possibly due to the fact that the observed wind patterns are driven by some mesoscale or even local-scale dynamics.
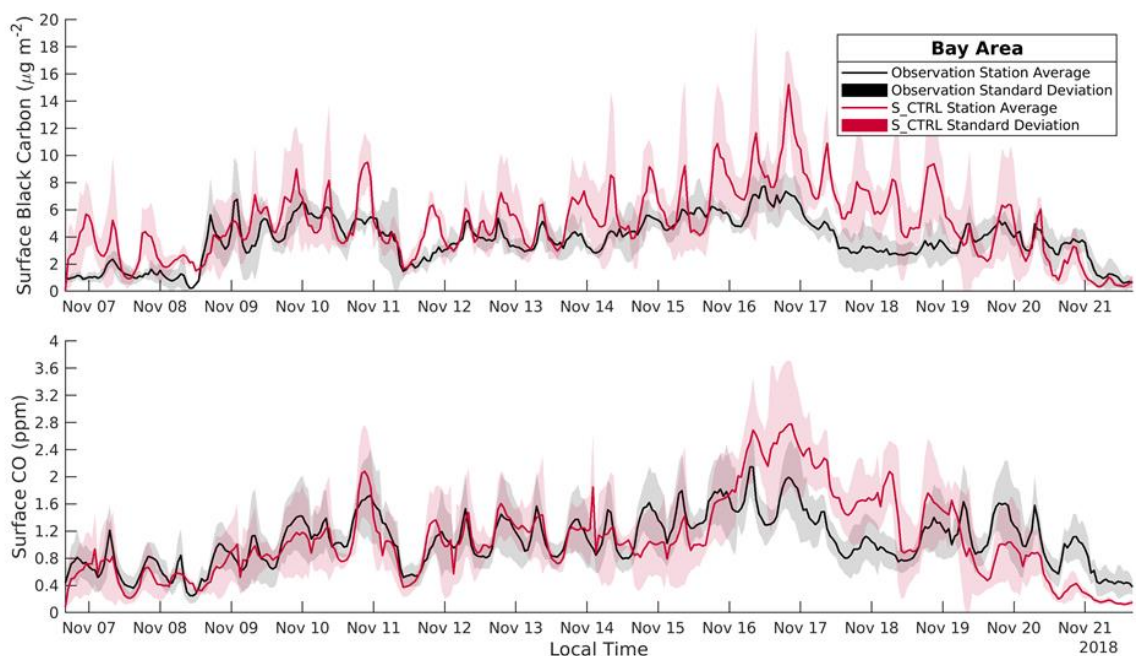

Figure 4.7. Comparison of AQS surface black carbon (a, N = 5) and carbon monoxide (b, N = 12) observations (black) with S_CTRL predictions (red) at monitoring sites in the Bay Area. S_CTRL captures the temporal evolution of BC and CO and is close to observed values. BC peaks are often overpredicted. The greatest bias of BC and CO occurs during 16-18 November, likely due to the scale factor applied to emissions during 13-16 November.

To study the structural evolution of the wildfire plume, we compare simulated total black carbon column with TROPOMI UVAI satellite retrievals (Fig. 4.8). TROPOMI UVAI is based on the difference between wavelength-dependent Rayleigh scattering observed in an atmosphere with aerosols and that of a modeled molecular atmosphere (Stein Zweers et al., 2018). This difference is measured in the UV spectral range where ozone absorption is small. A positive residual (red coloring) indicates the presence of UV-absorbing aerosols, like black carbon (BC), while a negative residual (blue coloring) indicates presence of non-absorbing aerosols. As WRF-Chem does not generate an aerosol index parameter, we compare UVAI to total BC column, a significantly absorbing aerosol. Over the period of the simulation, broad characteristics and shape, as well as some more distinct features, of the Camp Fire plume are reproduced by S_CTRL. Using similar input data sources and WRF-Chem configuration, but a simpler plume rise model, Shi et al. (2019) also capture the general shape of the plume, but underestimate aerosol magnitude. Discrepancies in S_CTRL plume transport correlate to bias in surface $PM_{2.5}$. On the first day of the fire, observations show that strong winds in northern California drag the plume west, where steady coastal winds transported the plume south and inland again (Fig. 4.8). The dynamics creates a dense plume with two narrow stretches. S_CTRL predictions of total BC column fail to capture the hook-shape present in the UVAI retrievals but reflect the two separate stretches of narrow plume. The simulation constrains one stretch to the valley, leading to overprediction of surface $PM_{2.5}$ in Sacramento on 8 November (Fig. 4.6b). On 11 November, the simulation does not reproduce the second band of the plume which wraps along the coast and towards San Francisco; rather, the plume remains more concentrated to the Sacramento Valley again. This leads to underprediction of surface $PM_{2.5}$ in the Bay Area and overprediction in Sacramento (Fig. 4.6b and c). The narrow $PM_{2.5}$ peaks of S_CTRL on 14-16 November in Sacramento can likely be attributed to the more pronounced plume on 14 November and 16 November. A stark horizontal gradient of fire emissions could restrict accumulation of $PM_{2.5}$ averaged over the Sacramento region.
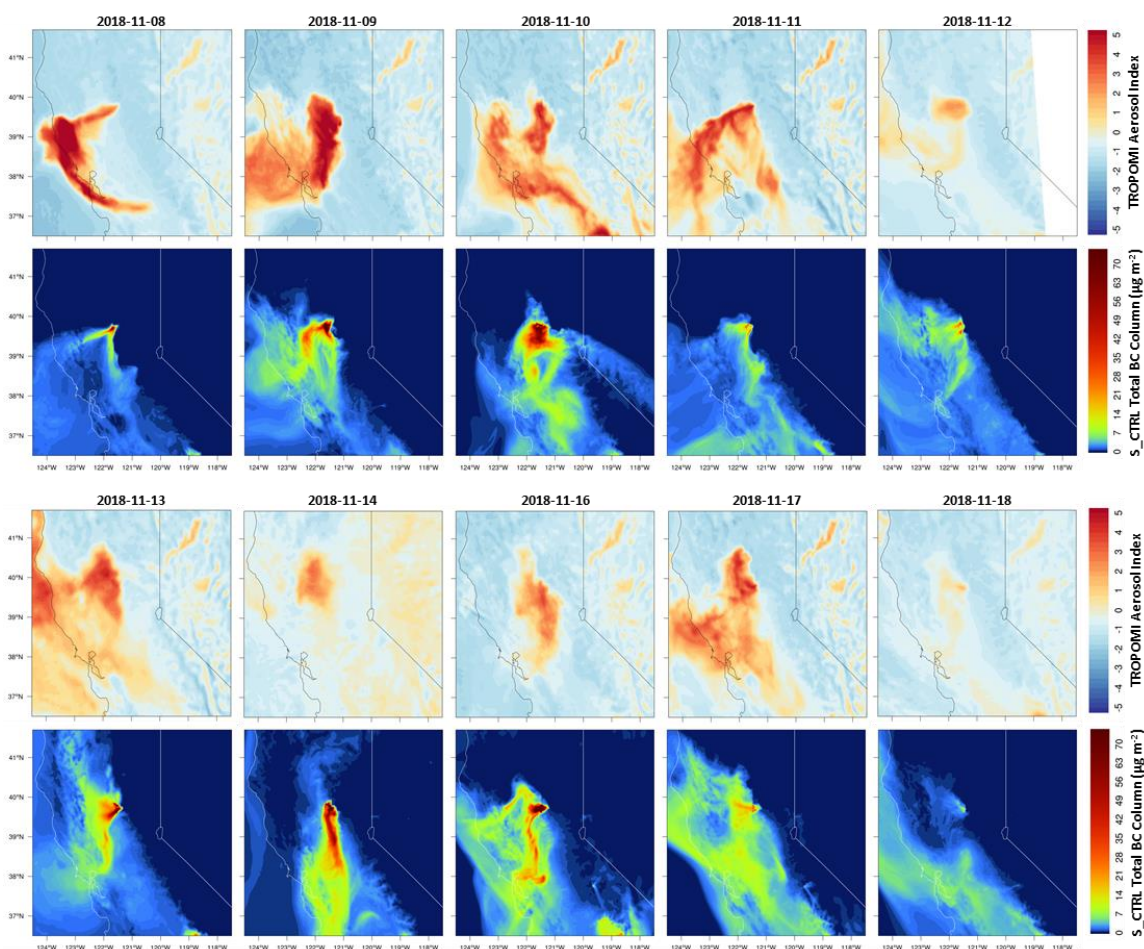
Figure 4.8. Comparison of TROPOMI UV aerosol index and S_CTRL total BC column during 8-18 November at 13:30 local time as a proxy for plume structure and motion. Due to cloud coverage, no data for 15 November are shown. Positive aerosol index (warm colors) indicates aerosols that absorb radiation like black and brown carbon. The spatial distribution of the plume is generally captured on most days. The simulation also captures some of the finer structures seen by the satellite, though somewhat displaced.

To investigate the predicted decrease of surface $PM_{2.5}$ in the Bay Area in the afternoon of 14 November, we individually analyze station 27 (Fig. 4.9) and station 28 (Fig. 4.10). Figures 4.9 and 4.10 show the vertical profile of S_CTRL $PM_{2.5}$ concentrations, the observed and predicted surface $PM_{2.5}$, and the observed and predicted wind fields. Additionally, Fig. 4.11 shows the spatial distribution of $PM_{2.5}$ and surface winds of observations (a) and predictions (b) at four times on 14 November. In the late morning at station 27, observed winds become northeasterly and $PM_{2.5}$ spikes as more particle-laden air flows westward (Fig. 4.10). At the same time, S_CTRL winds also become northeasterly and $PM_{2.5}$ increases accordingly.

However, predicted winds reverse, and PM$_{2.5}$ levels remain relatively low from midday 14 November to midday 15 November. Station 28 exhibits similar behavior of an increase in PM$_{2.5}$ with wind change, then a sharp drop as predicted winds deviate strongly northward. This behavior emerges as part of a larger flow pattern in Fig. 4.11. Throughout the morning of 14 November, the simulated wildfire plume approaches the Bay Area and is then driven back inland by a strong sea breeze in the afternoon, not present in the observational data. This behavior is also demonstrated in the vertical profile of PM$_{2.5}$ (Fig. 4.9a and 4.12a). A column of clean air flushing the Bay Area leads to a predicted bias of -50 µg m^{-3} on 15 November.
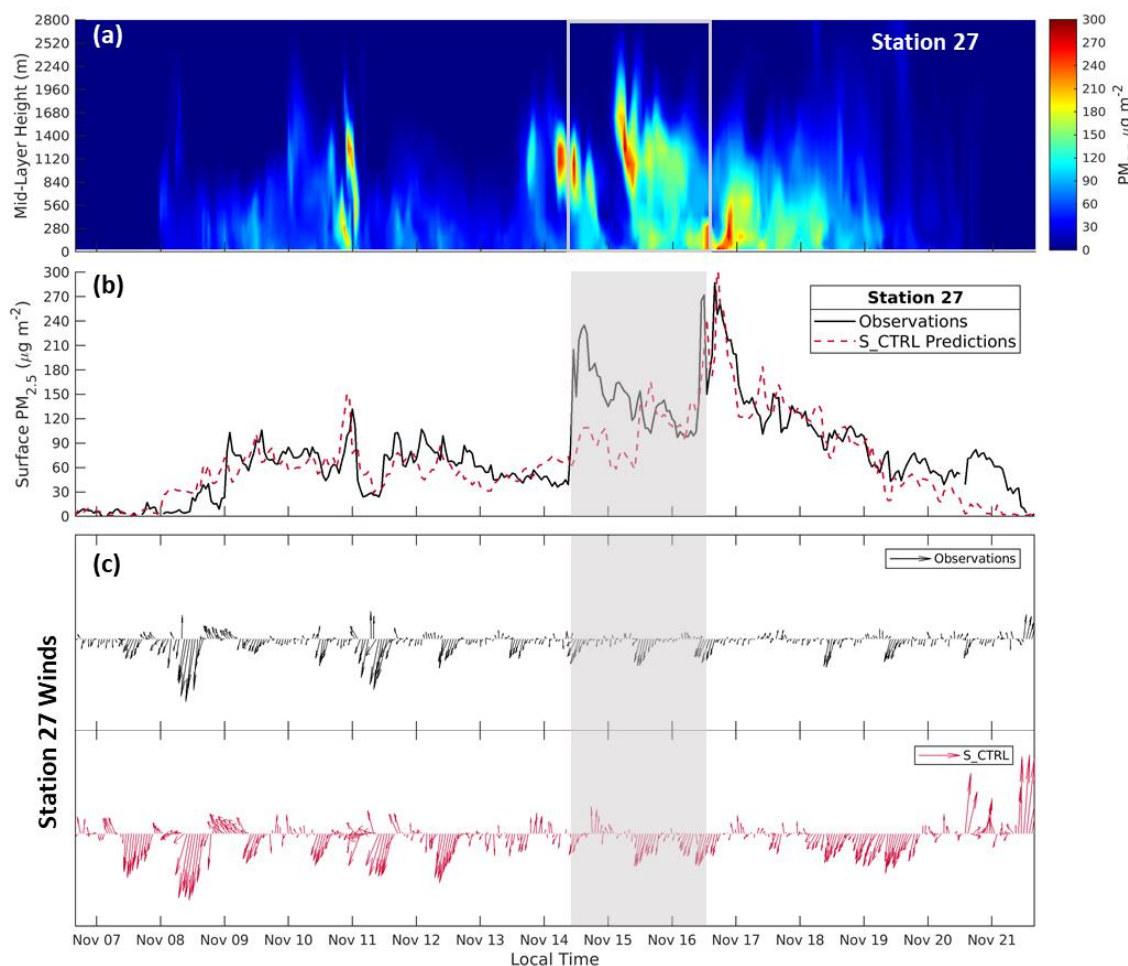

Figure 4.9. Vertical profile of PM$_{2.5}$ (a), time series of surface PM$_{2.5}$ (b), winds (c; observations in black and predictions in red) at Station 27 in the Bay Area. The gray box highlights the timeframe of greatest model bias of surface PM$_{2.5}$. Sharp increases in PM$_{2.5}$ correlate with a switch to northeasterly winds that import fire emissions to the Bay Area. Large negative PM$_{2.5}$ bias on 15 November occurs when S_CTRL deviates from observations and produces southerly winds which bring in clean air. This can be seen with the column of low level of PM on 15 November in (a).
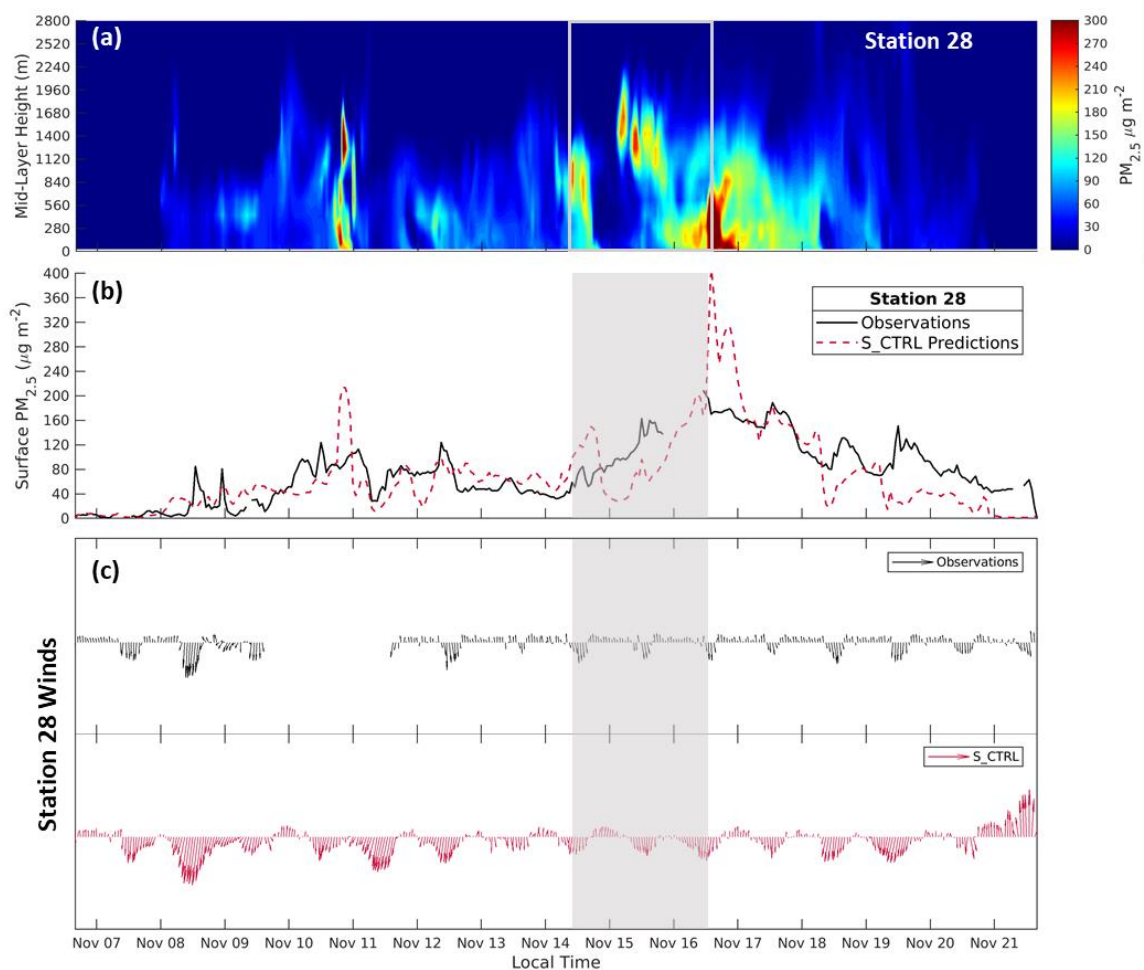
Figure 4.10. Vertical profile of PM$_{2.5}$ (a), time series of surface PM$_{2.5}$ (b), winds (c; observations in black and predictions in red) at Station 28 in the Bay Area. This station experienced different wind and PM evolution compared to Station 27 in Figure 4.10. The gray shading highlights the timeframe of greatest model bias of surface PM$_{2.5}$. Sharp increases in PM$_{2.5}$ correlate with a switch to northerly winds that import emissions to the Bay Area. Large negative PM$_{2.5}$ bias on 15 November occurs when S_CTRL deviates from observations and produces stronger southerly winds. This can be seen with the column of reduced particulate matter on 15 November in (a).
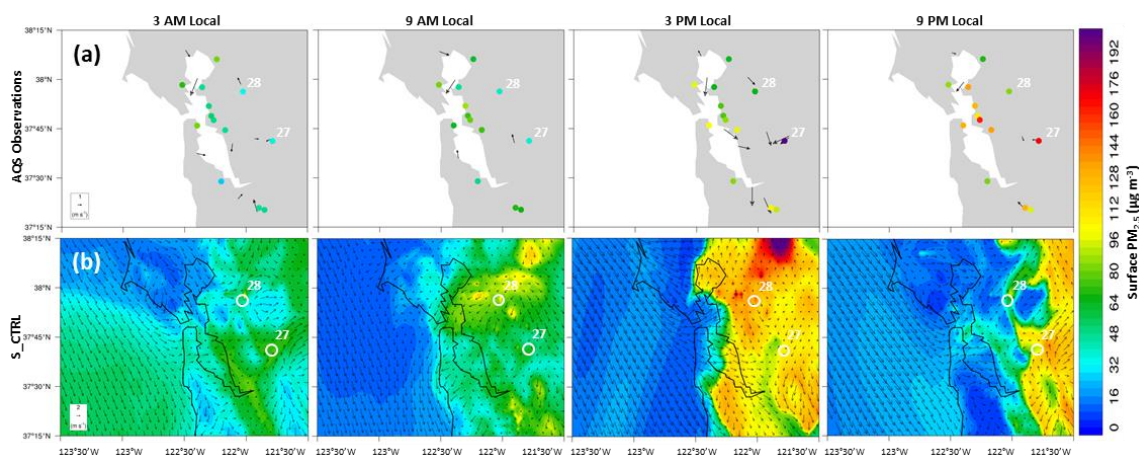
Figure 4.11. Surface PM$_{2.5}$ and wind field on 14 November in the Bay Area of observations (a) and S_CTRL predictions (b). Note that the reference wind vector for S_CTRL is 2 m s^{-1} while the reference is 1 m s^{-1} for observations. While the plume encroaches on the Bay Area, a strong sea breeze develops midday, driving plumes back inland. This sea breeze is not present in observational data, leading to a large underprediction of surface PM$_{2.5}$.

4.3.3 Aerosol Vertical Profile

The TROPOMI ALH retrieval represents vertically localized aerosol layers within the free troposphere in cloud-free conditions and is designed to capture aerosol layers produced by biomass burning aerosol (such as wildfires), volcanic ash, and desert dust (Apituley et al., 2019). ALH is retrieved based on the significant effect of aerosol vertical structure on the high spectral resolution observations in the O$_2$-A band in the near-infrared (759 to 770 nm). The ALH algorithm includes a spectral fit estimation of reflectance across the O$_2$ A band using the Optimal Estimation retrieval method with primary fit parameters of aerosol layer mid pressure and aerosol optical thickness (de Graaf et al., 2019). The assumed aerosol profile is a single uniform scattering layer with a fixed pressure thickness, constant aerosol volume extinction coefficient, and constant aerosol single scatter albedo. The mid pressure of the layer, defined as the average of the top and bottom pressures, is converted to altitude with a temperature profile. This parameterization is best suited for aerosol profiles dominated by a sole elevated and optically thick aerosol layer, which is characteristic of wildfire plumes. We compare the satellite-derived aerosol layer height to WRF-Chem predictions of PM$_{2.5}$ using two methods. We define the smoke aerosol layer with a PM$_{2.5}$ threshold concentration of 3 µg m^{-3}. For the first method, the layer height is calculated as the average of heights at which PM$_{2.5}$ is greater than the threshold. For the second method, these heights are weighted

by BC mass. Figure 4.13 shows the satellite-derived layer height (a) and the S_CTRL model bias of average heights (b) and mass weighted average heights (c). TROPOMI layer heights are generally 1 to 2 km and reach greater than 6 km in some instances. Using purely averaged heights, S_CTRL typically overpredicts ALH by 100 to 400 m and remains within a smaller range than TROPOMI. S_CTRL layer heights weighted by BC mass are lower, thus improving agreement with the satellite. Archer-Nicholls et al. (2015) and Sessions et al. (2011) also reported overpredicted aerosol layer heights using WRF-Chem when compared to airborne data and Multi-angle Imaging Spectro Radiometer MISR stereo heights, respectively. Using CMAQ, however, Herron-Thorpe et al. (2014) reported underpredicted heights when compared to Cloud-Aerosol Lidar with Orthogonal Polarization CALIOP products. Archer-Nicholls et al. (2015) found that error in plume injection height can contribute to error in surface PM, and that PM biases were dependent on vegetation type as carbon-density and heat release vary by vegetation. Location of the aerosol layer within the column likely also contributes to error in surface predictions of $PM_{2.5}$ in this study, however, the current analysis is inconclusive. The assumption of a single, elevated aerosol layer used in the TROPOMI ALH derivation may not be characteristic of the vertical structure predicted by WRF-Chem. As seen in Fig. 4.10 and 11 and in the vertical profile near the wildfire, layers of aerosol are commonly present at the surface and exist as multiple nonlocalized layers. Sessions et al. (2011) also found that using the FLAMBE fire data preprocessor with emission injection heights not constrained to the boundary layer resulted in better agreement with satellite products than PREP-CHEM-SRC. Consideration of the WRF vertical grid is also necessary when comparing surface level values. Further development of the analytic method used to evaluate WRF-Chem aerosol layer heights may provide insight into the behavior of the plume rise model and its vertical structure.
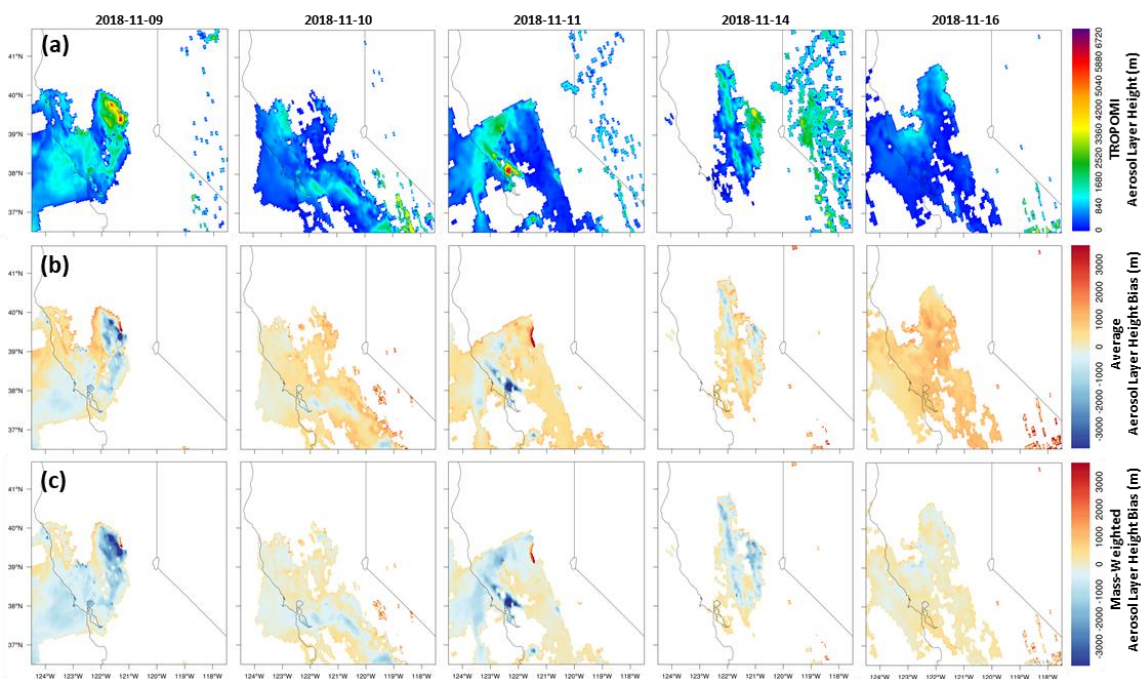
Figure 4.13. Comparison of TROPOMI aerosol layer height (a) and bias where S_CTRL layer height is calculated as the average of heights where $PM_{2.5} > 3 \ \mu g \ m^{-3}$ (b) and the average weighted by $PM_{2.5}$ mass (c) for select days at 13:30 local time. In panels b and c, warm colors indicate positive bias where S_CTRL overpredicts the height of the aerosol layer.

4.4 Sensitivity Simulation Analysis

We conduct sensitivity simulations to investigate the effects of various parameters on the ability of the WRF-Chem model to accurately predict downwind PM concentrations from wildfires. As meteorological conditions and related boundary structure play important roles in plume dynamics and the transport of PM, we separately test the aerosol feedback to meteorology and the land surface model. To understand the extent to which fire characteristics provided by satellite data can affect the simulation, we analyze the fire product sources (VIIRS versus FINN), the total fire emissions, and the division between smoldering versus flaming phase emissions. To examine the influence of the plume rise model, we perturb a key parameter, the entrainment coefficient.

4.4.1 Aerosol Radiative Feedback to Meteorology

By absorbing and scattering solar radiation, aerosols can impact the radiative fluxes, cloud formation, and precipitation in the atmosphere (Wang et al., 2016; 2020), and, in turn, the

meteorological conditions for aerosol formation, transport, and removal (Li et al., 2019). WRF-Chem has the option to couple aerosol-radiative direct effects with meteorology simulation. S_NOAERO uses the same input data and configuration as S_CTRL, but disables the aerosol radiative feedback. Figure 4.14 shows the evolution of surface wind speed and temperature throughout the wildfire near the source (a), in Sacramento (b), and in the Bay Area (c). The aerosol radiative impact on simulated meteorology is more pronounced for surface temperature than wind. When aerosol radiative feedbacks are noticeable, colder temperatures and calmer winds are found near the surface. Generally, feedbacks are more evident in the region closer to the fire sources with larger PM concentrations. Also, in the Bay Area, the largest changes in meteorology coincide with the largest differences in surface $PM_{2.5}$ between the two scenarios (Fig. 4.14), which occurs when higher concentrations are predicted (10-11 November, 14-16 November). Consequently, the aerosol radiative feedback in WRF-Chem acts to stabilize the atmosphere, presumably due to the solar absorption by smoke aerosols and reduction of radiation reaching the surface (Wang et al., 2013). When taking the entire time period into account, the overall aerosol effect on meteorology is relatively small in the downwind region, like the Bay Area, even when aerosol concentrations are high.
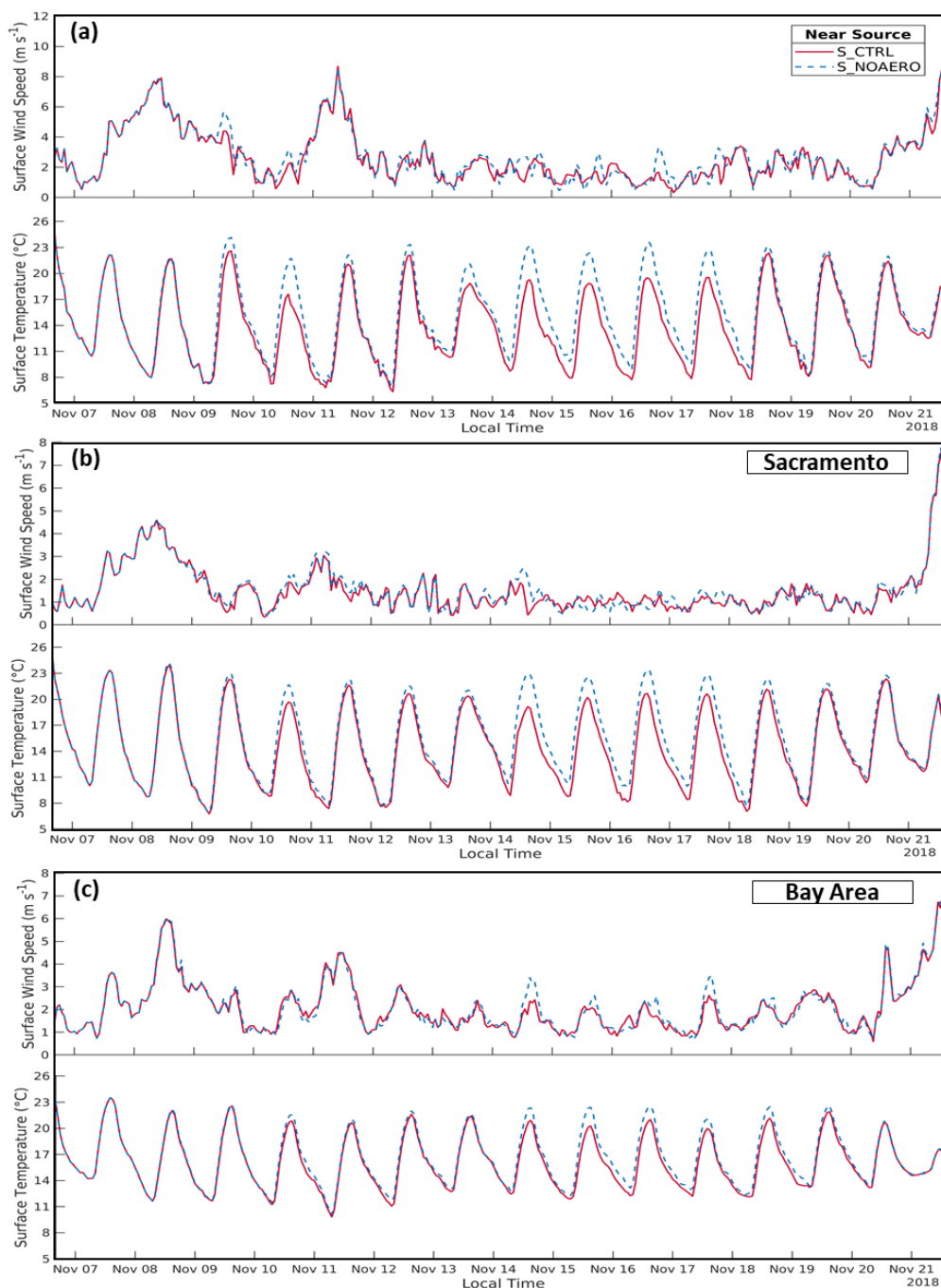
Figure 4.14. Comparison of meteorology generated by S_CTRL (solid red) and S_NOAERO (in which aerosol effects do not feed back to the meteorology, dashed blue) over the three areas of study: a) near the wildfire, b) Sacramento, and c) the San Francisco Bay Area. Exclusion of the aerosol feedback has the greatest effect nearest the fire, where S_NOAERO increased wind and temperature by 9.8% and 9.7%, respectively, on average. The aerosol feedback mechanism has the least significance in the Bay Area, where S_NOAERO wind speed differs less than 2% and temperature differs 3.1% on average. The most pronounced changes occur during 14-16 November when S_CTRL significantly underpredicts surface PM$_{2.5}$. In WRF-Chem, the feedback of aerosol-radiation interactions on meteorology act to stabilize the atmosphere, slow wind speeds, and increase PM concentrations.

4.4.2 Fire Emission Inventory

WRF-Chem input fire files produced with VIIRS and PREP-CHEM-SRC include fire size, smoldering emission flux, and flaming factor. Here, we test the sensitivity of predictions to FINN (S_FINN) versus VIIRS/MODIS, as well as the smoldering emission flux (S_EMRAW) and flaming factor (S_FCTX2). S_FINN produces very little aerosol, though it captures the timing of some peaks. The aerosol underestimation may be a result of bias in the emission inventory or an issue of its implementation in the plume rise model code, as FINN specifies total wildfire emissions rather than a smoldering and flaming distribution. When VIIRS emission inventory is used, the total wildfire emission flux can be altered through two parameters: the smoldering emission flux at the surface and the flaming factor. Directly increasing the smoldering emission flux adds emissions to the surface layer and increases flaming phase emissions proportionally. Figure 4.15 shows the impact of doubling smoldering emissions on 13 November and tripling them during 14-16 November. These changes to the inventory more than double concentrations of surface $PM_{2.5}$ in the area of the wildfire and increase concentrations in the Bay Area by 20 to 60 μg m^{-3} during 14-16 November. Consequently, increasing input of total wildfire emissions improves the agreement of predictions with observations in Sacramento and the Bay Area, suggesting that some uncertainty may stem from satellite fire products. This finding is supported by Archer-Nicholls et al. (2015), as they applied a factor of 5 to scale up the wildfire emissions in their simulations. By modifying the flaming factor, we perturb only the emissions injected aloft by the plume, as emissions higher in the atmosphere may allow for greater transport downwind. By doubling the flaming factor over the full simulation duration, S_FCTX2 recovers 10-35 μg m^{-3} in the Bay Area 14-16 November (Fig. 4.14c), when S_CTRL substantially underpredicts $PM_{2.5}$.
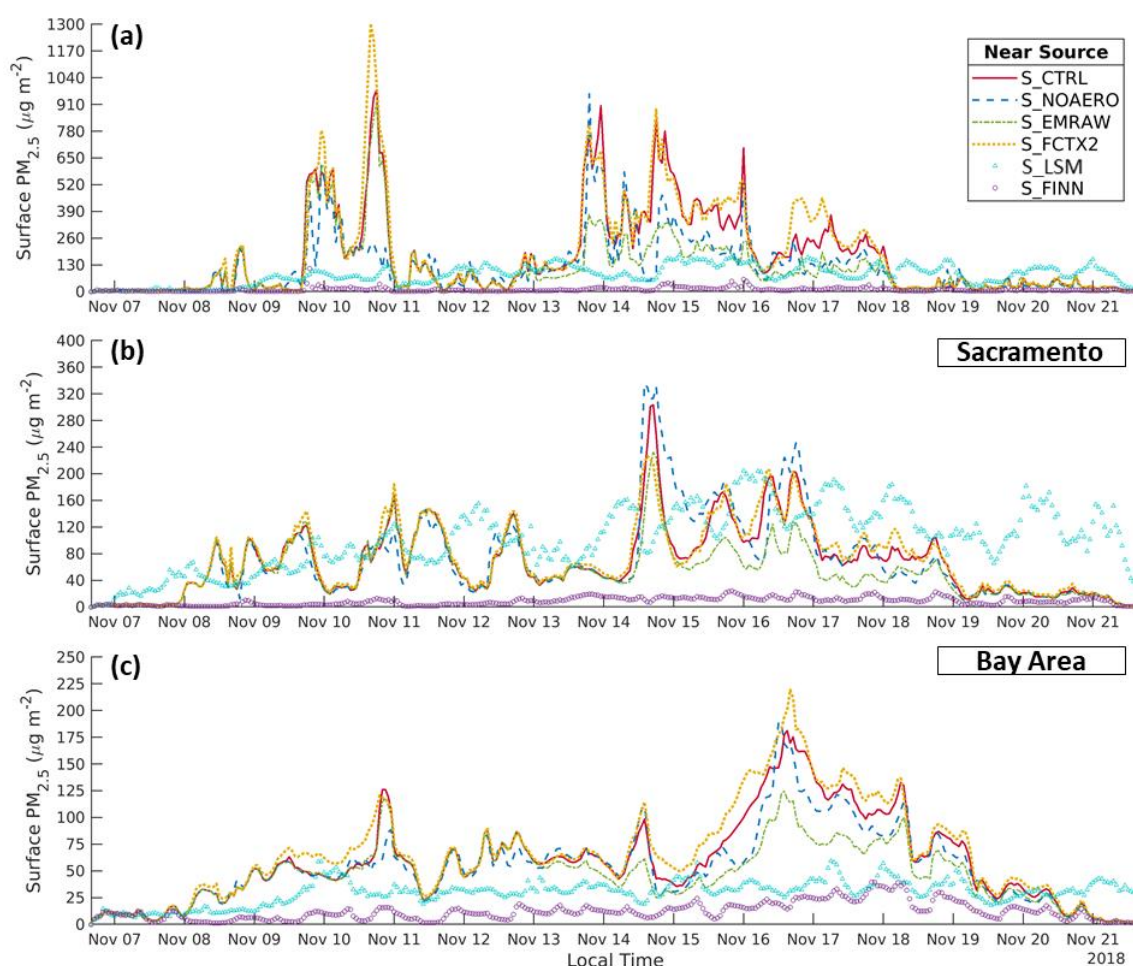
Figure 4.15. Time series of surface PM$_{2.5}$ (μg m^{-3}) predicted by the sensitivity simulations (Table 4.1) averaged for the three areas of study: a) near the wildfire (N = 5), b) Sacramento (N = 7), and c) the Bay Area (N = 13). S_ENTR is omitted from the figure as it resulted in less than 1% change from S_CTRL. In the Bay Area, S_FCTX2 generally predicted more surface PM$_{2.5}$, recovering 10-35 μg m^{-3} 14-16 November when S_CTRL significantly underpredicts PM$_{2.5}$ compared to observations. S_EMRAW demonstrates the impact of increasing the emissions inventory for 13-16 November. In the Bay Area, using the unperturbed emissions inventory reduces PM$_{2.5}$ by more than 30% over 14-16 November. The impact of the aerosol feedback mechanism on PM$_{2.5}$ (S_NOAERO) is location dependent. Excluding the feedback to meteorology generally reduces PM$_{2.5}$ near the wildfire and in the Bay Area, while increasing PM$_{2.5}$ in Sacramento. Employing the ACM2 PBL scheme results in a vastly different temporal evolution with a distinct diurnal pattern (S_LSM). FINN input fire data produces very little PM$_{2.5}$.

4.4.3 Plume Rise Parameterization – Entrainment Coefficient

The plume rise model parameterizes entrainment as proportional to the plume vertical velocity and inversely proportional to the plume radius (Freitas et al., 2010). Greater entrainment causes rapid cooling, such that near surface plume temperatures are only slightly

warmer than the environment, lowering buoyancy and reducing the plume height. Larger wildfires generate less entrainment and reach higher injection heights. The parameterization also includes the effect of horizontal winds on entrainment. Strong wind shear can enhance entrainment and increase boundary layer mixing (Freitas et al., 2010). Archer-Nicholls et al. (2015) decreased the original entrainment coefficient (Freitas et al., 2007) from 0.1 to 0.05 to improve their simulations of a wildfire. As the Camp Fire developed rapidly and intensely, we performed the sensitivity simulation S_ENTR with a lower entrainment coefficient of 0.02 to allow for higher injection heights. However, entrainment perturbation resulted in less than 1% change in surface $PM_{2.5}$ from S_CTRL. A possible reason is that the background winds were quite strong already, for which the entrainment coefficient played a limited role. We compare simulations using two different land surface models (LSM) which include the PBL schemes: the Noah LSM with Mellor-Yamada-Janjic (MYJ) PBL and the Pleim-Xiu LSM (referred to here as P-X) with the Asymmetric Convection Model 2 (ACM2) PBL (Janjic, 1994; Pleim and Xiu, 1995; Chen & Dudhia, 2001; Pleim, 2007). Land surface models simulate the heat and radiative fluxes between the ground and the atmosphere (Campbell et al., 2018). Noah LSM has four soil moisture and temperature layers, while the Pleim-Xiu LSM has two (Hu et al, 2014; Campbell et al., 2018). Both include a vegetation canopy model and vegetative evapotranspiration. The PBL scheme provides the boundary layer fluxes (heat, moisture, and momentum) and the vertical diffusion within the column. It uses boundary layer eddy fluxes to distribute surface fluxes and grows the PBL by entrainment. A key feature of PBL schemes is the inclusion of local mixing (between adjacent layers) and/or nonlocal mixing (from the surface layer to higher layers). The MYJ scheme is a turbulent kinetic energy prediction, while the ACM2 scheme is a member of the diagnostic non-local class. MYJ solves for the total kinetic energy in each column from buoyancy and shear production, dissipation, and vertical mixing. ACM2 has two main components: a term for local transport by small eddies and a term for nonlocal transport by large eddies. Coniglio et al. (2013) showed that the MYJ scheme can undermix the PBL in locations upstream of convection in the presence of overly cool and moist conditions near the ground in the daytime, whereas ACM2 can result in an excessively deep PBL in evening.

Pleim (AMS, 2007) also noted that ACM2 predicts the PBL profile of potential temperature and velocity with greater accuracy.

The use of P-X and ACM2 results in substantially different aerosol trends and plume evolution, the effects of which are largely location-dependent (Fig. 4.15). Near the fire and in the Bay Area, S_LSM produces little similarity in surface $PM_{2.5}$ magnitude and trend as compared to S_CTRL. S_LSM reduces $PM_{2.5}$ concentrations by more than 50% in both areas for the majority of the simulation period. However, S_CTRL overpredicts $PM_{2.5}$ near the wildfire, while S_LSM underpredicts but produces a more muted temporal pattern, similar to observations. In the Sacramento area, S_LSM generally predicts higher $PM_{2.5}$ values with a distinct diurnal trend. Peaks are of similar magnitude to S_CTRL, but displaced temporally. The topography of the Sacramento area is more uniform than the complex terrain of the Bay area as well as the foothills and canyons near the wildfire, likely contributing to the distinctions in the behavior of the two schemes. Moreover, the current sensitivity study stresses the importance of the parameterization of the land surface and the boundary layer. As shown here, the Noah LSM and MYJ scheme performs well for the broader region of northern California, whereas improvement near the wildfire itself may be attained with altered PBL parameterization.

4.5 Conclusions and Discussion

The record-breaking Camp Fire ravaged northern California for nearly two weeks. At a distance of 240 km downwind of the wildfire, Bay Area surface $PM_{2.5}$ levels reached nearly 200 µg m^{-3} and remained over 70 µg m^{-3} over 7-22 November 2018. It is uncertain to what extent the current chemical transport models can reproduce the key features of this historical event. Here, we employ the WRF-Chem model to characterize the spatio-temporal PM concentrations across northern California and to investigate the sensitivity of predictions to key parameters of the model. The model utilizes satellite fire detection products with a resolution of 375 m and a biomass burning model to generate the fire emission inventory at near real time. We conduct model simulations at 2 km resolution. A wide range of observational data is employed to evaluate the model performance, including ground-based

observations of $PM_{2.5}$, black carbon, and meteorology from EPA and NOAA stations, as well as satellite measurements, such as Tropospheric Monitoring Instrument (TROPOMI) aerosol layer height and aerosol index.

We focus on three geographic areas: the vicinity of the wildfire, Sacramento, and the San Francisco Bay Area. The control experiment was able to simulate the general transport and extent of the plume as well as the magnitude and temporal evolution of surface $PM_{2.5}$ in Sacramento and the Bay Area. Meanwhile, the control experiment substantially overpredicted surface $PM_{2.5}$ near the fire, but captured the general evolution of the fire development. On the Pacific coast, the Bay Area was subject to significant sea breezes not observed during the time period of simulation. Owing to strong winds predicted from the ocean, a large negative bias existed in surface $PM_{2.5}$. Increasing total wildfire emissions (smoldering + flaming) and increasing flaming phase emissions alone each recovered some $PM_{2.5}$ biases. Aerosol radiative feedback on meteorology acted to stabilize the atmosphere and slightly increased the $PM_{2.5}$ concentration near the surface during most severe episodes. Hence, its inclusion modestly improves model performance. Our study shows that sources of downwind PM error stem primarily from the localized structure of the plume and uncertainty in fire emissions. Uncertainty of partitioning between smoldering and flaming phases may also contribute to uncertainty in plume horizontal transport.

The recent TROPOMI aerosol layer height product shows promise as an analytical tool, but requires further development of the method by which it can be directly compared to WRF-Chem. Herron-Thorpe et al. (2014) noted that careful consideration must also be given to the vertical coordinates across models and satellite products, as discrepancies in reporting heights in reference to sea level, ground level, or the geoid can influence analyses. Additional verification of input fire data sources, such as FINN, and their implementation in the WRF-Chem plume rise model is needed for studies of the vertical structure. Deeper understanding of the role of plume dynamics and boundary layer parameterization on aerosol concentrations downwind from wildfires will inform updates to forecast models like WRF-SFIRE-CHEM, which couples WRF with a fire spread model and smoke dispersion simulation (Barbunzo 2019; Kochanski et al., 2013).

References

Andreae, M. O., and Merlet, P.: Emission of trace gases and aerosols from biomass burning. Global Biogeochemical Cycles, 15(4), 955–966, https://doi.org/10.1029/2000GB001382, 2001.

Apituley, A., Pedergnana, M., Sneep, M., Pepijn Veefkind, J., Loyola, D., Landgraf, J., and Borsdorff, T.: Sentinel-5 precursor/TROPOMI Level 2 Product User Manual Carbon Monoxide, SRON-S5P-LEV2-MA-002, http://www.tropomi.eu/sites/default/files/files/Sentinel-5P-Level-2-Product-User-Manual-Carbon-Monoxide_v1.00.02_20180613.pdf, 2018.

Apituley, A., Pedergnana, M., Sneep, M., Pepijn Veefkind, J., Loyola, D., Sanders, B., de Graaf, M.: Sentinel-5 precursor/TROPOMI Level 2 Product User Manual Aerosol Layer Height, S5P-KNMI-L2-0022-MA, http://www.tropomi.eu/sites/default/files/files/publicS5P-KNMI-L2-0022-MA-Product_User_Manual_for_the_Sentinel_5_precursor_Aerosol_layer_height-1.3.2-20190926_signed.pdf, 2019.

Archer-Nicholls, S., Lowe, D., Darbyshire, E., Morgan, W.T., Bela, M.M., Pereira, G., Trembath, J., Kaiser, J.W., Longo, K.M., Freitas, S.R., Coe, H., and McFiggans, G.: Characterising Brazilian biomass burning emissiongs using WRF-Chem with MOSAIC sectional aerosol. Geosci. Model Dev., 8, 549-577, https://doi.org/10.5194/gmd-8-549-2015, 2015.

Barbuzano, J.: Wildfire smoke traps itself in valleys, Eos, 100, https://doi.org/10.1029/2019EO135955, 2019.

Brown, T., Leach, S., Wachter, B., Gardunio, B.: The Northern California 2018 Extreme Fire Season [in "Explaining Extremes of 2018 from a Climate Perspective"]. Bull. Amer. Meteor. Soc., 101 (1), S1–S4, https://doi.org/10.1175/BAMS-D-19-0275.1, 2020.

Campbell, P.C., Bash, J.O., Spero, T.L.: Updates to the Noah land surface model in WRF-CMAQ to improve simulated meteorology, air quality, and deposition. Journal of Advances in Modeling Earth Systems, 11(1), 231-256, https://doi.org/ 10.1029/2018MS001422, 2018.

Cascio, W. E.: Wildland fire smoke and human health, Science of the Total Environment, 624, 586-595, https://.doi.org/10.1016/j.scitotenv.2017.12.086, 2018.

Chen, F., and J. Dudhia, 2001: Coupling an advanced land surface-hydrology model with the Penn State-NCAR MM5 modeling system, part I, model implementation and sensitivity. Mon. Wea. Rev., 129. 586-585.

Copernicus Climate Change Service (C3S): ERA5: Fifth generation of ECMWF atmospheric reanalyses of the global climate. Copernicus Climate Change Service Climate Data Store (CDS), https://cds.climate.copernicus.eu/cdsapp#!/home, last access: 22 May 2020, 2017.

Copernicus Sentinel data processed by ESA, Koninklijk Nederlands Meteorologisch Instituut (KNMI), Sentinel-5P TROPOMI Aerosol Index 1-Orbit L2 7km x 3.5km,

Greenbelt, MD, USA, Goddard Earth Sciences Data and Information Services Center (GES DISC), https://doi.org/10.5270/S5P-0wafvaf. 2018.

Copernicus Sentinel data processed by ESA, Koninklijk Nederlands Meteorologisch Instituut (KNMI), Sentinel-5P TROPOMI Aerosol Layer Height 1-Orbit L2 7km x 3.5km, Greenbelt, MD, USA, Goddard Earth Sciences Data and Information Services Center (GES DISC), https://doi.org/10.5270/S5P-j7aj4gr, 2019.

Copernicus Sentinel data processed by ESA, Koninklijk Nederlands Meteorologisch Instituut (KNMI)/Netherlands Institute for Space Research (SRON), Sentinel-5P TROPOMI Carbon Monoxide CO Column 1-Orbit L2 7km x 7km, Greenbelt, MD, USA, Goddard Earth Sciences Data and Information Services Center (GES DISC), https://doi.org/10.5270/S5P-1hkp7rp, 2018.

De Graaf, M., de Haan, J.F., and Sanders, A.F.J.: TROPOMI ATBD of the Aerosol Layer Height, S5P-KNMI-L2-0006-RP, http://www.tropomi.eu/sites/default/files/files/publicSentinel-5P-TROPOMI-ATBD-Aerosol-Height.pdf, 2019.

Dudhia, J.: Numerical study of convection observed during the Winter Monsoon Experiment using a mesoscale two–dimensional model, J. Atmos. Sci., 46, 3077–3107, https://doi.org/10.1175/1520-0469(1989)046<3077:NSOCOD>2.0.CO;2, 1989.

Emmons, L. K., Walters, S., Hess, P. G., Lamarque, J.-F., Pfister, G. G., Fillmore, D., Granier, C., Guenther, A., Kinnison, D., Laepple, T., Orlando, J., Tie, X., Tyndall, G., Wiedinmyer, C., Baughcum, S. L., and Kloster, S.: Description and evaluation of the Model for Ozone and Related chemical Tracers, version 4 (MOZART-4), Geosci. Model Dev., 3, 43-67, https://doi.org/10.5194/gmd-3-43-2010, 2010.

Freitas, S. R., Longo, K. M., Chatfield, R., Latham, D., Dias, M., Andreae, M. O., Prins, E., Santos, J. C., Gielow, R., and Carvalho, J. A.: Including the sub-grid scale plume rise of vegetation fires in low resolution atmospheric transport models, Atmos. Chem. Phys., 7(13), 3385–3398. https://doi.org/10.5194/acp-7-3385-2007, 2007.

Freitas, S. R., Longo, K. M., Trentmann, J., and Latham, D.: Technical note: Sensitivity of 1-D smoke plume rise models to the inclusion of environmental wind drag, Atmos. Chem. Phys., 10(2), 585–594. https://doi.org/10.5194/acp-10-585-2010, 2010.

Freitas, S. R., Longo, K. M., Alonso, M. F., Pirre, M., Marecal, V., Grell, G., Stockler, R., Mello, R. F., and Sánchez Gácita, M.: PREP-CHEM-SRC – 1.0: a preprocessor of trace gas and aerosol emission fields for regional and global atmospheric chemistry models, Geosci. Model Dev., 4, 419–433, https://doi.org/10.5194/gmd-4-419-2011, 2011.

Guenther, A., Karl, T., Harley, P., Wiedinmyer, C., Palmer, P.I., and Geron, C.: Estimates of global terrestrial isoprene emissions using MEGAN (Model of Emissions of Gases and Aerosols from Nature), Atmos. Chem. Phys., 6, 3181-3210, https://doi.org/10.5194/acp-6-3181-2006, 2006.

Herron-Thorpe, F. L., Mount, G. H., Emmons, L. K., Lamb, B. K., Jaffe, D. A., Wigder, N. L., Chung, S.H., Zhang, R., Woelfe, M.D., and Vaughan, J.K.: Air quality simulations of wildfires in the Pacific Northwest evaluated with surface and satellite observations during the summers of 2007 and 2008. Atmos. Chem. Phys., 14(22), 12,533–12,551. https://doi.org/10.5194/acp-14-12533-2014, 2014.

Houghton, R., Lawrence, K., Hackler, J., and Brown, S.: The spatial distribution of forest biomass in the Brazilian Amazon: A comparison of estimates, Global Change Biology, 7(7), 731–746. https://doi.org/10.1046/j.1365-2486.2001.00426.x, 2001.

Hu, Z., Zhong-Feng, X., Ning-Feng, Z., Ma, Z., Guo-Ping, L.: Evaluation of the WRF model with different land surface schemes: a drought event simulation in southwest China during 2009-10. Atmospheric and Oceanic Science Letters, 7(2) 168-173, doi: 10.3878/j.issn.1674-2834.13.007, 2014.

Janjic, Zavisa I.: The Step–Mountain Eta Coordinate Model: Further developments of the convection, viscous sublayer, and turbulence closure schemes, Mon. Wea. Rev., 122, 927–945, https://doi.org/10.1175/1520-0493(1994)122<0927:TSMECM>2.0.CO;2, 1994.

Janjic, Z. I.,: Nonsingular implementation of the Mellor-Yamada Level 2.5 Scheme in the NCEP Meso model. NCEP Office Note No. 437, 61 pp., 2002.

Jin Q., Wei Z.-L., Yang B., Huang J.: Consistent response of Indian summer monsoon to Middle East dust in observations and simulations, Atmos. Chem. Phys., 15, 9897-9915 https://doi.org/10.5194/acp-15-9897-2015, 2015.

Li, Z., et al., East Asian Study of Tropospheric Aerosols and Impact on Regional Cloud, Precipitation, and Climate (EAST-AIRCPC), J. Geophys. Res. 124 (23) 13026-13054, 2019.

Longo, K. M., Freitas, S. R., Andreae, M. O., Setzer, A., Prins, E., and Artaxo, P.: The Coupled Aerosol and Tracer Transport model to the Brazilian developments on the Regional Atmospheric Modeling System (CATT-BRAMS)—Part 2: Model sensitivity to the biomass burning. Atmospheric Chemistry and Physics, 10(13), 5785–5795. https://doi.org/10.5194/acp-10-5785-2010, 2010.

Kahn, R. (2020), A global perspective on wildfires, Eos, 101, https://doi.org/10.1029/2020EO138260, 2020.

Kochanski, A., Beezley, D., Mandel, J., Clements, B.: Air pollution forecasting by coupled atmosphere-fire model WRF and SFIRE with WRF-Chem. ArXiv: 1304.7703 [physics.ao-ph], 2013.

Mlawer, E.J., Taubman, S.J., Brown, P.D., Iacono, M.J. and Clough, S.A.: Radiative transfer for inhomogeneous atmospheres: RRTM, a validated correlated–k model for the longwave, J. Geophys. Res., 102, 16663–16682, https://doi.org/10.1029/97JD00237, 1997.

Olson, J., Watts, J., and Allison, L.: Major world ecosystem complexes ranked by carbon in live vegetation: A database, Oak Ridge National Laboratory, Oak Ridge, Tennessee, USA. 2000.

Pimlott, K., Laird, J., and Brown, E.G.: 2015 Wildfire Activity Statistics. California Department of Forestry and Fire Protection. Available at: https://www.fire.ca.gov/media/10061/2015_redbook_final.pdf.

Pleim, Jonathan E.: A Combined Local and Nonlocal Closure Model for the Atmospheric Boundary Layer. Part I: Model Description and Testing, J. Appl. Meteor. Climatol., 46, 1383–1395. doi:10.1175/JAM2539.1, 2007.

Pleim, J., A. and Xiu.: Development and testing of a surface flux and planetary boundary layer model for application in mesoscale models. Journal of Applied Meteorology, 34, 16-34, https://doi.org/10.1175/1520-0450-34.1.16, 1995.

Sessions, W.R., Fuelberg, H.E., Kahn, R.A., and Winker, D.M.: An investigation of methods for injecting emissions from boreal wildfires using WRF-Chem during ARCTAS. Atmos. Chem. Phys., 11, 5719-5744, https://doi.org/ 10.5194/acp-11-5719-2011, 2011.

Shao, Y., Ishizuka, M., Mikami, M., and Leys, J.: Parameterization of size-resolved dust emission and validation with measurements, J. Geophys. Res. Atmos., 116, D08203, doi:10.1029/2010JD014527, 2011.

Shi, H., Jiang, Z., Zhao, B., Li, Z., Chen, Y., Gu, Y., Jiang, J.H., Lee, M., Liou, K.N., Neu, J., Payne, V., Su, H., Wang, Y., Marcin, W., and Worden, J.: Modeling study of the air quality impact of record-breaking Southern California wildfires in December 2017. Journal of Geophysical Research: Atmospheres, 124. https://doi.org/10.1029/2019JD030472, 2019.

Schneising, O., Buchwitz, M., Reuter, M., Bovensmann, H., and Burrows, J. P.: Severe Californian wildfires in November 2018 observed from space: the carbon monoxide perspective, Atmos. Chem. Phys., 20, 3317–3332, https://doi.org/10.5194/acp-20-3317-2020, 2020.

Strahler, A., Muchoney, D., Borak, J., Friedl, M., Gopal, S., Lambin, E., & Moody, A.: MODIS Land Cover Product Algorithm Theoretical Basis Document (ATBD). Version 5.0, available at https://modis.gsfc.nasa.gov/data/atbd/atbd_mod12.pdf, 1999.

Stein Zweers, D.: TROPOMI ATBD of the UV aerosol index, S5P-KNMI-L2-0008-RP, available at http://www.tropomi.eu/sites/default/files/files/S5P-KNMI-L2-0008-RP-TROPOMI_ATBD_UVAI-1.1.0-20180615_signed.pdf, 2018.

Tewari, M., Chen, F., Wang, W., Dudhia, J., LeMone, M.A., Mitchell, K., Ek, M., Gayno, G, Wegiel, J., and Cuenca, R.H.: Implementation and verification of the unified NOAH land surface model in the WRF model. 20th conference on weather analysis and forecasting/16th conference on numerical weather prediction, pp. 11–15. 2004.

University Corporation for Atmospheric Research: MOZART DOWNLOAD. https://www.acom.ucar.edu/wrf-chem/mozart.shtml, 2018.

US Environmental Protection Agency: Air Quality System Data Mart [internet database] available via https://www.epa.gov/airdata, last access: 17 May 2020.

US Environmental Protection Agency: National Emissions Inventory (NEI). https://www.epa.gov/air-emissions-inventories/national-emissions-inventory-nei, 2018.

Wang, Y., Le, T., Chen, G., Yung, Y.L., Su, H., Seinfeld, J.H., Jiang, J.H.: Reduced European aerosol emissions suppress winter extremes over northern Eurasia, Nat. Climate Change, 10, 225–230, https://doi.org/10.1038/s41558-020-0693-4, 2020.

Wang, Y., Ma, P.-L., Jiang, J., Su, H., and Rasch, P.: Towards Reconciling the Influence of Atmospheric Aerosols and Greenhouse Gases on Light Precipitation Changes in Eastern China, J. Geophys. Res. Atmos. 121(10), 5878–5887, https://doi.org/10.1002/2016JD024845, 2016.

Wang, Y., Khalizov. A., Levy, M., and Zhang, R.: New Directions: Light Absorbing Aerosols and Their Atmospheric Impacts, Atmos. Environ., 81, 713-715, https://doi.org/10.1016/j.atmosenv.2013.09.034, 2013.

Ward, D., Susott, R., Kauffman, J., Babbitt, R., Cummings, D., Dias, B., Holben, B.N., Kaufman, Y.J., Rasmussen, R.A., and Setzer, A.W.: Smoke and fire characteristics for cerrado and deforestation burns in Brazil: BASE-B experiment. J. Geophys. Res., 97(D13), 14,601–14,619. https://doi.org/10.1029/92JD01218, 1992.

Wiedinmyer, C., Akagi, S. K., Yokelson, R. J., Emmons, L. K., Al-Saadi, J. A., Orlando, J. J., and Soja, A. J.: The Fire INventory from NCAR (FINN): A high resolution global model to estimate the emissions from open burning. Geoscientific Model Development, 4(3), 625–641. https://doi.org/10.5194/gmd-4-625-2011, 2011.

WRAP (Western Regional Air Partnership): 2002 Fire Emission Inventory for the WRAP Region- Phase II, Project No. 178-6, available at: http://www.wrapair.org/forums/fejf/tasks/FEJFtask7PhaseII.html, 2005.

Zhao, C., Liu, X., Leung, L., and Hagos, S.: Radiative impact of mineral dust on monsoon precipitation variability over West Africa. Atmos Chem. Phys., 11, 1879-1893, https://doi.org/10.5194/acp-11-1879-2011, 2011.

C h a p t e r   5

CONCLUSIONS

This work investigates the use of computational models to study air quality in understudied rural areas and of acute pollution events, and the development of required model inputs. In chapters 2 and 3, an anthropogenic emission inventory for India was prepared and applied in the Community Multiscale Air Quality Model (CMAQ) with special focus on emissions from cooking with solid biofuels. In chapter 4, a historic wildfire was simulated with the Weather Research and Forecasting Model coupled with chemistry (WRF-Chem), and the ability of the model to reproduce the plume's effects on air quality was assessed.

In chapter 2, it was estimated that over a third of ambient $PM_{2.5}$ was attributable to household emissions. Secondary organic aerosol (SOA) was found to account for over a third of residential $PM_{2.5}$ and up to half of ambient $PM_{2.5}$. This work demonstrates that improving cooking technology may be a valuable strategy for mitigating outdoor air pollution, as well as indoor. Success of future mitigation efforts relies on further study and development of the anthropogenic emissions inventory. The construction of an inventory for use in India posed a significant challenge due to very sparse data. The inventory employed in chapter 2 included emission factors (EF) by lumped biofuel types and diurnally varying household energy consumption. However, the inventory did not include coal or liquid petroleum gas (two additional widely used fuels) in the EF profiles. As cooking was found to contribute significantly to particulate matter levels, rural area air quality exhibited a strong diurnal trend. While the transportation sector was also included in the inventory, they were not diurnally distributed, despite the distinct temporal variation in driving behavior. Integration of additional fuel-specific data and traffic trends into the inventory would improve similar simulation studies. More sensitivity analyses are needed to better understand the impacts of individual cooking fuels and inform mitigation strategies.

In chapter 3, the discrepancy between findings from lab experiments and field studies of cookstove technologies was exposed. Combustion conditions and resulting emission

characteristics are highly variable due to differences in operation and fuel availability, type, and moisture content. Lab experiments are conducted in a more controlled manner and tend to have more efficient and complete combustion. Inconsistencies across methods can significantly impact the conclusions derived from these studies. Further investigation is needed to understand the uncertainties of experimental techniques and to build a more representative profile of cookstove emissions. Data from a multitude of lab and field experiments are employed in the chemical and aerosol mechanisms in CMAQ, warranting updates to the mechanism when new data is obtained from more representative studies. Cookstove type and fuel availability vary regionally. The impact of cooking varies seasonally as fuel availability and meteorology also change seasonally. Thus, greater spatiotemporal coverage of cooking parameters is necessary to inform cookstove design and conduct comprehensive mitigation strategy studies. Greater coverage of surface air quality monitoring would also improve this work.

In chapter 4, the ability of WRF-Chem to reproduce wildfire plumes was evaluated by conducting simulations of the 2018 northern California Camp Fire. The study found that it is possible to reproduce long range transport of wildfire plumes, an important skill for smoke forecasting as well as health and economic impact assessments. However, near-source $PM_{2.5}$ was substantially overpredicted, calling for further investigation into the plume rise parameterization and local atmospheric dynamics. The recently produced TROPOMI aerosol layer height retrieval shows potential as analytical tool for plume studies, but further development of the method by which it can be compared with parameters generated by air quality models is needed. Numerous sensitivity studies in chapter 4 demonstrate the importance of vertical structure in predicting $PM_{2.5}$ and uncover variability in fire emission inventories. The analysis used both surface data and satellite products and can inform the development of data assimilation systems, an important endeavor as the air quality research field expands. Increasing occurrence and intensity of wildfires as the climate changes establishes the growing need for accurate simulations.

This work has shown that the applicability of air quality models like WRF-Chem and CMAQ to exposure modeling of both regional air pollution and acute pollution events is promising.

The simulation studies have identified quality model configurations that can serve as the base for future studies and computational cost optimization efforts. The study of India in chapter 2 is one of the first of its kind and provides a strong reference point for future study of regions historically understudied.